Title

Rational Materials Design Enabling High Energy Density Lithium-Ion Batteries

Permalink

https://escholarship.org/uc/item/7tb2g43f

Author

Shi, Wenyue

Publication Date

2020

Peer reviewed|Thesis/dissertation

UNIVERSITY OF CALIFORNIA

Los Angeles

Rational Materials Design Enabling High Energy Density Lithium-Ion Batteries

A dissertation submitted in partial satisfaction of the

requirements for the degree Doctor of Philosophy

in Chemical Engineering

by

Wenyue Shi

2020

ABSTRACT OF THE DISSERTATION

Rational Materials Design Enabling High Energy Density Lithium-Ion Batteries

by

Wenyue Shi

Doctor of Philosophy in Chemical Engineering

University of California, Los Angeles, 2020

Professor Yunfeng Lu, Co-Chair

Professor Vasilios Manousiouthakis, Co-Chair

The aggravated environmental issues and limited resources call for renewable substitutions for fossil energy. In order to enable the wide use of renewable energy resources such as wind power and solar power, energy storage devices and materials have to be developed accordingly. Among all the energy storage candidates, rechargeable batteries, especially lithium-ion batteries (LIBs) show great potential. The high energy and power density of LIBs benefitted from the light-weight of lithium metal is a great advantage over other energy storage devices such as lead-acid batteries. They are also relatively environmental-friendly as a result. LIBs have long cycling life, with little memory effect. The properties of LIBs including physical features and energy storage characteristics are adjustable and flexible with different designs and use of materials, endowing them with broad applications from portable consumer electronics to electric vehicles to grid-scale energy storage.

Anode as one major component of LIBs, has been a research focus for years. In light of the strong need for LIBs with higher energy density, silicon anode materials and lithium metal anode have been especially popular because of their ultrahigh specific capacity that significantly boosts the energy density of the according cells. Given their favorable advantages, they have major drawbacks that decisively hinder their applications in the market. Silicon materials, decided by its alloying lithiation mechanism, have almost 300% volume expansion upon full lithiation, which can cause serious fractures on the electrode and eventual failure. On the other hand, despite the high capacity and low lithiation potential of Li metal, Li dendrite growth is a severe problem that directly leads to a cell failure and even unwanted safety concerns.

In this dissertation, low-cost and durable silicon anode materials are developed. To overcome the major problems of Si anode materials, a covalently-bonded nanocomposite of silicon and poly(vinyl alcohol) (Si-PVA) by high-energy ball-milling of a mixture of micron-sized Si and PVA is designed. The obtained Si nanoparticles are wrapped by resilient PVA coatings that covalently bonds to the Si particles. In such nanostructure, the soft PVA coatings can accommodate the volume change of the Si particles during repeated lithiation and delithiation. Simultaneously, as formed covalent bonds enhance the mechanical strength of the coatings. Due to the significantly improved structural stability, the Si–PVA composite delivers a lifespan of 100 cycles with a high capacity of 1526 mAh g–1. In addition, a high initial Coulombic efficiency over 88% and an average value of 99.2% in subsequent cycles can be achieved. This reactive ball milling strategy provide a low-cost and scalable route to fabricate high performance anode materials.

To take a further step, an electrolyte membrane is designed and developed to enable the use of Li metal anode. . Inspired by ion channels in biology systems, we constructed lithium-ion

channels by chemically modifying the nanoporous channels of metal-organic frameworks (MOFs) with negatively charged sulfonate groups. Analogous to the biological ion channels, such negatively charged moieties repel anions while allowing effective transport of cations through the pore channels. Implementing such MOFs as an electrolyte membrane dramatically improves the lithium-ion transference number, enhances the rate capability and durability of the batteries. With the MOF membrane, Li dendrite growth is much suppressed, leading to an improved Coulombic efficiency and a prolonged cycle life.

The dissertation of Wenyue Shi is approved.

Dante Simonetti

Qibing Pei

Vasilios Manousiouthakis, Committee Co-Chair

Yunfeng Lu, Committee Co-Chair

University of California, Los Angeles

2020

Table of Contents

List of Figures

List of Tables

Acknowledgment

I would like to express my gratitude to my advisor, Dr. Lu, for his guidance and instructions during the years. His generosity and kindness made lots of things easier for me.

I would like to thank all my colleagues in Lu group. Specifically Dr. Li Shen, Dr. Gen Chen, Dr. Guoqiang Tan, Dr. Xianyang Li and Pengcheng Xu for contributing to this dissertation.

I would like to thank Jesse Baucom, for always being there for me.

I would like to thank my parents, for their unconditional love and support.

VITA

2012 – 2016   B.S. Chemistry

                                                     Peking University

2016 – 2020   Teaching Assistant, Graduate Researcher

                             Department of Chemical and Biomolecular Engineering

                                  University of California, Los Angeles, USA

Publications

1. **<u>Wenyue Shi,</u>** Jianqiang Shen, Li Shen, Wei Hu, Pengcheng Xu, Jesse A. Baucom, Shengxiang Ma, Shuxing Yang, Xiao-Ming Chen, and Yunfeng Lu, Electrolyte Membranes with Biomimetic Lithium-Ion Channels. *Nano Letters* Article ASAP, DOI: 10.1021/acs.nanolett.0c01910

2. **<u>Wenyue Shi</u>**, Hao Bin Wu, Jesse Baucom, Xianyang Li, Shengxiang Ma, Gen Chen and Yunfeng Lu, Covalently-bonded Si-polymer Nanocomposites Enabled by Mechanochemical Synthesis as Durable Anode Materials. *ACS Applied Materials & Interfaces,* in revision

3. Kaiqiang Qin, Jesse Baucom, Deliang Liu, **<u>Wenyue Shi</u>**, Naiqin Zhao, Yunfeng Lu, A Powder Metallurgic Approach toward High-Performance Lithium Metal Anodes. *Small* 2020, 16, 2000794. DOI: 10.1002/smll.202000794

4. Dejia Kong, Li Shen, Runwei Mo, Jiaxu Liu, Ran Tao, **<u>Wenyue Shi</u>**, Shengxiang Ma, Chen Zhanga and Yunfeng Lu, CVD-assisted fabrication of hierarchical microparticulate Li2TiSiO5-carbon nanospheres for ultrafast lithium storage. *Nanoscale* 2020 DOI: 10.1039/d0nr02821

Chapter 1: Introduction

1.1 Background

In spite of the emergence of modern society and the aggressive development of human technologies, today in the year of 2020, after over 200 years from the first Industrial Revolution and humans started to use coals extensively, and also over 200 years from the first real battery was invented, our daily commute is still mostly dependent on simple combustion reactions that consumes the non-renewable fossil energy decayed for hundreds and millions of years – fuels.

Sustainability is hardly the biggest problem for fuels. As **Figure 1.1**a shows, CO2 concentrations in the atmosphere are at their highest levels in over 80,000 years. More specifically, the concentration of CO_2 doubled within the last 200 years, exceeding a normal range of fluctuations, and aligning with the development of modern technologies and global economics. Among the major causes for the astonishing and drastic increment of atmospheric CO_2 concentration, transportation contributes approximately 20% (**Figure 1.1b**), which mainly comes from the combustion of oil and gasoline.
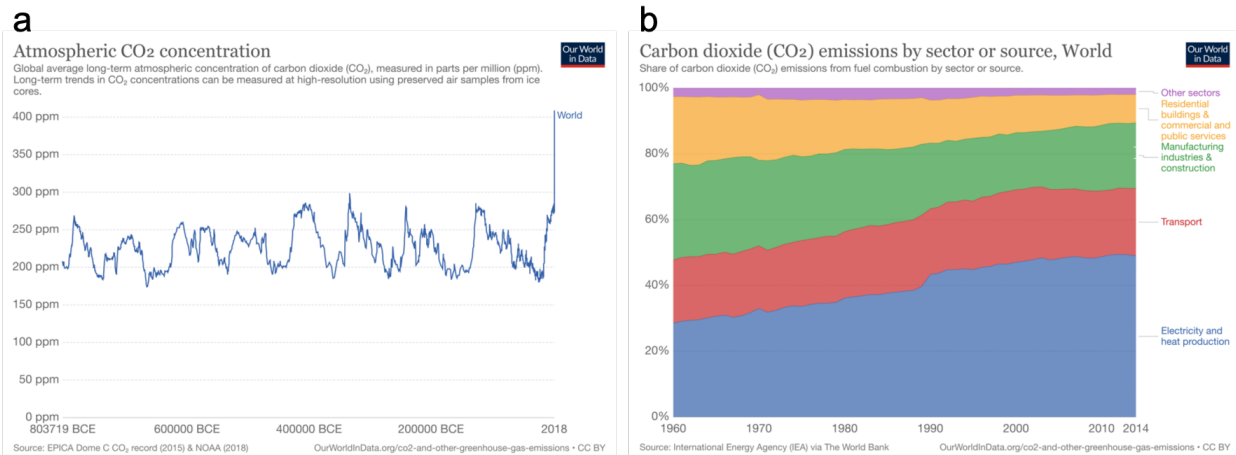
Figure 1.1 (a) Global atmospheric CO_2 concentration over the years up to 2018. (b) Global CO_2 emissions by different sectors or sources.[1]

Human emissions since 1850 accounts for almost all of the global warming. It would be redundant to stress the devastating consequence global warming can induce to human societies. Especially in the past several years, we have experienced numerous wildfires, unpleasant climate changes etc., closely or remotely related to global warming. People gradually come to the realization that we cannot avoid those problems. We cannot wait and sit back to throw those problems on the next generation, because the global warming seems expediting its pace to affect our daily life and nobody can give an assertive answer to how long our stable life can last for.

Actions are being taken. Scientists and researchers are diligently working on alternative energy sources. Wind power, solar cells, hydro power etc. are becoming more and more common in use. There is a growing trend that an increasing amount of governments and private companies are investing and working on the development and reinforcement of renewable and clean energy sources[2] (**Figure 1.2a**). However, the sole development of energy generation sources is not good enough to alleviate the energy problem. Figure 1.2a shows that solar energy almost always takes up over one third of the total investments. Solar energy is one of the most favored energy sources since it is believed to be completely clean and sustainable, less selective to regions and environments and more approachable for installments and deployment compared to wind energy and hydro energy. One limiting factor for solar cell applications is, indeed, its high or even unaffordable cost, which largely comes from its energy storage systems. Solar cells convert and store solar energy into batteries (lithium-ion batteries), but according to studies and statistics, the cost of lithium-ion batteries per kWh is nearly as much as the solar modules themselves, and

there might even be a shortage for the lithium-ion batteries in terms of the total amount of energy they can store (**Figure 1.2b**).
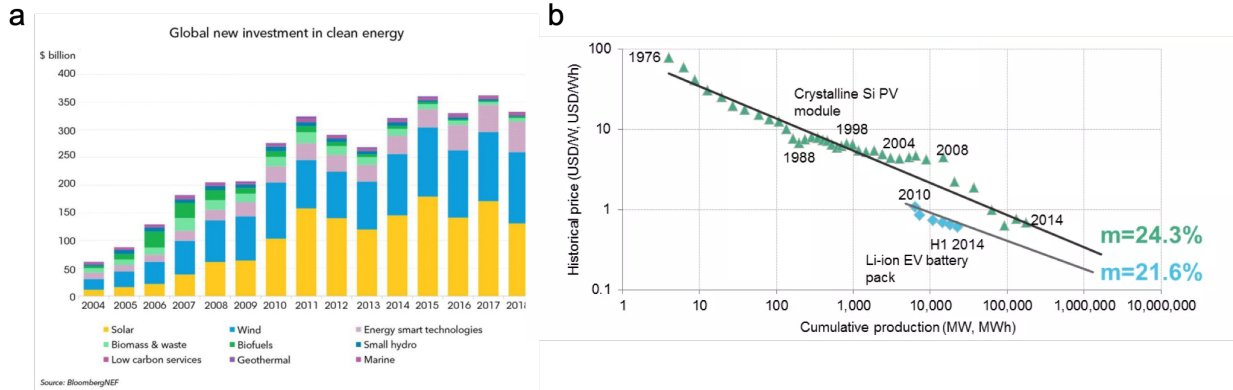
Figure 1.2 (a) Trends and distributions of global new investment in clean energy.[2] (b) The cost of lithium-ion batteries and crystalline silicon photovoltaic modules.[3]

People have reached a consensus that while we are seeking for an alternative clean energy for the sake of the environment protection, it is also important to extend our knowledge and improve the technologies for energy storage systems.

1.2 Energy Storage Technologies

As mentioned above in 1.1, it is critical to develop energy storage technologies while developing energy generation technologies. Energy storage technologies collect and store the energy generated from renewable energy sources that produce energy intermittently to achieve a steady energy supply. Based on the form of energy that is released from the energy storage systems, there are thermal energy storage (TES) and electrical energy storage (EES) technologies.

TES systems can involve no phase change (sensible heat storage, such as molten salts and concrete), undergo a phase change (latent heat storage, such as fatty acids and esters) or be associated with a reversible chemical reaction (thermalchemical heat storage, such as ammonia systems). They are often used to utilize the heat loss from energy supply chains and to increase the flexibility of combined heat and power plants.[4]

EES on the other hand, is regarded as one of the most readily available form of energy. It is widely applied in consumer products, residential power supply and public services. According to **Figure 1.3a**, the annual net generation of electricity is steadily growing over the years, with a majority from fossil forms, renewable energy sources constituting a bigger portion every year. Therefore, there is a corresponding growing demand for EES systems. Pumped hydro storage (PHS) is a form of electromechanical energy storage system for large scale energy storage. PHS uses electricity to pump water to an upper reservoir at electricity valley load, and let the water flow to the lower reservoir to activate the turbine and generate electricity.[5] It is designed for a rational deployment of electric energy. Other major electromechanical energy storage systems include flywheel energy storage, gravity energy storage and compressed air energy storage. Hydrogen energy storage (HES) as a form of chemical energy storage is clean, storable and transportable with high energy density. Hydrogen is usually used in a fuel cell and produce electricity through the chemical reaction of H_2 and O_2. The major drawback is the high cost of the catalysts and the low energy conversion efficiency during the H_2 production step. Electrochemical energy storage including supercapacitors and batteries. They are usually highly approachable, adjustable and transportable. They are widespread from portable consumer electronics to electric vehicles.
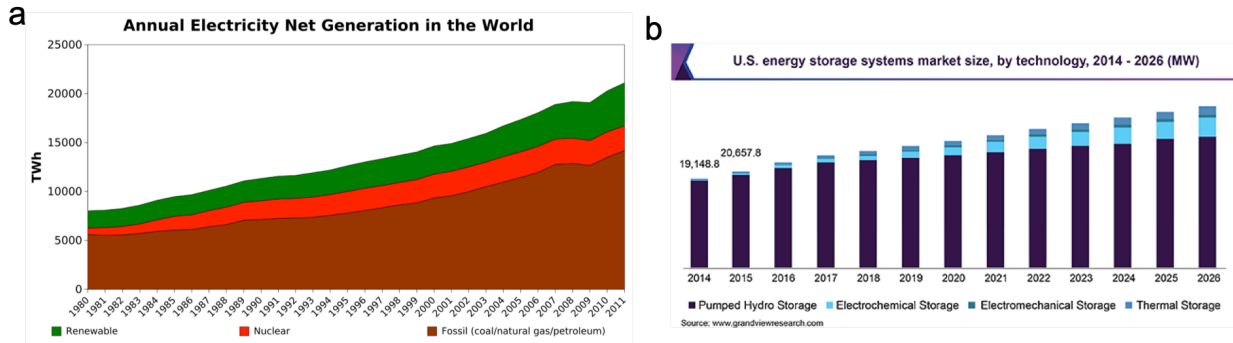
Figure 1.3 (a) Annual electricity net generation in the world.[6] (b) Energy storage systems market size in the U.S.[7]

Figure 1.3b shows the market size for different mainstream energy storage systems in the U.S. PHS as a grid-scale energy storage system is leading the market share. Electrochemical storage is following and going to share bigger market size in the future according to the prediction.

Table 1.1 compares the efficiency of different energy storage technologies. Conversion efficiency refers to the process of converting the energy stored into released form of energy. Delivery efficiency refers to overall delivery of energy from the pristine fuel through the base load power generator and energy storage plants. Effective efficiency describes the ability of the energy storage plants to effectively store the electrical energy. The conversion efficiencies vary from 70% to 91%, with electromechanical flywheel energy storage being the lowest, and superconducting magnetic energy storage (SMES) being the highest. All types share a similar delivery efficiency within the range of 24% to 31%. The distribution of effective efficiencies is close to the conversion efficiencies. Even though the energy efficiencies are still in development, flywheel energy storage has a flexible size and accordingly shorter construction time, same as battery energy storage.

Table 1.1 Performance and characteristics comparison for energy storage plants.[8]

Energy Storage Technology	Efficiency[1],[2],[3]			Size (MW)	Construction Time (years)
	Conversion	Delivery	Effective		
Compressed Air Energy Storage (CAES)	N/A[4]	28	82	50-220	2.5-4.0
Pumped Hydro (PH)	75	26	75	1000-2000	8-12
Battery Energy Storage (BES)	75	26	75	1-1000	1-2
Flywheel Energy Storage (FES)	70	24	70	0.1-1.0	1-2
Superconducting Magnetic Energy Storage (SMES)	91	31	91	0.1-2000	1-8

Table 1.2 shows the different costs to build energy storage plants. Compared to conventional pumped hydro energy storage, which costs totally $1200 – 1700/kW, more recent technologies including battery, flywheel and SMES are favored with a much lower price. Battery technologies are especially standing out for only $320/kW overall cost (advanced). Energy storage technologies are not always readily to be built and operated, and governments have to consider multiple variables before policy enforcement. Therefore, battery (electrochemical) energy storage technologies with low-cost, high operability and adjustability, simpler and faster constructions become one of the most popular choices.

Table 1.2 Cost comparison for energy storage technologies.[8]

Energy Storage Technology	$/kW +	$/kWh* x	H =	Total Capital, $/KW
Compressed Air				
-Large (110 MW)	390	1	10	400
-Small (50 MW)	530	2	10	550
Pumped Hydro				
-Conventional (1000MW)	1100	10	10	1200
-Underground (2000MW)	1200	50	10	1700
Battery (target) (10MW)				
-Lead Acid	120	170	2	460
-Advanced	120	100	2	320
Flywheel(target) (100MW)	150	300	2	750
Superconducting Magnetic Storage (target) (1000MW)	120	250	2	720

1.3 Electrochemical Energy Storage Systems

Electrochemical energy storage is an established and valuable approach to improve the reliability and overall use of the entire power system (generation, transmission and distribution.)[9] EES can be employed from grid-scale services (power plants etc.), to portable smart electronic devices (mobile phones etc.). Electrochemical energy storage systems refer to various batteries that generate and release through the conversion of chemical reactions. According to **Figure 1.4a**, the group of batteries including lithium-ion, lead-acid, sodium-sulfur etc. is flexible to cater for the demands in terms of rate power and discharge time. Based on the design and architecture of the system, the rated power for a battery can vary from 0.01 to 100 MW, and the discharge time can vary from 0.001 to over 10 hours.[9] Compared to electromechanical energy storage systems including PHS and compressed air, batteries have lower power, but more affordable and accessible. Double-layer capacitors store electric energy in the form of electrical charges instead of chemical reactions. They deliver a decent power and an extremely short, or even instantaneous charge. Applications that require ultrafast charging/discharging or unstable and pulsing charging/discharging such as EVs during its acceleration broadly use capacitors. However, as an EES system, they have low output voltage and suffer severe self-discharging. As a result,

capacitors are often in a combined usage with batteries and other energy storage systems or for grid power applications.
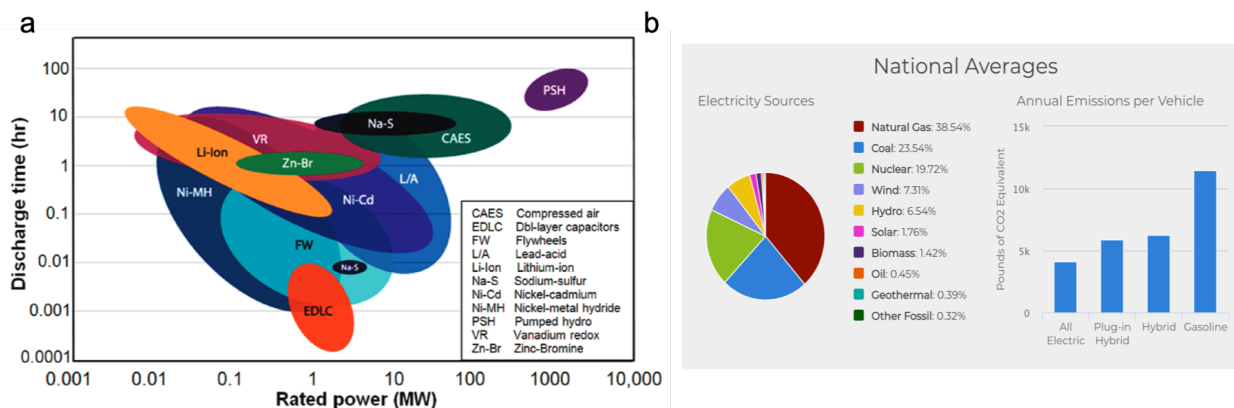
Figure 1.4 (a) Power ratings and discharge time for various EES systems.[9] (b) Major electricity sources and annual CO_2 emission per vehicle in the U.S.[10,11]

The small sizes and portability of batteries are indeed a critical advantage for its extensive applications in our daily life. In 2020, more and more electric vehicles (EVs) are drawing substantial attention from people. **Figure 1.4b** shows one good reason. Each electric vehicle can reduce the CO_2 emission by two thirds in one year, in comparison with an all gasoline vehicles. Even hybrid electric vehicles (HEVs) with less aggressive changes can reduce half of the CO_2 emission.[10–12] Relieving the global warming on the side, the rocketing development for smart devices and the demanding expectations from consumers also keep the researchers for electrochemical energy storage systems on the cutting edge. Most mobile phones run out of battery within ten hours under heavy usage[13], which brings inconvenience to people in some circumstances such as long trips and it could be a hassle to feel obligated to charge them every day. For Apple products, the battery weight for their latest products can take around 30%

of the total weight[14]. Beside safety, people are also calling for high energy density from next-generation batteries.

Based on the chemical reactions occurring during the energy conversion process, there are four major battery technologies, including redox flow batteries (RFB), Na-S/Na-metal halide batteries, lead-acid batteries and lithium-ion batteries.
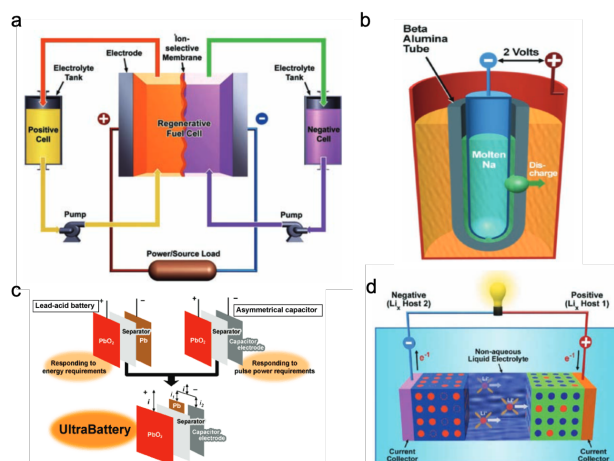
Figure 1.5 Four major types of batteries. (a) Redox flow battery (RFB). (b) Na-S or Na-metal halide battery. (c) Lead-acid battery. (d) Lithium-ion battery.

RFB as its name suggests, utilizes redox reaction in aqueous solutions (**Figure 1.5a**). Common redox couples include $Fe^{2+}/Fe^{3+} \| Cr^{2+}/Cr^{3+}$, $Ce^{4+}/Ce^{3+} \| V^{2+}/V^{3+}$, $Fe^{3+}/Fe^{2+} \| Br_2/Br^-$ etc. RFBs potentially have long cycle life, and they are mainly applied for grid-scale energy storage for their MW energy storage. The limitations include high capital cost, possibly low long-term stability from the electrolyte and self-discharging issues.[15]

In Na-S and Na-MH batteries, reversible charge and discharge occur via Na-ion conducting (**Figure 1.5b**).[16] The battery often uses liquid sodium for the high ionic conductivity, thus is usually operated at 300 – 350 ºC. High temperature Na batteries have high energy efficiency, but the high temperature conditions also bring challenges for packaging and sealing.[17]

Given other irreplaceable advantages of Na batteries such as plentiful natural resources for sodium, they are a research target and a trending topic for scientists and researchers.

Lead-acid battery is a traditional type of battery that can be dated back to 1860 and matured over the years (**Figure 1.5c**). It is the least expensive type of batteries in terms of capital cost ($/kWh). However, because of their short cycle life and low energy density, they are not as popular as their peers.[18] Moreover, the use of lead metal can lead to severe environmental pollution, prompting some governments to formulate unfavorable policies and eliminate lead-acid batteries manufacturing and applications. Researchers are working on substituting the lead anode partially or completely with carbon in order to further improve the performance.

Lithium-ion batteries (LIBs) store energy in the form of lithium ions intercalation or insertion. They have very high energy efficiency (~100%), high energy density and high power. With the mix and match of different cathode and anode materials, LIBs with various capacity, cycle life and rate performance can be obtained. They are the go-to battery for various purposes including portable electronics, electric vehicles and grid-scale power plants. Given LIBs' appealing natural properties, a lot of research is being done to overcome their limitations and improve their advantages to a higher level, which include the safety concerns brought by the flammable organic solvent and possibly lithium metal, high cost ($/kWh), narrow operating temperature window and recycle and reuse of metal elements from the electrode materials.[19]

1.4 Development of Lithium-Ion Batteries (LIBs) Materials

A battery contains three or four necessary parts: cathode, anode, electrolyte and separator. In lithium-ion batteries (LIBs), the two electrodes are lithium-ion conductive and electronic conductive, but the electrolyte and the separator only conducts or let through lithium

ions but not electrons. Cathodes have a high chemical potential over Li/Li^+, while anodes have a lower potential over Li/Li^+. During the battery charging process, the electric energy from the external power serving as a stream of electrons flowing through the external circuit to the anode, forces the lithium ions inside the LIB to flow to the same electrode in order to maintain the charge balance. During the discharging process, the lithium ions travel from the anode to the cathode through the separator carried by the electrolyte, causing the electrons flowing in the external circuit to support the external devices.

Around 1960s, scientists studied the reversible Li ions insertion behaviors into transition-metal sulfides with aqueous electrolyte solutions. That concluded the first tryout for LIBs. With water present, the voltage of the cell is limited. Not until late 1970s, Stanley Whittingham had created a lithium-ion rechargeable battery with TiS_2 cathode, and that inspired John B. Goodenough to investigate the reversible Li-ions insertion characteristic of a layered compound $LiCO_2$, then led to Akira Yoshino make the first real rechargeable lithium-ion battery (**Figure 1.6**), pairing with graphitic-carbon.[20] The following reactions demonstrate the charging process going on in the cell:

$$LiCoO_2 \longrightarrow x\ Li+ + x\ e^- + Li_{1-x}CoO_2 \qquad (1)$$

$$6x\ C + x\ Li^+ + x\ e^- \longrightarrow x\ LiC_6 \qquad (2)$$
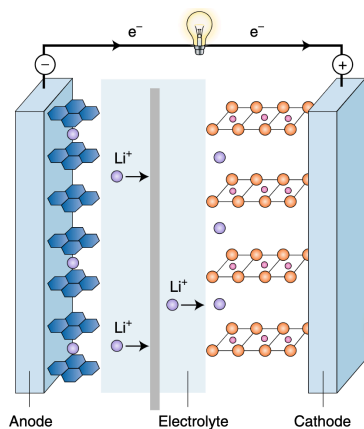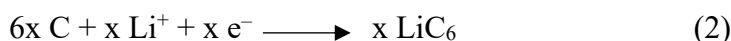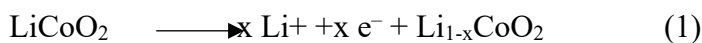
Figure 1.6 Components of lithium-ion batteries.[20]

For practical and commercial applications, those are the criteria that are mostly considered and discussed for a battery: (1) Energy density (kWh/kg, kWh/L), which decides the how much energy the battery can carry; (2) Power density (W/kg, W/L), which determines the output power it can provide to the external devices; (3) Cycling stability or cycle life, which decides how long the battery can be used and how often it needs to be replaced; (4) Rate performance, which determines how fast the battery or the device can be charged; (5) Other factors including operating temperature window, self-discharging, recyclability and etc.

Modern LIBs continue to use this configuration, even the electrode materials of the first LIB, but after years of breakout for materials research on LIBs, people have developed numerous advanced materials for electrodes and electrolytes that have different properties for applications with different requirements.

1.4.1 Cathode Materials Development

Cathode materials are the decisive part of some critical properties of LIBs. **Figure 1.7** illustrates the mainstream lithium-transition metal based cathode materials structures. They are olivine $LiTMPO_4$, spinel $LiTM_2O_4$, layered $LiTMO_2$ and Li_2TMSiO_4. Because they have different structures and properties, the according batteries deliver diverse performance and features.[21]

Classic $LiFePO_4$ cathode is a typical olivine $LiTMPO_4$. The structure of $LiFePO_4$ consists of corner-shared FeO_6 octahedra and edge-shared LiO_6 octahedra linked together by PO_4 tetrahedra. The oxygen atoms are strongly bonded by both Fe and P atoms, thus $LiFePO_4$ shows

a good high temperature stability up to 400 ºC. However, the strong covalent oxygen bonds also lead to poor electronic conductivity (~10^{-9} cm/S), which compromises its performance at low temperatures. $LiFePO_4$ does not experience a severe phase change like some other cathode materials, which brings a long cell cycle life. Combined with its good safety, $LiFePO_4$ is widely used in traditional EVs. Even though $LiFePO_4$ has a decent specific capacity (170 mAh/g), due to its low tap density, the according cells are usually low in energy density (kWh/kg, kWh/L).[22] In recent years, new companies for EVs tend to choose other cathode materials that can offer a higher energy density instead of $LiFePO_4$.
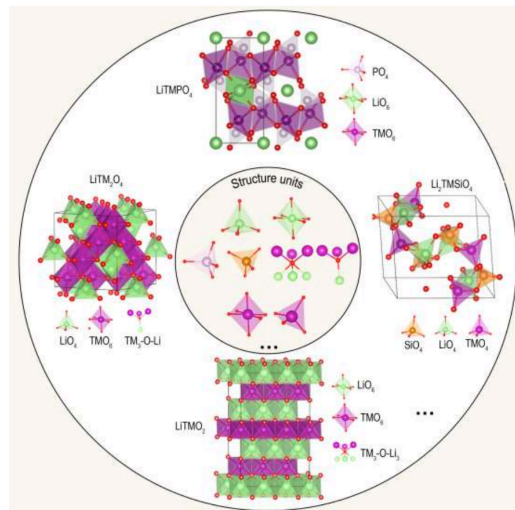
Figure 1.7 The structure units of some representative cathode materials (olivine $LiTMPO_4$, spinel $LiTM_2O_4$, layered $LiTMO_2$ and Li_2TMSiO_4), TM denotes transitional metals.[23]

Spinel structured $LiTM_2O_4$ includes $LiMn_2O_4$ and $LiNi_{0.5}Mn_{1.5}O_4$. $LiMn_2O_4$ possesses a face-centered cubic spinel structure and provides a 3-dimensional channel for lithium ions to travel. The Mn with 3+ covalence state has strong Jahn-Teller effect.[24] As a result, the Mn metals in $LiMn_2O_4$ tend to immigrate and dissolve into the electrolyte, causing the poor cycling

stability. To improve the performance, some metals are used to partially substitute Mn atoms. Among them, Ni is the most successful and attractive candidate because of its high working voltage (~4.7 V) and considerably high specific capacity (~148 mAh/g). However, the introduction of Ni does not solve the problem of the poor cycling stability and this material still suffers quick capacity decay. Despite the intrinsic problem of Mn elements, those cathodes with spinel structures are still popular for research and commercial purposes, considering the incomparably high voltage, low cost and the improvement of thermostability by Mn.[25,26]

Layered $LiTMO_2$ cathode is the most intriguing topic for both academics and industry, for its high content in lithium and higher specific capacity. Materials with most applications include $LiCO_2$ (LCO), $LiNO_2$ (LNO), $LiNi_xCo_yMn_{1-x-y}O_2$ (NCM) family and $LiNi_xCo_yAl_{1-x-y}O_2$ (NCA) family.[27] LCO is the cathode material used in the first commercial LIB but still widely applied in electronics. LCO delivers a decent working voltage (~4.25V), good cycling stability and high tap density unmatched with other cathode materials. On the other hand, LCO, similar to LNO, because of their layered structures, layers can go through a breakdown and collapse once all the lithium ions are extracted. Therefore, to maintain the structural stability, only around 50% lithium ions are utilized during the delithiation process in practical applications.[28] Another realistic disadvantage of LCO comes from the cobalt they use. Companies are trying to prevent using LCO due to the scarcity of the Co minerals and also the serious environmental pollution caused by this heavy metal. Nickel is a less toxic and richer metal resource and its oxides show high activity for lithium storage, but as mentioned above, the structural instability of LNO essentially hinders its application. As a result, other metals are introduced to partially substitute Ni to improve the performance, such as Mn, Co and Al. For example, the substitution of small Co ions results in lattice contraction and suppress the immigration of Ni to Li^+ sites.[29] Some

common compositions for NCM include 111 ($LiNi_{0.33}Co_{0.33}Mn_{0.33}O_2$), 523, 622 and 811, which cater for different needs and currently are developed to different stages. Higher Co and Mn ratios both bring higher structural stability. Co also brings better rate performance, but Mn on the contrary impairs the kinetics. The problems of those elements themselves will be taken into account as well, such as high cost for Co and dissolution of Mn.[30] Al is another popular metal element to be doped into layered nickel oxides structures. The EV leader in the market Tesla chooses NCA-80 ($LiNi_{0.8}Co_{0.15}Al_{0.05}O_2$) as the cathode material for their batteries. Al improves the structural stability, as well as the kinetic properties, but NCA usually involves complex synthesis procedures. Large amount of efforts from both research institutes and industries are committed to develop high-nickel cathode materials. Approaches that are confirmed effective include but not limited to surface coating[31,32], grain boundary strengthening[33,34], primary particle nanosizing[35], primary particles reshaping[36] and realignment and single-crystal particles[37,38].

Even though transition metal silicates including Li_2FeSiO_4 and Li_2MnSiO_4 are cheap and safe, they deliver low specific capacity that are unsatisfying and not promising for the improving energy demands.[39] As a result, the amount of research works on those materials are limited.

1.4.2 Anode Materials Development

Another direction to achieve LIBs with high energy density is through the development of anode materials. Unlike cathode materials that have been updated for several generations, graphitic carbon materials have been dominating the market for anode materials since the debut of LIBs. Although anode materials only take up approximately 14.3% of the cell cost and 10.6% of the cell mass[30], they are an undeniably critical component of the battery, not only because of the irreplaceable role they are playing, but also because of the impact they can bring to the

cell/battery energy and power density.[40] The U.S. Department of Energy goals for EV batteries

are 350 Wh/kg, 750 Wh/L and US$75/kWh at the cell level, in order to enable the full driving

performance and price of an internal combustion engine vehicles via EVs. For the near future,

the U.S. Advanced Battery Consortium expect batteries to have energy density over 275 Wh/kg

and 550 Wh/L at the cell level by 2023 [30,41] To achieve such values at the cell level, it is

estimated that around 500 Wh/kg is needed at the electrode pack level.[27,42] As **Figure 1.8a**

shows, cells that use the most common commercial anode material graphite (C) lie on the bottom

left corner of the diagram, which indicates low energy densities and specific energies, and the

corresponding specific energy (< 400 Wh/kg) is unsatisfying to reach goal.
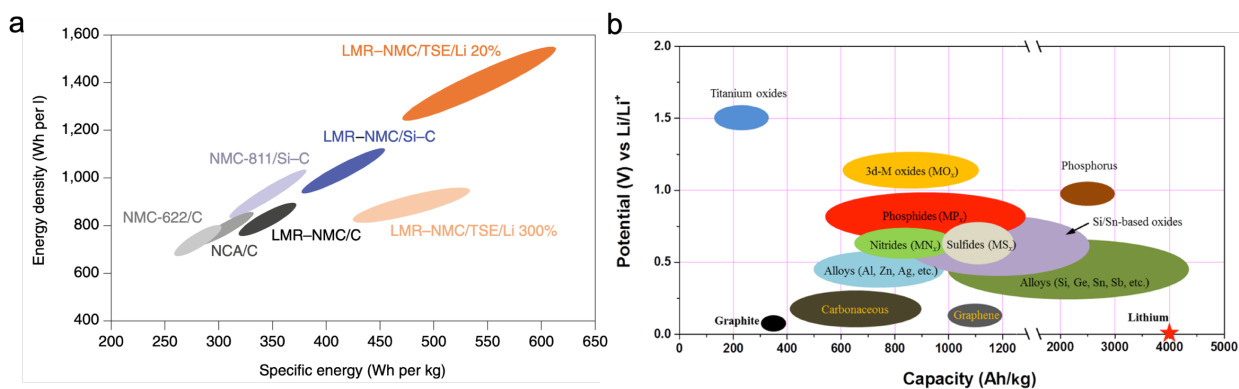
Figure 1.8 (a) Energy density versus specific energy diagram of different cell chemistries at

electrode stack level.[43] (b) Potentials (vs. Li/Li$^+$) and corresponding capacity density of cells

with different cell chemistries.[44]

       Figure 1.8b explicitly demonstrates the research map for anode materials. The ideal

anode material should have high specific capacity (mAh/g) and low potential (vs. Li/Li$^+$) so that

it will enable high energy density while also offering output voltage of the corresponding cell.

Given those principles, anode materials on the bottom right corners, including Si, Ge, Sn, Sb

alloys and lithium metals, are the most promising and attractive materials for developing next-generation lithium batteries.

Based on the reaction mechanism with lithium ions, anode materials can be divided into three major categories: intercalation, alloying and conversion. Intercalation types, as indicated by its name, let lithium ions intercalate into their d-spacing lattices without causing pronouncing volume change of the hosts, including some best-known anode materials such as graphite and lithium titanate.[45] They usually have long cycle lives and high safety level due to the minimal phase and volume changes of the materials, but at the same time offer quite limited capacity. Alloying types including silicon and its family (germanium, tin, etc.), namely forming alloy compound phases with lithium ions, are the most beloved troublemakers, as they provide extremely high specific capacity and yet extremely poor cycling stability before modifications due to the dramatic volume expansion during the lithiation process. Conversion types undergo a reversible reduction/oxidation with lithium ions. They are usually metal compounds (Fe_3O_4, CuO, NiO, MoS_2, etc.) that can form composite with lithium.[44] They deliver relatively higher capacity than intercalation types, but have intrinsic low Coulombic efficiency and short cycle lives due to the unideal irreversibility from the lithiation/delithiation. Lithium metal anode, technically is also a conversion anode by its definition, but special as it is, people tend to study it as an exciting new type. Lithium metal anode experiences the stripping and plating between lithium ions and lithium metal. With no doubt it provides the highest specific capacity and the lowest potential (vs. Li/Li^+), while also facing problems such as low Coulombic efficiency, safety concerns brought by the existence of lithium metal and the risk of short-circuiting, and limited cycling stability.
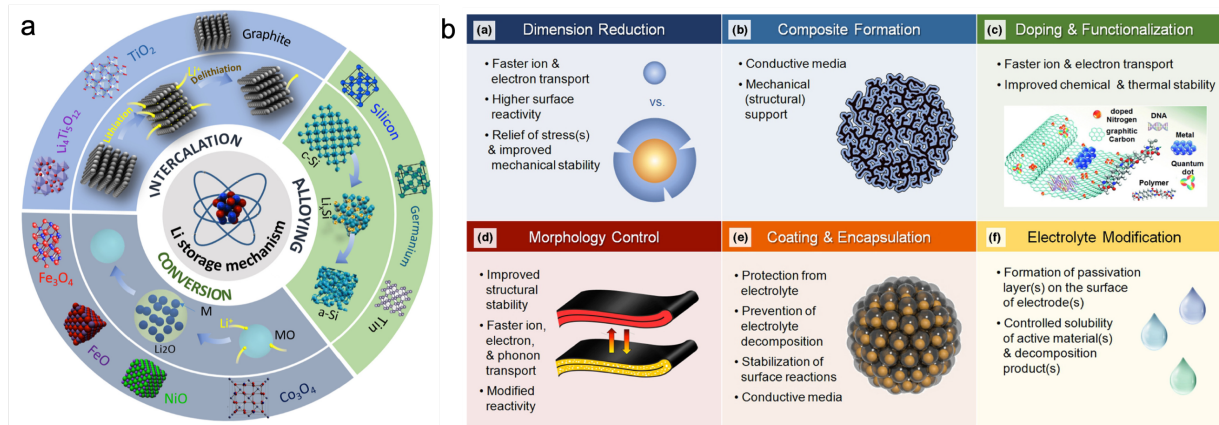
Figure 1.9 (a) Schematic illustration of different reaction mechanism of anode materials for LIBs.[45] (b) General strategies for performance enhancement and their rationales.[46]

Over the years, people have conducted extensive research works on improving the performance of anode materials. The most popular and famous methods can be classified into six categories as shown in **Figure 1.9b**. Dimension reduction refers to particle size breakdown, i.e. from macroscale to nanoscale. Composite formation is to mix the active anode materials with some conductive, structure-supportive materials or surface modifying materials to form composites. Doping and functionalization is to introduce dopant elements into the material structure to improve specific properties. Morphology control changes the performance of the materials by manipulating the morphology, e.g. to 2-dimensional, spherical or tubes. Coating and encapsulation are extremely commonly used to protect material particles from pulverization through a surface coating layer. Electrolyte modification such as additives can improve the solid-electrolyte interfaces (SEIs) formed on anode particles.

For researchers, it is meaningful to improve the performance and modify the properties of the anode materials by all means. However, when it comes to industrialization, the cost certainly plays a significant role for the application. Even though batteries with higher energy and power

18

are expected in the future, the cost for batteries ($/kWh) is anticipated to be lower and lower.[47] Anode materials, usually as the cheap part of the cells because of the mature process of graphite, only takes up less than 20% of a total cell cost,[30,43] have to be developed in a cost-efficient way in order to be valuable for commercial applications. Taking all the considerations into account, carbon-based anode, LTO anode, silicon-based anode and lithium metal anode are the most attractive and promising materials for commercial LIBs addressing different needs.

1.4.2.1 Carbon-Based Anode Materials

As mentioned above, carbon-based anode materials, especially graphite, have been the mostly applied anode materials for lithium ion batteries over the past until now.

Graphite has a theoretical specific capacity of 372 mAh/g[48], which is not high but understandable considering it has the intercalation mechanism. It has a low potential (~0.1 V) vs. Li/Li^+ that on one hand enables the high output voltage of the full cell, but on the other hand since the potential is getting close to the voltage where lithium metal starts to be reduced and form on the surface, the low potential could lead to generation of lithium residues and eventually causes short-circuits or thermal runaway.[49] The reason why graphite is applied universally mainly comes from the combination of its decent specific capacity and superior cycling stability. Its cycling stability also comes from the intercalation mechanism, which allows lithium ions accommodate themselves inside the gaps between d-spacing lattices without causing significant volume changes (~10.5% on a full lithiation)[50]. The specific capacity of 372 mAh/g is not satisfying for current battery development technologies. Besides, the rate performance of graphite is usually considered as a weakness, as its capacity can go below 300 mAh/g at only 0.5 C and below 200 mAh/g at 1 C, which is far from meeting the requirement for a fast-charging

battery. This shortcoming mainly comes from the slow Li$^+$ diffusion across the bulk graphite particles.[51]

Within the class of graphite, there are two types with slightly different properties. Natural graphite is highly anisotropic in terms of the particle morphology.[52] They are usually used as energy type graphite (close to theoretical specific capacity), but have specifically low capacity retention at high rate. Spherical graphite is modified to spherical shapes via surface modification based from natural graphite. They are designed to improve the rate capability of the natural graphite. Artificial graphite is carbonized and processed with high temperature. Their capacity is lower than natural graphite (310 – 360 mAh/g), but they usually deliver a higher Coulombic efficiency especially the initial Coulombic efficiency (ICE) and a better fast-charging property. Due to the increasing demand for the EVs market that requires fast-charging batteries, artificial graphite has become the mainstream anode materials with the largest annual manufacturing production worldwide.[53]

Beside the traditional natural and artificial graphite anode materials, there are some other well-known carbon materials applied in some specific areas because of their special features such as soft carbon, hard carbon with low graphitization degrees. Typically raw materials determine whether the carbon is hard or soft. Typical raw materials for soft carbon are petroleum pitch and coal tar pitch. Hard carbon can be obtained through heat treating thermosetting resins and vegetable fibers.[54]

Soft carbon includes mesocarbon microbeads (MCMB) and coke (needle coke). Soft carbon can easily graphitize when the temperature goes beyond 2000 °C. Those carbon materials have a lower specific capacity than normal graphite, usually around 300 mAh/g when heat-treated at 1100 – 1200 °C.[54] Because of their amorphous structure, soft carbon has a smaller

average particle size. Therefore, more side reactions are expected to happen during the charging and discharging process for this material. In general, soft carbon has a better rate performance than graphite. Among soft carbon materials, MCMB usually delivers a lower specific capacity, because the granularity distribution of MCMB is narrower than coke and does not contain fine powers. Therefore, the electronic conductivity of MCMB is also rather lower than coke.[55] Due to the compromised nature of soft carbon, instead of directly being used as anode materials, soft carbon is more commonly used as a primary material for graphite production.

On the other hand, hard carbon is never graphitized, even above 3000 °C under ambient pressure. At room temperature, hard carbon is difficult to lithiate and a high potential hysteresis is observed, causing the overall output voltage to be low for battery. The ICE of hard carbon cell can also be much lower than a graphite cell. However, at elevated temperatures, hard carbon can immediately deliver a higher reversible capacity than normal graphite materials, a high Coulombic efficiency and a lower potential hysteresis.[56] Considering this feature, hard carbon can be used in high-temperature applications with a suitable electrolyte. Because of the raw materials, the cost for this material is correspondingly higher than soft carbon and even graphite, which is also a factor that needs to be considered.

When used as anode materials, soft carbon and hard carbon with their larger interlayer distance, are applicable for sodium-ion batteries compared to graphite materials whose inter-planar d-spacing is only 0.34 nm and are too small to accommodate sodium ions.[57–59] Their shortcomings for lithium-ion batteries are intrinsic and concomitant with their natures, thus hard to overcome. Therefore, an increasing amount of research focus on their performance in sodium-ion batteries instead of lithium-ion batteries.

As for traditional graphite materials, they are already a highly mature commercial materials. Very few researchers focus their studies on graphite alone as the anode material. Of the minorities, most of the works challenge to improve graphite's rate performance such as using magnetic field to align the graphite particles[51] and coating spherical graphite particles with conductive layers[60,61]. Some researchers have done subtle engineering on graphite particles including using additives[62] and more effective binders[63,64] to improve the volumetric energy density and cycling stability. With no doubt, the mainstream usage for graphite beside already as the commercial anode material, is to composite it with other anode materials with higher energy density such as silicon, tin, MoS_2 and etc.[65–67] Looking through the new start-up companies strategies on anode materials , it is clear that Si/C composites are a resistible and fast-developing trend for the next-generation LIBs anode materials.

1.4.2.2 LTO-Based Anode Materials

$Li_4Ti_5O_{12}$, also known as LTO anode, is famous for its impressive fast-charging capability. LTO also uses a intercalation mechanism for lithium ions similar to graphite. However, compared to graphite, LTO is inferior in both specific capacity and the voltage. LTO usually only delivers a reversible capacity of 150 – 160 mAh/g, and a high potential vs. Li/Li^+ (~1.55 V), which leads to a low voltage of the cell.[68] In spite of the obvious disadvantages, LTO is unique in its excellent cycling stability and superior rate performance. LTO is indeed a "zero-strain" material in terms of Li^+ intercalation and deintercalation, meaning there is only a slight shrinkage of the lattice parameter, from 8.3595 to 8.3538 Å, resulting a minimal change in cell volume (about 0.2%).[69] This features helps improve LTO's rate capability and provides an extremely long cycle life. Thanks to its high potential, which is higher than the voltage where

main redox reactions of the electrolyte happen, LTO gets to stay away from the formation of passivation layers, further allowing the great cycling stability and the usage of its nanopowder. Consequently, LTO also demonstrates excellent low-temperature performance.[70]

Various research works have been done to improve the versatility of LTO anode materials, to increase the energy density of LTO as it is low for current technologies, or to further enhance its rate capability. Chen *et al.* grew LTO directly from titanium foils and made self-supported free-standing LTO nanosheet arrays that can deliver a capacity of 78 mAh/g at the ultrahigh rate of 200 C and achieve a cycle life of 3000 cycles at 50 C.[71] Zhang *et al.* developed LTO microspheres in combination with uniform reduced graphene oxide (rGO) coatings, that reached a high electrical conductivity and a higher capacity retention at high rates.[72] Li et al. doped rare earth element Sm into LTO crystal structure that significantly enhanced the specific capacity of LTO to over 170 mAh/g at 0.2 C.[73] Other attempts include mixing and compositing LTO particles with carbon materials[74], varying the morphology of the LTO particles[75] and downsizing the LTO materials into nanoscale[76].

Currently, LTO is not the major player among anode materials due to its shortcomings and high costs, but for some specific applications that require extremely rapid charging capability and long cycle life LTO is one of their best options.

1.4.2.3 Silicon-Based Anode Materials

1.4.2.3.1 Elementary Si Anode

Silicon (Si) has been a hottest research topic for LIB anode materials for years. The motivation is fairly simple: its super high theoretical specific capacity (~4200 mAh/g)[77], low cost and the understandable degeneration mechanism that is seemingly solvable.

As the best representative of group IVA elements that are considered as candidates (Si, Ge, Sn) for LIB anode materials, Si goes through the formation of alloying with lithium ions during lithiation process and eventually form $Li_{22}Si_5$ or $Li_{4.4}Si$ at a full lithiation. Among its peers, it has the highest theoretical capacity (vs. germanium 1625 mAh/g and tin 994 mAh/g), which is also over ten times specific capacity of graphite (372 mAh/g). Not only gravimetric capacity of Si is significantly higher than commercial graphite, considering its higher bulk density, Si also presents a much higher volumetric capacity (9781 mAh/g vs. graphite 837 mAh/g).[78] According to **Figure 1.10a**, at room temperature, the lithiation and delithiation voltage plateaus for Si are around 0.1 – 0.2 V and 0.4 V, respectively. The reasonably low lithiation potential improves the safety by reducing the formation of lithium metal, compared to graphite's low lithiation potential (~ 0.1 V), while Si is able to maintain a low delithiation potential so that the cell voltage will not be compromised.[79] When at elevated temperature (450 °C), Si could show reversible lithiation and delithiation curves with clear plateaus showing its different stages for lithiation. At room temperature, however, crystalline Si goes through a single crystalline-to-amorphous phase transformation during the first lithiation and remains amorphous afterwards.[80] After turning into amorphous state, the kinetics of lithium ion transport will be improved, which further benefits the electrochemical performance later on.

In addition to the favorable features of Si, it is also the second most abundant element in earth's crust, and it is environmentally benign.[80] The low cost of crude Si materials makes it promising for broad market applications. Based on **Figure 1.10b**, people are very optimistic and looking forward to the extensive commercialization of Si anode materials. From the year of 2019, the silicon anode based battery market is expected to increase exponentially, with over four times of the market in five years.
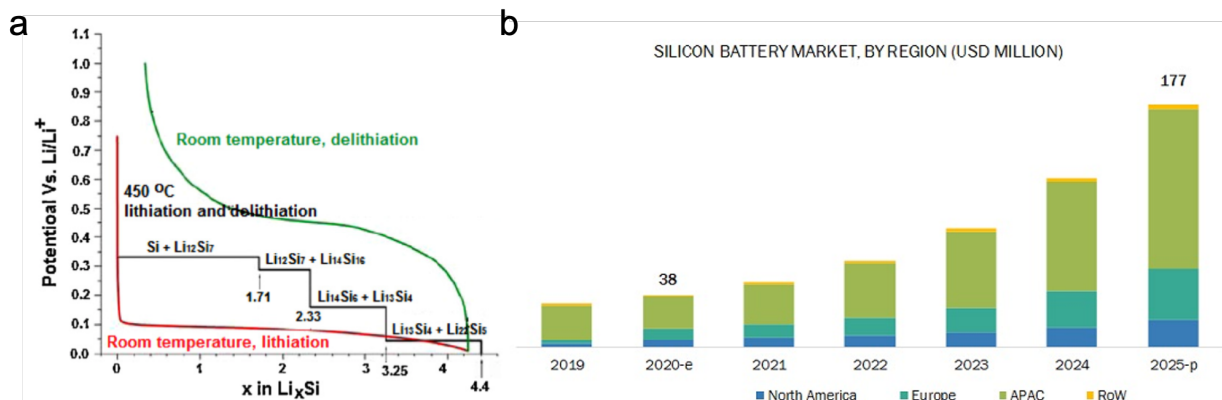
Figure 1.10 (a) Si electrochemical lithiation and delithiation curve at room temperature and high temperature. Black line: theoretical voltage curve at 450 °C. Red and green lines: lithiation and delithiation of crystalline Si at room temperature, respectively.[80] (b) Market forecast for silicon anode batteries by region.[81]

Where there great benefits, comes great costs. The problems that people have to solve in order to commercialize Si anode are severe. It is an impressive feature that Si has a theoretical capacity of ~4200 mAh/g, but at the same time, the accommodation of lithium ions through the formation of alloys forces Si to expand to 400% of its pristine volume.[80] As **Figure 1.11a** shows, the lithiation process gradually forces the Si to expand to a much bigger volume compared its original structure, at the same time destroying its crystalline structure to form amorphous alloy with lithium ions. This alloying process that turns Si from crystalline to amorphous is indeed irreversible during the whole battery charging/discharging process. Indicated by **Figure 1.11b**, in the initial discharging cycle, crystalline Si gradually and partially forms alloy with Li atoms and become amorphous Si. Until the stoichiometry of Li to Si has reached 3.5 ($Li_{14}Si_4$), all the crystalline Si has completely gone and transformed into amorphous phase, when the capacity has

reached approximately 3560 mAh/g. When the lithiation keeps going, eventually crystalline

$Li_{15}Si_4$ is formed and the capacity reaches 4000 mAh/g. During the first delithiation or charging

process, the crystalline $Li_{15}Si_4$ retains and coexists with amorphous Li/Si alloy until enough

lithium ions have been extracted from Si and the amorphous Li/Si remained continues the

delithiation process.[82] Ever since the first cycle, Si has turned amorphous and maintains

amorphous in the following cycles.
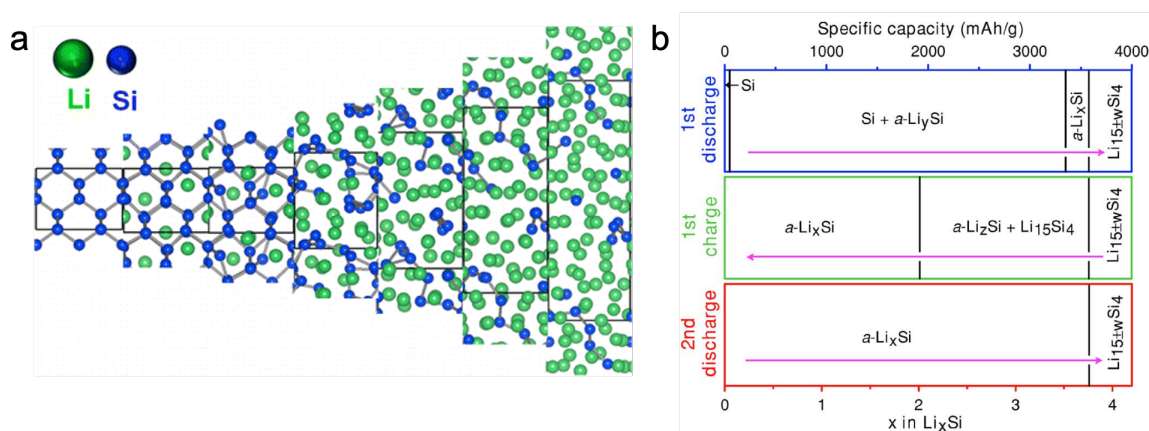
Figure 1.11 (a) Configurations from the lithiation algorithms of Si model without a solid-

vacuum interface, consisting of four Si atoms per layer.[83] (b) Phase diagram describing the phase

that form during the charging/discharging cycling of a Li/Si electrochemical cell between 0.005

V to 0.9 V at room temperature.[82]

As a result of the severe volume expansion and the significant phase change, Si

electrodes experience multiple failure mechanism. As **Figure 1.12** shows, three possible reasons

can lead to the final failure of the electrode and battery. Figure 1.12a is a result of structural

instability. After the repeated lithiation and delithiation process of Si, the particles turn into

smaller amorphous pieces, eventually causing cracking and pulverization. This phenomena

further results in problems in Figure 1.12b and c. When Si particles pulverize and crack, the particles start to lose electrical and physical contact with conductive carbon and binder, which will make those Si particles isolated from the electrical circuit and even fall apart from the current collector and the electrode, eventually causing significant capacity loss for the battery. Solid-electrolyte interfaces (SEIs) are a passivation layer of organic and inorganic lithium salt that is formed on the surface of anode materials during the lithiation stage. Moderate amount of SEIs can improve the lithium ionic conductivity of the anode materials that are benign to the battery. However, Si particles continuously going through enormous volume expansion because of lithiation will inevitably break the SEI layers on the particles surface. Therefore, when the fresh surface is exposed again to the electrolyte, new SEIs will form on the surface of the fresh particle surface. After many cycles, the repetitively process of SEIs collapse and formation not only leads to the increasing resistance of the anode materials because of the excessive SEIs, but also consumes a great amount of electrolyte that further contributes to the termination of the battery life.
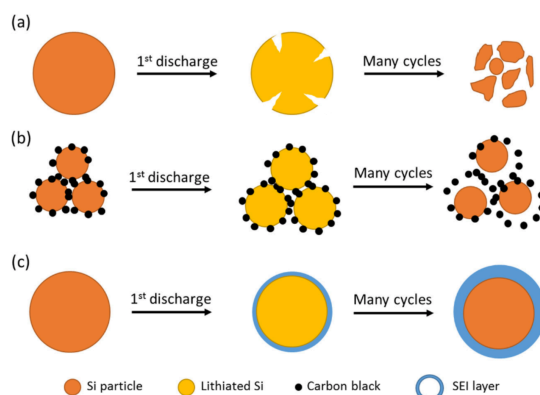
Figure 1.12 Failure mechanism of Si anode: (a) cracking and pulverization; (b) volume expansion and loss of electrical contacts and (c) formation of excessive SEI.[45]

Such problems above have doubtlessly hindered the practical application of Si anode materials. The loss of electrical contact induced by the particle pulverization explains for the poor cycling stability and rapid capacity decay of Si anodes. The repeated formation of SEIs limits the Coulombic efficiency, which accelerates the capacity loss in a battery using Si anode. Accordingly, to solve the problems caused by volume expansion has always been a primary concern for researchers.

A general idea to improve Si anode performance is to decrease the size of the particles. Most commercially available Si sources are bulk particles in hundreds of microns' scale. It is well-acknowledged that Si nanoparticles have a better performance. Equation (1) and (2) demonstrate the lithium ion diffusion and particle fracture resistance for spherical electrode particles. In Equation (1), τ stands for the diffusion of lithium ions. L is the diffusion length for lithium ions. D_{Li} is the diffusion coefficient of lithium ions within the material particles, an intrinsic value of the material. Equation (1) tells us that for a certain material, a shorter diffusion length, i.e. a smaller particle size, brings up a short diffusion time. Therefore, compared to bulk particles, nanoparticles will allow lithium ions to go through the particles thoroughly within a certain time, leading to a smaller concentration polarization inside the electrode material and an improved rate performance. In Equation (2), G is the energy release rate during the lithiation process. Z is a dimensional number of order unity, a constant. σ is the representative stress. h stands for the feature (particle) size. E is the Young's modulus. As demonstrated by Equation (2), the energy release is positively correlated to the particle size h, which means the bigger the particles are, the more energy they will need to release.[84] When G is below the fracture energy, the particle will stay intact. Otherwise cracks will form and the fracture will occur. Bringing all the parameters for silicon, the corresponding critical particle sizes can be obtained are 150 nm

for crystalline Si and 870 nm for amorphous Si, which implies nanoscale Si particles can prevent themselves from significant fractures. By any means, the usage of Si nanoparticles instead of macroscale bulk Si can effectively improve the structural stability during the lithiation and delithiation process, and reduce the consumption of electrolytes from repetitive formation of SEI layers.
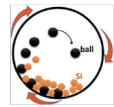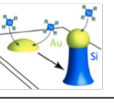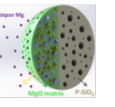
$$\tau = \frac{L^2}{D_{Li}} \quad (1) \qquad\qquad G = \frac{Z\sigma^2 h}{E} \quad (2)$$

Four main methods are common for the production of silicon nanoparticles according to **Table 1.3**. High-energy ball-milling (HEBM) is a scalable method that is suitable for industrialization and large batches. HEBM utilizes mechanical energy (friction, collision, impact) to break down particles or form new chemical bonds.[85] The biggest advantage of HEBM compared to other methods is its great scalability and high yield. It also has a safe and rather simple operation process that makes the overall cost affordable for commercial production. The as-obtained primary Si nanoparticles are generally in the range of 10~200 nm. However, because of the exposed high-energy Si surface after the HEBM process, the primary particles usually go through a severe secondary-aggregation which causes the final particle size up to microscale.[86] Shen *et al.* uses ball-milling to produce nanosized Si particles, but found out further steps such as HF etching and carbon coatings are still necessary to reach a stable performance for the milled Si particles.[87] Due to its flexibility with the reaction and feasibility for new chemical bonds, HEBM still has a big potential for the production of Si anode materials. Chemical vapor deposition (CVD) is extremely common for Si nanostructure production in literatures but rarely used in industry. CVD can directly produce Si nanoparticles using SiH_4 as the source. It can also

produce one-dimensional Si nanowires via substrates with special morphology[88,89] or hollow Si nanostructures combined with etching process[90]. In the well-known work for Si nanowires, Chan *et al.* established a vapor-liquid-solid growth via CVD with gold nanoparticles as the catalyst and SiH_4 as the silicon source. The obtained Si nanowires are able to maintain its structural integrity after cycles and thus deliver an improved cycling stability and the rate performance.[91] Because CVD uses gas sources at high temperatures and deposit at atomic levels, the yield is low while the cost is high. However, the process is highly controllable as it can produce nanoparticles in different sizes, thicknesses and morphologies with desirable features. Metal-assisted chemical etching (MACE) utilizes metal ions on the surface of Si particles to etch into the particle, forming Si nanowires or porous Si nanoparticles.[92] They are similar to CVD in the scale, but instead of bottom-up, MACE shapes Si particles in a top-down way. Ge *et al.* uses Si nanoparticles as the starting material and dopes the nanoparticles with boron. After the doped particles absorbs Ag ions, the Ag^+ is able to etched the surface of Si particles and produce nanoporous Si particles.[93] Magnesiothermic reduction (MR) utilizes the reaction between Mg and SiO_2 to produce nanoporous Si particles. After reacting with SiO_2, Mg is oxidized into MgO and Si is generated accordingly. Based on the substrates, the final product can be porous Si particles or uniform Si nanoparticles. Jia *et al.* uses magnesiumthermal reduction on a SiO_2 template and obtained three-dimensional mesoporous Si frameworks with the particle size around 500~600 nm and the primary particle size around 30 nm. The according anode material shows a better cycling stability than commercial nano-Si due to the improved contact between Si particles.[94] MR process is affordable and simple in terms of the raw materials and the conversion reaction. However, at the same time, MR has a low efficiency due to the further side reaction between Mg and Si.[95,96]

Table 1.3 Comparison of processes, morphologies, production costs and advantages/disadvantages between different fabrication methods of nanosilicon.[45]

Methods	Process	Product	Production; cost of raw material	Features
High-energy Ball-milling (HEBM)		Si nanoparticles (SiNPs) (400-2000 mAh/g)	~4 kg/h; ~$1/kg metallurgical silicon	High yield, scalable, low cost; Secondary aggregation,
Chemical Vapor Deposition (CVD)		Si nanowires/tubes, SiNPs (>2000 mAh/g), and thin films	0.75 mg/h; ~$100/kg of SiH_4	Controllable, diverse; High cost, unsafe, low yield
Metal-assisted Chemical Etching (MACE)		Porous SiNPs	0.1-10g/h; ~$200/kg of Si wafer	Controllable, diverse; High cost, unsafe
Magnesiothermic Reduction (MR)		Hollow Si spheres	0.1-0.5g/h; ~$2/kg of Mg	Controllable, diverse; Low efficiency

Beside or along with scaling down Si to nanoparticles, extensive efforts have been spent on various modification and coating of the Si particles. Because of the volume expanding nature of Si during lithiation, rigid coatings with void space around Si particles are an effective and popular way to protect the particle from pulverization. Liu *et al.* revolutionarily devised the yolk-shell structure for carbon coated Si particles. Starting from Si nanoparticles, they take advantage of the oxidation layer SiO_x on the surface and uses it as the sacrificial layer. Carbon is further coated on the outer surface. After etching the SiO_x layer, the yolk-shell structure is obtained with an exceptional cycling stability at its time.[97] This design as many benefits, such as preventing the particles from cracking and electrical disconnection, reducing the repetitive formation of SEI layers and improving the particles contact. Because of its great efficacy, similar methods have been reported with different structural designs such as the encapsulation of yolk-shell Si particles in carbon tubes to further improve the cycling stability and rate performance[98], a pomegranate

design for high areal loading and high Coulombic efficiency[99], and strong and flexible graphene cages replacing the amorphous carbon to coat Si microparticles[100]. TiO_2 coating becomes the popular substitution of the shell for this design due to its outstanding mechanical strength. Jin *et al.* demonstrated a TiO_2 coating that can endure a 5x strength compared to amorphous carbon coatings, with which the cell has an extended cycle life.[101] Yang et al. claimed that amorphous TiO_2 shows elastic behaviors that can effectively buffer the volume expansion of Si and works better than crystalline TiO_2.[102]

Stronger binders that can provide a better interconnection is another way of improving the Si anode performance. Conventional binder polymers such as poly(acrylic acid) (PAA) and carboxymethyl cellulose (CMC) are not able to sustain the electrode integrity after the Si particles start to crack. Wu *et al.* reported an in situ polymerization for a conductive hydrogel matrix around Si particles that can provide a stronger support and connection for the particles through the crosslinked property, and improve the capacity retention at high current density at the same time.[103] Later on, Wang *et al.* came up with the self-healing polymer utilizing the non-covalent hydrogen bonds that can repetitively break and form during the volume expansion and contraction, in order to keep the structural integrity of the silicon particles in the electrode. Instead of expensive Si nanoparticles, this method can be applied to low-cost bulk Si particles.[104] Zhao *et al.* introduced a new conductive binder PPyMAA that can effectively improve the initial Coulombic efficiency (ICE) in combination with a commercial high tap-density nano-Si.[105]

Considering the loss of lithium ions from the electrolyte during the first cycle, and the huge volume expansion during the lithiation process, prelithiation for Si becomes attractive to alleviate these problems. Liu *et al.* initially prelithiates the Si nanowires following their previous work.[106] Forney et al. prelithiates Si/carbon nanotubes with stabilized lithium metal powder to

obtain anode materials eliminating 20 – 40% first cycle irreversible capacity loss and the corresponding full cell shows an impressive cycling stability.[107] Zhao *et al.* prelithiates Si particles and oxidizes the surface to form Li_2O which allows the prelithiated Si particles to be air-stable and protect the structural integrity at the same time. The obtained material has an ICE over 90.8% and remains stable even after being exposed to ambient air.[108]

Beside methods using or incorporating the strategies mentioned above, other creative works also have contributed to the pool of Si anode materials manufacturing. Wang *et al.* grows interconnected Si networks via plasma-enhanced chemical vapor deposition (PECVD) directly on the current collector and further coats the surface of Si with carbon. This network without additional binder or conductive carbon, achieved a stable cycling performance and reached a capacity over 1200 mAh/g at an ultrafast rate of 7 C.[109] An et al. designed a process starting with Mg_2Si. After nitration and etching, the final product is extremely nanoporous and able to sustain its structure during the lithiation process.[110] Chen *et al.* developed a Si 2-dimensional nanosheet based on MR reaction that is mesoporous and has a short lithium-ion diffusion pathway. As a result, the obtained material delivers an outstanding rate performance.[111]

Due to the severe problems Si anode materials are facing, the combination of Si and graphite materials is a growing trend for commercialization.[65] The composite is expected to increase the specific capacity of graphite while not compromising too much of its stability and Coulombic efficiency. Ko *et al.* invented a novel architecture that Si nanoparticles are coated onto the surface and into the pores of commercial graphite particles. Furthermore, the Si particles are coated with more carbon. This hybrid anode material combines the stability of graphite and the high capacity of Si together and achieved an overall enhanced electrochemical performance.[112] Similarly, Ma *et al.* incorporates Si into the graphite macropores and obtained a

composite material with capacity over 527 mAh/g and a high ICE of 93%.[113] Park et al. prepared a structure containing titanium and silicon alloy core and nanoporous silicon as the shell. When further mixed with graphite, the composite electrode shows good cycling stability.[114] Si/graphite composite anode materials have great potential for application. As a result, many countries formulated policies regarding the benchmark for the development of Si/graphite anode materials, and key players worldwide also released their products with Si as a component.[115]

Nowadays, improving the cycling stability of Si anode materials is still the primary challenge for both academic and industrial research. At the same time, the use of low cost materials and procedures is an essential requirement in order to put the research into practical applications.

1.4.2.3.2 SiO$_x$ Anode

Silicon oxides (SiO$_x$) are a promising family as the anode materials. Researchers suggested that the SiO$_x$ could be a random mixture of Si and SiO$_2$ nanostructures. Based on the chemical stoichiometry, x can vary. The ones that have x value close to 1 (SiO) are the most attractive candidates for the anode market.

At a full lithiation process, a theoretical capacity of 2680 mAh/g can be reached for SiO materials. Similar to Si, SiO also goes through big volume expansion (~200%). It is generally accepted that Li$_x$Si alloys, lithium silicates (Li$_4$SiO$_4$, Li$_2$Si$_2$O$_5$, Li$_6$Si$_2$O$_7$, Li$_2$SiO$_3$) and Li$_2$O are formed during the first lithiation of SiO. Li$_x$Si is reversible during the lithiation and delithiation as lithium ions can be extracted and converted back and forth. Lithium silicates and Li$_2$O are considered irreversible components. Therefore, they can greatly lower the ICE (~60%) of SiO and cause big challenges for applying SiO into full cells. On the other hand, the irreversible

components serve as a buffering matrix against the volume expansion during the lithiation and delithiation, hence improving the cycling stability of SiO. Despite the significant volume expansion for SiO, the capacity retention for SiO after many cycles is much higher than Si.[116]

Beside the further improvement of cycling stability for SiO, other serious problems remained for SiO are related to the low ICE and low rate capability. There are some similar efforts done to SiO in comparison of Si including conductive coatings and core/shell structure designs to improve its cycling stability and rate performance. Extensive research has been carried out in order to improve the ICE of the anode. Seong *et al.* developed a prelithiated SiO/C anode material by letting the lithium metal pre-react with the anode for 48 hours before testing the cell. The ICE has been improved to 72.8% and the following Coulombic efficiency quickly rises up to over 90%.[117] From the same research group, they developed a double-layered anode design, where inside the anode the active material is attached to a copper mesh that is layered on lithium powders. Because of the excessive amount of Li metal in the cell configuration, the ICE is able to reach 100%.[118] Kim *et al.* used a resistor to conduct a controllable and sophisticated short-circuit process with voltage strictly monitored between the SiO electrode and Li metal foil. After the short-circuit, the SiO electrode is paired with NCA to construct a full cell, which reached an ICE of 94.9%.[119]

Due to the inhomogeneous nature on the atomic-scale, SiO is thermodynamically unstable and it tends to disproportionate into Si and SiO_2.[116] This is a feature that can be greatly taken advantage of. In fact, researchers have found that this reaction will happen during heat treatment and some other conditions such as high energy mechanical milling as shown in **Figure 1.13**. Yang *et al.* uses high energy mechanical milling to react lithium metal and SiO during the milling process so that Li_2O and lithium silicates are pre-formed before the first lithiation

process, and nanocrystalline Si is generated. By doing this, an ICE of 81% is reached.[120] Yom *et al.* discovered that when SiO is treated with Li under 600 °C, beside the transition from SiO to Si, there will also be a layer of Li_2O and lithium silicates formed on the surface of the solid particles that helps improve the ICE to over 80%.[121] Considering the existence of inactive material SiO_2, Yu *et al.* etched the SiO_2 with NaOH and obtained crystalline Si embedded inside porous SiO_x matrix. They improved not only the Coulombic efficiency, but also the rate capability.[122] Those designs are seeking for a balance between the SiO_x and Si.
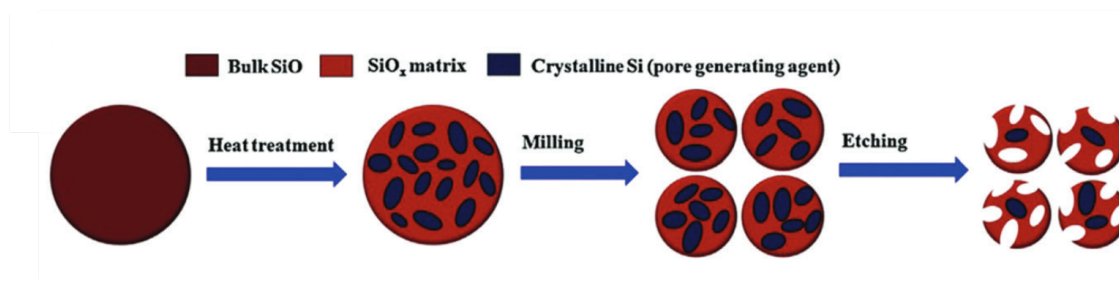
Figure 1.13 Schematic illustration of the process of SiO disproportionation into Si and SiO_2.[122]

As a result of its better cycling stability, SiO_x is applied in commercial batteries as extensively as Si if not more.[123] However, for commercial applications, a high ICE is same critical as a long cycle life since a low ICE means the consumption of the most expensive component – cathode materials in LIBs.

1.4.2.4 Lithium Metal Anode

As Figure 1.8b shows, lithium metal has the highest theoretical capacity (3860 mAh/g) among all the anode candidates. Lithium is the lightest member of the alkali metal group, with the smallest atomic radius of all metals, which also contributes to its ultrahigh capacity. Lithium

also has the lowest electrochemical potential (-3.04 V vs. standard hydrogen electrode or 0 vs. Li/Li^+), which makes the full cell with lithium metal anode able to output the highest possible voltages and high energy densities.[124] Lithium metal is technically a conversion type anode material, but unlike other conversion type materials such as Fe_3O_4, lithium metal is hostless as it goes through the reaction from lithium ions to lithium metal during lithiation and the reverse during the delithiation as Equation (3) indicates.

$$Li - e^- \leftrightarrow Li^+ \qquad (3)$$
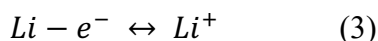
Similar to other alkali metals, Li has high reactivity and reacts slowly in dry air. It can also react with trace amount of water rapidly. Therefore, Li metal will instantaneously get oxidized into Li_2O, $LiOH$, Li_2CO_3 and Li_3N by O_2, H_2O, CO_2 and even N_2 in ambient air environment. As a result, Li metal is not accessible in the nature. Instead, commercial Li metal products are isolated from the rich lithium mineral resources via electrolysis.[125]

In spite of the minor difficulty during the metal extraction, Li metal is still a promising and attractive anode candidate for next-generation lithium ion batteries. In fact, LIBs that use Li metal as the anode have been given a specific name of lithium metal battery (LMB). The ultrahigh specific capacity and energy density of Li metal have endowed unique advantages to LMBs. As **Figure 14a** shows, by replacing graphite anode with Li metal, the thickness of the anode can be reduced by almost 2/3. As a result, the overall cell specific energy can be increased by ~35% and the energy density by ~50%. Especially if a suitable solid-state electrolyte is introduced to combine with the usage of Li metal, substituting flammable liquid electrolytes, it will impose both safety and thermal management mass and volume requirements at a pack level.[126] To compare LMBs with a broad choices of power sources in **Figure 14b**, one can tell with the use of conventional LIBs, the energy density and specific density are both compromised

compared to gasoline. A small leap to LMBs is to use the Li-LMO configuration, with which both the energy density and the specific energy can be improved greatly. When we keep moving forward into the future, the application of Li-air battery can ideally reach a similar energy density to gasoline eventually. Even though there are still numerous obstacles to overcome towards the further applications of Li-S or Li-air batteries, the first difficulty for us to conquer is the development of more reliable and stable Li metal anode.
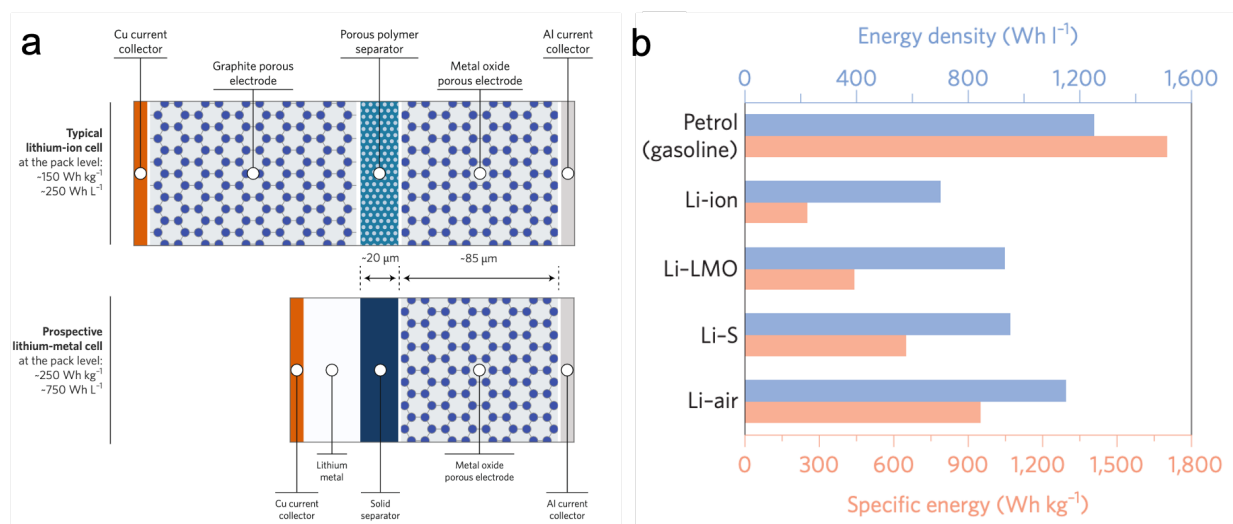
Figure 1.14 (a) Schematic illustration of the configurations of traditional LIBs and lithium metal based LMBs.[126] (b) Bar chart showing the practical specific energy (pink) and energy densities (blue) of petrol (gasoline), traditional LIBs and current state-of-the-art LMBs. Battery casings, separators and electrolytes are all taken into account.[127]

There are several critical issues that need to be addressed for the development of Li metal anode as **Figure 1.15a** shows. During the cycling process, SEI will form on the surface of Li metal. Due to the nature of Li metal anode, there is infinite volume expansion based on the

extent of Li stripping and plating. As a result, when the volume expands, the SEI could crack and cause the isolation of dead Li. The repeated formation of SEI on the fresh Li surface consumes excessive amount of electrolytes which leads to low Coulombic efficiency of the battery. At the same time, dendrite growth can cause short-circuit in the cell, leads to thermal runaway and possible combustions. Once Li metal contacts the environment outside the battery, the high reactivity of the metal could induce bigger safety hazards.
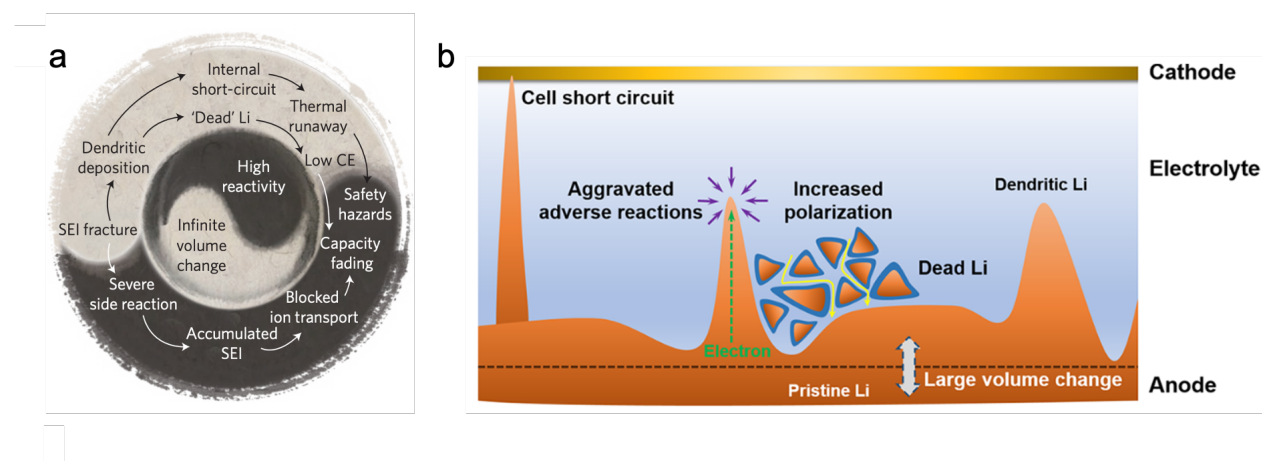
Figure 1.15 (a) Correlations among the different challenges in the Li metal anode, originating from high reactivity and infinite volume change.[127] (b) Schematic illustration of the short-circuit process from Li dendrite growth during the cycling process in LMBs.[125]

Figure 1.15b demonstrates the pathways of cell failure in more detailed manners. When the lithium ions nucleate non-uniformly on the surface of Li metal, dendrite starts to form and grow. Li dendrite could grow to the extent that it could seemingly penetrate the separator and immediately cause cell short-circuit. Short-circuit can cause severe safety issues especially at a battery pack level, which is also unpredictable and instantaneous. The surface area of Li metal will significantly increase due to the existence of Li dendrite. Because of the high reactivity of

Li, the high surface area could lead to unnecessary side reactions between Li and the electrolytes, causing excessive and irreversible consumption of both Li metal and electrolytes, which is both a waste and a trigger for the cell failure. Low Coulombic efficiency and irregular capacity decay can manifest this phenomenon. The huge volume expansion during the lithiation process causes the SEI fracture, promoting more dendrite growth through the cracks. While during the delithiation process, the Li stripping from the kinks or roots of the dendrite can easily break the electrical contact between the Li dendrite and the substrate, producing dead Li.[127] This process is irreversible and harmful to the cell. Li dendrite and dead Li make original dense Li metal foil into porous and uneven Li structure. The existing pores and dead Li particles considerably prolongs the diffusion pathways for Li^+ and electrons inside the anode. At the same time, the excessively formed SEI layers start to compromise the electronic conductivity of the anode. Consequently, a large polarization during cycling process will be rendered, directly leading to a poor rate capability and a low energy efficiency. Given those severe problems above, it is challenging yet critical to overcome the issues that are causing the safety concerns, cycling instability, poor rate capability and low energy efficiency during the use of Li metal anode, before we can possibly commercialize LMBs.

To address different aspects of existing challenges for Li metal anode, a great amount of efforts towards the improvement of the metal anode itself, electrolytes and separators are devoted into LMB researches.

In order to alleviate the problem of SEI fractures, constructing artificial SEIs is one common way. An ideal SEI layer should be chemically and electrochemically stable, and mechanically robust to sustain the stress from Li dendrite growth. Normally, dependent on components of the electrolytes, multilayer or mosaic structures of SEIs can be formed on the

surface of the anode materials.[128] In most common $LiPF_6$ liquid electrolyte system, SEIs are usually consisted of LiF, Li_2O, LiOH, $LiP_xO_yF_z$ and various lithium carbonates.[129] They are usually electrochemical stable, but do not possess mechanical strength due to their nature of salts. Artificial SEIs can form through the exposure of Li to certain chemicals and solvents. SEIs resembling the natural SEI components are a favored option because their stability and compatibility.[130] Yan *et al.* exposed Li metal to a common liquid electrolyte additive – fluoroethylene carbonate (FEC). A dual layer film was able to form on the surface of Li with inorganic and organic layers condensed in inner and outer parts, respectively, due to the different reactivities. The components of this artificial SEI resemble the natural SEI formed on Li metal, but more uniform and dense that can effectively improve the Li nucleation and hamper the dendrite growth.[131] Similarly, Lang *et al.* soaked Li metal into polyvinylidene fluoride (PVDF) solution and formed a dense and uniform layer of LiF on the surface of Li metal. The integrity of the artificial LiF layer remains undamaged after cycling. The cycling stability of the according LMB cell is greatly improved as a result.[132] Zhu *et al.* proposed a graphitic-inorganic bilayer artificial SEI which is consisted of a graphitic layer and a layer of inorganic components (LiF, Li_2O, Li_3N and Li_2CO_3), which has strong mechanical strength and stiffness and is able to endure the stress from the Li dendrite growth while effectively allowing lithium ions and electrons to pass through.[133] Versatile works constructing artificial SEIs through coating polymers or small molecules that can form strong chemical bonds with Li.[134] Gao *et al.* used a reactive polymer composite consisting of polymers, graphene oxide sheets and nanoscale salt particles that is homogeneous and mechanically strong itself, whereas a passivating layer formed on the interface between the composite and Li metal is dense and stable to improve the efficiency of Li deposition under lean electrolyte conditions.[135] Liu *et al.* developed a Li-ion conducting artificial

SEI with Cu_3N nanoparticles and styrene-butadiene rubber (SBR). Li metal can react with Cu_3N to produce ionic conductive Li_3N. The obtained dense SEI layer can significantly suppress the growth of Li dendrite and greatly improve the Coulombic efficiency of the Li metal anode to 98%.[136]

SEI breaking on Li metal can also be attributed to the infinite volume change of during the lithiation and delithiation. To address this issue, constructing Li metal host is a popular method. Li host with a robust structure will provide defined pores or channels for Li deposition. At the same time, the functional groups in the Li host can implement uniform Li nucleation and further deposition, effectively preventing uneven growth of dendrite. Zhang *et al.* took advantage of carbonized wood and created a porous conductive framework with well-aligned channels as Li host material. Molten Li can infuse into those channels and become Li/C electrode, which is able to guide Li deposition and confine the Li metal inside the channels to prevent Li dendrite growth.[137] Due to the small size of the pores or channels, the surface tension for molten Li to infuse could be high and hamper it from entering. Therefore, Liang *et al.* has developed lithiophilic 3-dimensional scaffold that allows molten Li to infuse freely. This host has a carbon nanofiber scaffold that is highly conductive and porous. They then coated the nanofiber with Si nanoparticles via CVD which endows the structure with lithiophilicity. The obtained anode successfully maintains its volume unchanged in response to Li stripping and plating process. Due to the conductive property of this scaffold, the voltage hysteresis especially at high rate is significantly reduced.[138] Similarly, Liu *et al.* also used electrospinning to acquire a stable polymeric backbone. A conformal layer of ZnO was coated via atomic layer deposition (ALD) in order to render the surface lithiophilic, and let molten Li to be drawn into the porous matrix. The according cell can endure a high current density with modest polarization.[139] Unlike graphene,

reduced graphene oxide (rGO) usually has good lithiophilicity, while still possessing the strong mechanical intensity from layered graphene structure. Lin *et al.* fabricated a layered rGO film and readily infuse molten Li into the film within minutes. The obtained Li-rGO films have good flexibility and mechanical strength. The layered structure can efficiently accommodate Li deposition and achieve a close-to-theoretical capacity (3390 mAh/g) without significant volume change. The according LMB delivers a smaller voltage hysteresis and excellent rate capability at 10 C.[140] Xue *et al.* combined interconnected 3-dimensional graphene that offers toughness and electrochemical stability with 2-dimensional silver nanowires network that provides smooth and ultrafast electron transportation channel and non-nucleation barrier sites. They have managed to obtain long-range ordered structure with Ag nanowires uniformly distributed on the graphene surface. This Li host shows superior stability and Coulombic efficiency especially at high current densities.[141]

Extensive researches on the development of electrolytes and additives for Li metal anode have been carried out including various types of solid-state electrolytes with structural stability and high mechanical strength and electrolyte additives that improve the SEI stability. Details will be revealed in 1.4.3.

1.4.3 Electrolyte Materials Development

Electrolyte is a critical component in batteries as they directly carry and transport lithium ions between cathodes and anodes. Electrolytes usually contain lithium salts, solvent and additives, each one having a significant impact on the cell performance. Some basic requirements for electrolytes include high ionic conductivity, good electrochemical stability within the cell voltage window and capability of forming stable SEI layers. As the development

of advanced LIBs, more desirable features are expected, such as low or non-flammability, high thermal stability and high Li^+ transference number for good kinetics and transportation. For next-generation LIBs, especially high-voltage batteries and LMBs, advanced electrolyte development becomes extraordinarily important since current electrolyte technologies are not satisfactory for those applications.

Currently, based on the cell configuration, there are several commercially available liquid electrolyte options. One molar $LiPF_6$ in ethylene carbonate (EC) / diethyl carbonate (DEC) (vol. 1:1) is a widely adopted liquid electrolyte that is extensively used both in commercial LIBs and academic researches. It has high overall ionic conductivity, usually above 10^{-3} S/cm, and low activation energy so that it would still have good transportation properties under low temperatures.[142] EC has high dielectric constant and can supply high ionic conductivity. While DEC or another linear carbonate dimethyl carbonate (DMC) can decrease the viscosity of the mixed solvent and help improve the electrochemical stability of SEI layers.[143] Generally this electrolyte satisfies most requirements for LIBs and thus is commonly used for various types of batteries. However, to cater for the higher demand for next-generation LIBs, we have to confront with the problems from the nature of this electrolyte. $LiPF_6$ is not a chemically stable salt. In fact, it instantaneously reacts with trace amount of water to produce hydrofluoric acid (HF) that is toxic both to the environment and lives. It is also thermal instable as the electrolyte starts to decompose at ~80 ºC, which disables its application in high temperatures such as aircrafts. Moreover, the use of organic solvent can potentially induce serious accidents including spontaneous combustion of EVs.[144] Beside all the safety concerns, the energy efficiency of this electrolyte needs improving as well. In spite of its seemingly high ionic conductivity, only a small portion of the ionic conductivity comes from lithium ions, which makes the majority of

energy wasted on the transportation of PF_6^- anions instead of being stored as electrochemical energy. Even though $LiPF_6$ electrolyte is able to serve most of the cell configurations and maintain electrochemical stable in common voltage windows, it cannot accommodate high voltage (> 4.3 V) for a long-term cycling stability without additional additives.[145] The problems above leads to worse consequences when $LiPF_6$ electrolyte is used for LMBs because of the excessive consumption of electrolyte materials and the high output voltage of the LMBs.

Beside $LiPF_6$ in organic solvent electrolyte, there are a couple of more recently discovered electrolytes that are not yet applied in commercialization because of the immaturity of the development or inevitable problems hindering the practical applications. However, they can still be promising and advantageous in terms of academic researches for novel materials exploration. Some other analogs of $LiPF_6$ including $LiClO_4$, $LiBF_4$, $LiAsF_6$. For the sake of commercialization, they all face different challenges such as high explosivity, poor properties for SEI formation and low conductivity, high toxicity respectively.[146] On the other hand, $LiClO_4$ in propylene carbonate (PC) has high operating temperature that enables high temperature battery research. $LiBF_4$ shows a less sensitivity to water compared to $LiPF_6$ and brings convenience during manufacturing and operations. The anodic stability of $LiAsF_6$ can be high, the electrolyte remaining stable up to 4.5 V on various cathode surfaces.[142] A newer Li salt with oxolato ligands named LiBOB ($LiBC_4O_8$) has been given attention because it is able to form stable SEI layers, anodically stable, thermally stable and decomposing into less corrosive products in presence of moisture. However, it is still far from meeting the rate capability requirement for commercial applications.[147] Another Li salt lithium bis(trifluoromethanesulfonyl)imide (LiTFSI) has been popular due to its significant improvement in stable SEI formation and lower mobility for the anions. It is so far the best acknowledged electrolyte for Li-sulfur battery due to the lower

solubility of polysulfide ions in its solvent (1,3-dioxolane and dimethyl ether). However, it has a narrow voltage window because it provokes aluminum pitting corrosion.[148] Researchers have discovered that a sophisticated mixture of multiple electrolytes can lead to an improved performance due to the combining advantages. Zheng et al. developed a LiTFSI-LiBOB dual electrolyte with 0.05 M $LiPF_6$ as an additive. The resulting hybrid electrolyte shows a significantly improved charging capability and cycling stability of LMBs thanks to the generation of a robust and conductive SEI layer.[147]

As repeatedly mentioned above, SEIs play a crucial role for cell performance. SEI, i.e. solid-electrolyte interface, is a passivation film formed during the cell cycling. SEIs are generally believed to exist on the surface of electrode material particles and they are especially involved for the anode materials performance. The reduction potential for organic solvents is lower than 1.0 V (vs. Li/Li^+). Therefore, during the cycling process when Li is exposed to the electrolyte and a current is applied, immediate reactions happen and form SEI layers on the interface between electrode materials and electrolytes.[130] For most organic-solvent-based electrolytes, SEI components are highly similar, usually including LiF, Li_2O, LiOH, Li_2CO_3, $ROCO_2Li$ and other organic lithium salts.[149] Not only the chemical composition of SEI layers is important for cell performance, crystallinity, morphology and structure, thickness and density all matter to a large extent. Two models are popular and supported regarding the SEI structures and the arrangement of the lithium salts. As **Figure 1.16a** shows, Mosaic model proposes in SEI, lithium salts are distribute in blocks as heteropolymicrophases. It is well-acknowledged as it agrees with various experimental measurements.[150] On the other hand, multilayer model is brought up demonstrating SEI forms in an ordered way where the same species deposit into a layer (**Figure 1.16b**).[151] Unlike a lot of theories, it is not such case that bends to "one or the other" rule. Using

cryoelectron microscopy (cryo-EM) Li *et al.* suggests that upon the usage of different electrolytes, SEIs can form diverse structures.[128] Simply with $LiPF_6$ in EC/DEC electrolyte, Mosaic SEI is formed on lithium dendrite for lithium metal anode, which is unfavored since the high crystalline regions can pinch the dendrite and generate dead Li. However, with the assistance of some additives, such as FEC in their work, the formation of multilayer SEI structure is promoted. The multilayer structure is more uniform and thus has higher mechanical stability that can sustain the Li deposition and extraction from the SEI shells.
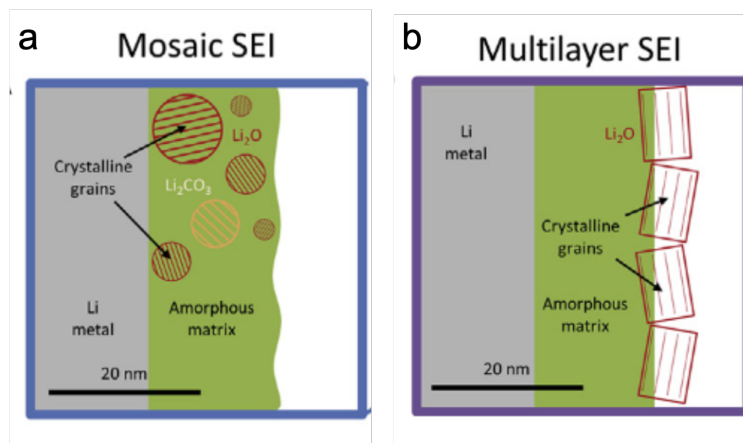
Figure 1.16 Schematic illustrations of two models for SEI formation on electrode materials surface. (a) Mosaic model. (b) Multilayer model.[128]

Like mentioned above, additives in electrolytes can have a strong impact on SEI structures and further affect the cell performance. Based on the main purposes and the working mechanisms, electrolyte additives can be categorized into SEI forming improver, cathode protecting agent, $LiPF_6$ stabilizer, safety protecting agent and Li deposition improver.[152] Among

them, SEI forming improver is the most popular and common type, including the widely adopted vinylene carbonate (VC) and FEC. Those additives can coat the electrode materials with a layer of organic components. VC is a typical polymerizable monomer additive that can free-radically polymerize under electrochemical induction. As a result, a stronger SEI containing stable and mechanically strong polymer will be formed. The presence of VC in the electrolyte can polymerize on lithiated graphite, effectively suppressing both electrolyte solvent and salt anion reduction.[153] Furthermore, the corresponding robust SEI layer can endure the huge volume expansion during Si particles lithiation better, and thus significantly improve the cycling stability of Si anode materials.[154] FEC can decompose into a HF molecular and a VC molecule under SEI-forming potentials. The resulting VC takes effects as mentioned. HF molecules are able to react immediately with alkali lithium salts including Li_2O, LiOH and Li_2CO_3 to produce more stable SEI component LiF molecules. When applied for Li metal anode, HF also helps shape SEI layers on lithium dendrite and encourage more even and uniform Li deposition. Therefore, FEC is especially favored for LMBs and batteries that need to be charged a fast rate or a low temperature as Li metal plating is inevitable in those situations. Other types of additives can possibly scavenge water molecules and dissolved metal ions, impede $LiPF_6$ decomposition, reduce the flammability and overcharge and etc. to improve the cell performance.[152]

For unstable anode materials such as Si and Li metal, modifying SEI components is not enough to conquer the problems. Like it has been mentioned, for most liquid electrolytes, despite the fact they have high ionic conductivities, the majority of which comes from the mobility of anions instead of Li ions. The redundant transportation of anions can directly lead to heat generation that lowers the energy efficiency, excessive SEI formation that increases the cell impedance and consumes the electrolyte, and irregular Li metal electrodeposition that results in

Li dendrite growth and explosive hazards.[155] To address this challenge, it is vital to introduce the concept of Li$^+$ transference number.

Defined by Equation (4) where D indicates diffusion coefficients for ions in liquid electrolytes, Li$^+$ transference number (t_{Li+}) is the proportion of Li$^+$ diffusivity to the overall ionic diffusivity in liquid electrolytes. To be more straightforward, t_{Li+} can also be interpreted as the proportion of the Li$^+$ ionic conductivity to overall ionic conductivity.[156]

$$t_{Li+} = \frac{D_{Li+}}{D_{Li+}+D_-} \qquad (4)$$

The highest possible value for t_{Li+} is one. A high t_{Li+} indicates Li$^+$ takes up the majority of ion transported in the electrolyte. While a low t_{Li+} implies the anions in the electrolyte has a high mobility and accounts for a large portion of ion motion, which can lead to low energy efficiency and thermal runaway reaction as the transportation of anions lead to heat generation instead of electrochemical energy storage. t_{Li+} can be measured through electrochemical polarization and nuclear magnetic resonance spectroscopy (NMR), where the former one is widely adopted for a cell measurement while the latter one directly measures the diffusion coefficients of ions and reflects the physical properties.

For LiPF$_6$ liquid electrolyte, depending on the choices of solvent composition, t_{Li+} can vary in the range of 0.24 ~ 0.37 using polarization method.[157] Within a reasonable concentration and temperature range for liquid electrolytes, t_{Li+} does not fluctuate significantly so 0.38 is widely accepted as the t_{Li+} for LiPF$_6$ in EC/DEC electrolyte for all concentrations and temperatures.[158] Therefore, even though the overall ionic conductivity of LiPF$_6$ electrolyte can reach 10^{-3} S/cm, Li$^+$ conductivity is usually below 5×10^{-4} S/cm because of the high diffusivity and mobility of PF$_6^-$ anions. This low t_{Li+} of LiPF$_6$ liquid electrolyte causes a large amount of

anions accumulate on the surface of the electrode, building up a concentration gradient that creates overpotential for charging and discharging and further limits the power and energy density of the cell. In terms of this nontrivial issue of liquid electrolytes, it is shown that even a modest improvement in t_{Li+}, e.g. to ~0.7, would be greatly beneficial as it particularly allows a higher attainable state of charge (SOC) at higher rates.[159] In other words, a better fast-charging property will be empowered by a higher Li_+ transference number. As a result, numerous methods have been applied by researchers to adjust electrolyte properties upon the improvement of Li^+ transference number.

Starting from liquid electrolytes themselves, even though in a common range of electrolyte salt concentrations t_{Li+} does not vary significantly, researchers have discovered peculiar phenomena under extreme conditions. Suo *et al.* used an ultrahigh concentration of LiTFSI (salt to solvent weight ratio over 2.0) and reached an unexpected t_{Li+} of 0.73 due to the reduced solvation and a resulting higher mobility of Li^+. It remarkably suppresses Li dendrite growth and shape change for Li metal anode.[160] Similarly, the same leading researcher established a water-in-salt electrolyte with the concentration over 20 M for Li aqueous batteries and claimed the same mechanism.[161]

Gel electrolytes are a good transition stage for next-generation liquid electrolytes. They can be a mixture of liquid electrolyte and particle additives, or polymer matrix with ionic liquid. They could serve nearly as liquid electrolyte, or as a free-standing gel without extra use of a separator. Lu *et al.* tethered ionic liquid to silica nanoparticles covalently and then mixed it with LiTFSI salt to form a hybrid electrolyte. As a result of fixed anions on silica nanoparticles and the higher concentration of mobile ions in the hybrid, the obtained electrolyte exhibits a higher t_{Li+} ~0.54 with an uncompromised ionic conductivity.[162] The same research group improved the

transference number to ~0.96 by eliminating any extra Li salts. Silica nanoparticles are attached

with Li salts and dispersed in conductive fluid tetraglyme. They spontaneously form a charged,

nanoporous network of particles at moderate nanoparticle loadings. However, low ionic

conductivity ($< 10^{-4}$ S/cm) is an obvious drawback of this electrolyte system.[163] Tominaga *et al.*

discovered that direct and simple addition of titania nanoparticles to poly(ethylene carbonate)

based electrolytes can significantly improve both the ionic conductivity and the transference

number. The effect comes from the active interface between the polymer and titania nanoparticle

surface that has high acidity.[164]

Like mentioned, polymer matrix that forms free-standing gel electrolyte membrane is

another popular option since it also saves the use of extra separators. This method requires a

polymer that is able to construct a network structure in selected solvents allowing the formation

of free-standing membrane. Safa et al. developed a cationic-polymer based gel electrolyte, with

the addition of LiTFSI in ionic liquid. Due to the attraction of the polymer backbone to the

anions in the electrolyte, the Li^+ transference number has been improved from 0.3 to 0.41. Even

with the modest improvement, the rate capability of corresponding cells have been enhanced

significantly.[165] Li et al. mixed a polyethylene oxide with monomer solutions, and through

ultraviolet (UV) light achieved a crosslinked polymer network. Additional liquid electrolyte is

added. With the absorption of anions by the polymer network, the t_{Li+} is able to reach 0.76.[166]

Even though gel electrolytes can improve the transference number moderately, it is

usually not satisfying. Therefore, people have been trying to solve this problem in a more

aggressive way – solid-state electrolyte (SSE). Over any other types of electrolytes, solid-state

electrolytes in general have a huge advantage – a close-to-unity transference number. Besides,

SSEs are considered as a safe alternative as they suffer less problems in over-heating, leakage

and flammability.[166] SSE usually includes inorganic materials and polymer electrolytes. In inorganic SSE, lithium ions lie in the crystalline structure of the inorganic compounds, where Li^+ can ionize and shuttle within the structure whereas the according anions from the inorganic backbone does not have mobility due to its bulk structures. This type of SSE typically has higher ionic conductivity compared to the polymeric type due to their well-defined structure and Li^+ transportation pathways.[167] The first real SSE for lithium ions were developed by Dudney *et al*. This material is well known as LiPON (lithium phosphorous oxynitride). This pioneer of SSE, however, has a low ionic conductivity around 10^{-6} S/cm.[168] Inspired by this structure, various materials metal oxides are synthesized including lithium superionic conductor (LISICON) $Li_{14}Zn(GeO_4)_4$[169,170] and later on garnet type SSEs. Garnet type SSE $Li_7La_3Zr_2O_{12}$ (LLZO) was first reported by Murugan *et al*. LLZO can reach a high total conductivity of 7.74×10^{-4} S/cm at room temperature with a thin pellet. LLZO also delivers excellent thermalstability up to 900 ºC against lithium metal and non-flammability.[171] In order to improve its flexibility and fabricate the powder into free-standing electrolyte membrane, Fu *et al*. combined the LLZO with PEO-based polymer matrix to form a flexible membrane with nanofiber network. The obtained electrolyte membrane reached an ionic conductivity of 2.5×10^{-4} S/cm and a considerable lithium stripping/plating performance. The membrane also has stable thermal property and important non-flammability.[172] Despite their high ionic conductivity and non-flammability, the big challenge inorganic SSEs are facing comes from the high interfacial resistance caused by the poor contact between the solid-solid interface. To address this problem, Han et al. used atomic layer deposition (ALD) to construct a conformal Al_2O_3 layer on garnet type $Li_7La_{2.75}Ca_{0.25}Zr_{1.75}Nb_{0.25}O_{12}$ (LLCZN). Al_2O_3 can significantly help the molten Li conformally coat on the surface of LLCZN with no interfacial void space. The obtained membrane shows a

drastically reduced interfacial resistance and thus a remarkable lithium stripping and plating performance.[173]

Polymeric SSEs are another popular option. They can generally be categorized into two strategies, which are PEO-based composite electrolytes (the according batteries are given a special name of "lithium polymer battery") and single-ion polymer electrolytes. PEO-based electrolytes involve less innovation in chemical structures. They take advantage of the fact that inorganic lithium salts are more conductive in amorphous phases than crystalline phases. When composited with PEO-based polymers, those solid lithium salts ($LiClO_4$, $LiCF_3SO_2$, etc.) can dissociate and "dissolve" in the polymer matrix.[174,175] Polymer composite electrolytes are partially applied in commercial products such as smart phones and devices due to their high conductivity. However, despite their advantages, they usually cannot solve the problem of low Li^+ transference number because the dissolution and dissociation of small molecular weight lithium salts.[176] On the other hand, single-ion polymer electrolytes (solid polymer electrolytes, SPEs) address the problems in the opposite way. Resembling lithium salts, SPEs are composed of negatively-charged anions and lithium ions. Nevertheless, instead of small mobile anions, SPEs have anions covalently connected onto the polymer backbones, which immobilize the anions from transportation due to the polymeric nature. As a result, Li^+ are the only mobile ions in the electrolyte system, resulting in a single-ion conducting feature and a close-to-unity transference number. Due to the high dissociation of Li^+ from $TFSI^-$ groups from the delocalization, TFSI anions are often used as the anionic branches on polymer backbones. For instance, Bouchet et al. synthesized an efficient single-ion SPE with a triblock structure that is later widely adopted as a symbolic design. This BAB-type polymer contains a middle chain of PEO and end chains of P(STFSILi), where the PEO provides the lithium ion conducting ability,

and P(STFSI) provides the mechanical strength and the main ion pairs. By varying the ratio between the polymer structures, the conductivity is able to reach 10^{-5} S/cm at 60 °C with a Li^+ transference number of 0.85.[155] Likewise, SPEs usually allows single-ion conducting property and reaches high Li^+ transference number achieved by its nature. However, the low conductivity coming from its low lithium ion concentration largely limits its practical applications.

After all, the development of electrolyte materials for next-generation LIBs and LMBs never stop. Researchers continue the pursuit of ideal electrolytes that fulfill all the expectations for commercialization, most importantly including high ionic conductivity, fast Li^+ kinetics and transference number, and good thermalstability or non-flammability.

Chapter 2: Dissertation Objective

2.1 Design Criteria and Needs for Lithium-Ion Battery (LIB) Materials

As mentioned above, next-generation LIBs are reaching for high energy, high power, safety and low cost to cater for a rocketing demand for electrochemical energy storage systems.

When it comes to each individual component, there are different requirements and expectations. Cathode materials should have high specific capacity and high energy density as current cathode materials most exhibit very limited capacity. At the same time, the elimination of some metal elements that cause severe cost, pollution, recycling and humanity problems mainly including cobalt is expected in order to endorse LIBs with a higher acceptance worldwide. Anode materials should have higher specific capacity and energy density as well with a cycle life close to the classic anode material graphite. For applications of products, rate capability for charging process is usually more important compared to discharging. The rate performance of anode materials are usually the limiting step for charging rate, as lithium ions transport into anode materials during charging. In that case, the rate capability improvement for anode materials becomes critical. In the meantime, the improvement should not compromise the low cost of anode materials, otherwise it can harshly restrict the applications. As for the electrolyte materials, a fast kinetics for Li^+ transportation showing as a high Li^+ transference number (t_{Li+}) is vital for the development of high energy and power density batteries. At the same time, ionic conductivity should still maintain similarly high to conventional liquid electrolytes. Other advantages such as thermalstability and non-flammability are a highly preferred plus.

Beside the core components, other parts for cells and battery packs can also play an important role during the manufacturing and the packing process, such as current conductors, house materials, battery management systems (BMS), cooling components, sealing components, and etc. However, we will not discuss them here as they are outside the perspective of this dissertation.

2.2 Dissertation Objective and Research Scope

The general objective of this dissertation is to stretch the capacity and energy density of current LIB materials and achieve the goals for next-generation LIBs. To address some prominent challenges, we choose to develop silicon anode materials and LMB electrolyte materials as their applications can significantly boost the energy density of current batteries.

Even though silicon nanoparticles are favored due to their promising performance for the volume expansion suppression and cycling stability improvement, the incredibly high cost for materials production keeps them far away from being commercialized. We aim to produce nanoscaled silicon particles with a commercially accessible method, high-energy ball-milling, combining with direct polymer coatings that effectively buffer the volume expansion of silicon particles during lithiation process. This simple procedure and raw materials used enable low cost while still significantly improving the cycling stability of silicon materials. When further coated with an electronic conductive polymer, this anode material is compatible with commercial graphite. The according composite Si/C anode material is expected to have a comparable cycling performance to graphite while delivering a greatly improved capacity.

In order to achieve the application of LMBs, high ionic conductivity and high Li^+ transference number are both absolutely necessary. Current technologies either exhibit high conductivity but slow Li^+ kinetics or the opposite. We aim to mimic the efficient biological ion transportation on cell membranes and develop an electrolyte membrane that well incorporates both high conductivity and Li^+ transportation through the association and electrostatic interaction with liquid electrolyte. The according electrolyte membrane is expected to immobilize the anions in the liquid electrolyte and as a result improve the energy efficiency and cycling performance of LMBs with a high Li^+ transference number.

Chapter 3: Covalently-Bonded Si-Polymer Nanocomposites Enabled by Mechanochemical Synthesis as Durable Anode Materials

3.1 Introduction

The fast-growing demand for electric vehicles, portable devices and grid-scale energy storage urges the development of next-generation lithium-ion batteries (LIBs) with higher power and energy density. Considerable research efforts hence have been devoted to the engineering of silicon, a promising anode material with moderate operating potential (0.1~0.4 V) and high specific capacity (3578 mAh g^{-1} for Li$_{3.75}$Si) in comparison with the current commercial graphite (0.05 V and 372 mAh g^{-1}).[109,177,178] Bulk silicon resources are abundant and cost-effective, yet its severe pulverization and repeated formation of solid-electrolyte interphase (SEI) caused by the huge volume expansion (300%) result in irreversible capacity loss and poor cycling stability.[179,180] Therefore, its practical application has been greatly restricted.

Aiming at improving the structural integrity, a variety of synthetic strategies have been developed to fabricate silicon nanostructures.[181–185] Significantly, special attention has been put into the protection of silicon with functional coating layers, involving different methods such as CVD[186,187], heat treatment,[188–190] sol-gel[191,192] and so on[193,194]. However, the complexity, inefficiency and high-cost generally impede their large-scale production and adaption. High-energy ball- milling (HEBM) has been reported as a low-cost, high-yield and scalable method for the efficient production of silicon nanomaterials, which is feasible for industrial manufacture.[195]

Different from mixing ball-milling, energy can be re-dispersed and transported by HEBM with strong friction and collision.

Figure 3.1 shows the original research work on the utilization of HEBM for the production of Si nanoparticles.[195] Compared to the pristine Si powders in microscale, Si nanoparticles after HEBM process presents a well-distributed nanoscaled size (Figure 3.1a, b). As Figure 3.1c shows, during the HEBM process, the grain boundaries of Si particles will become amorphous due to the strong shear force. The amorphous layers of Si allow a faster transportation of Li^+, and significantly improve the lithiation kinetics, which will enhance the cycling stability as well as the rate performance. Therefore, even compared to commercial crystalline Si nanoparticles, the ball-milled Si could deliver a superior electrochemical performance. As a result, ball-milled Si delivers a much longer cycle life in comparison to commercial Si nanoparticles in Figure 3.1d.
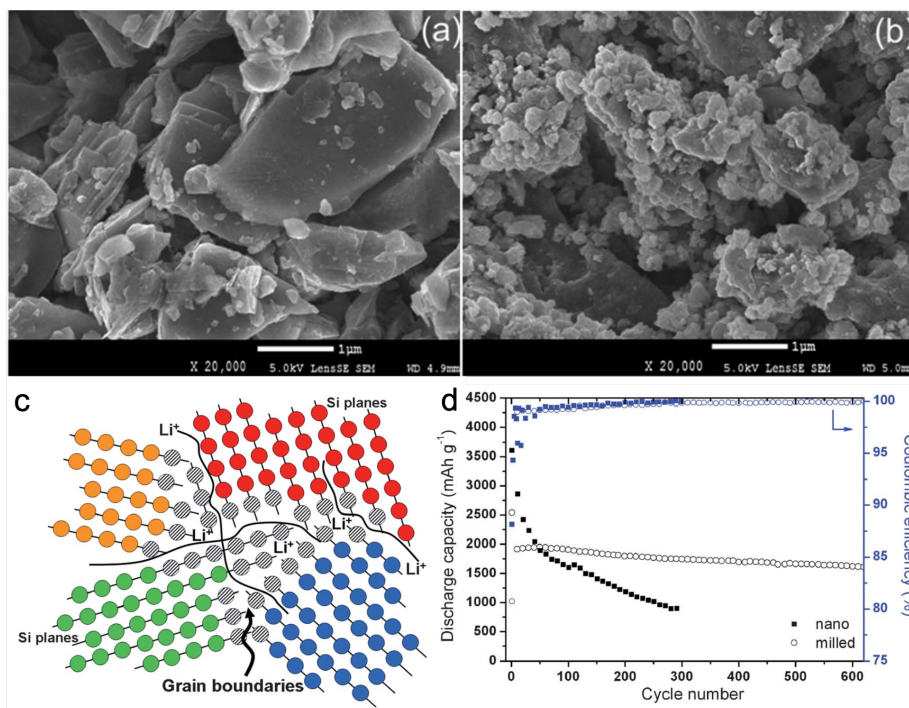
Figure 3.1 SEM images of (a) as-received 1-5 μm Si powder and (b) milled 1-5 μm Si powder. (c) Scheme of nanocrystalline structure of milled Si powder showing grain boundaries where faster Li^+ diffusion occur.[195]

More interestingly, the precedents of organic reactions and synthesis of metal-organic frameworks demonstrate the feasibility of building chemical bonds through HEBM.[196,197] However, for the preparation of Si-based anode materials, HEBM has only been engaged in size breaking- down, which makes post-processing necessary to construct robust chemical connection with protective layers.[198–200] The concept of reactive high-energy ball-milling (RBM) has barely been applied for the production of silicon nanocomposites with chemically bonded coating layers.

Herein, we report polymer-coated silicon nanocomposites with *in situ* generation of covalent bonds between Si nanoparticles and poly(vinyl alcohol) (PVA) by a solvent-free, one-pot and no-post-process RBM method. PVA acts as the resilient component in the composites because of its high tensile strength and flexibility. The flexible covalently-bonded coating buffers the volume expansion of the silicon during lithiation process, which effectively prevents the particles from pulverization and maintains the integrity of electrode. The size of Si nanoparticles can be adjusted by regulating the content of PVA, among which silicon nanoparticles coated by 5% PVA deliver the optimal electrochemical properties. A reversible specific capacity of 1526 mAh g^{-1} is obtained at 200 mA g^{-1} after 100 cycles with loading of 1 mg cm^{-2}. A high initial Coulombic efficiency (ICE) over 86% and an average of 99.2% have been achieved.

3.2 Experimental Section

3.2.1 Synthesis for PVA-Coated Silicon Composite

Silicon (99%, ~325 mesh) and poly(vinyl alcohol) (M_W 89,000-98,000, 99% hydrolyzed) were purchased from Sigma-Aldrich without further purification. Si and different amount of PVA (0, 2 wt%, 5 wt%, 10 wt%) were mixed in the jars with the ball-to-powder ratio of ~12, sealed in argon atmosphere, and milled by the high-energy ball-miller (Retsch, High Energy Ball Mill Emax) at 1000 rpm. After 10 h, all powder was collected without further treatment.

3.2.2 Structural Characterizations

Crystalline structures of the Si-PVA powder were determined by the Rigaku powder X-ray diffractometer (XRD) using Kα radiation (λ = 1.54 Å). Surface morphology and particle sizes were investigated by scanning electron microscopy (Nova 230 Nano SEM), transmission electron microscopy (FEI T12 Quick CryoEM and CryoET TEM) and High-resolution transmission electron microscopy (FEI Titan S/TEM). Raman spectra was conducted on a Renishaw 2000 System with a He/Ne laser at a wavelength of 633 nm. Infrared spectra experiments were carried out by a transmission mode on a Jasco 420 Fourier transform infrared (FTIR) spectrophotometer. Thermogravimetric analysis (TGA) was performed in argon atmosphere by a ramping rate of 10 °C min^{-1}. Gas sorption measurements were conducted using a Micromeritics ASAP 2020 system at 77 K. Prior to gas adsorption/desorption measurement, all power was degassed at 120 °C for 12 h. For X-ray photoelectron spectroscopy (XPS) studies, AXIS Ultra DLD was used for analysis. All the spectra were fitted to Gaussian–Lorentzian functions and a linear-type background using CasaXPS software. The binding energy values were all calibrated using C 1s peak at 284.5 eV.

3.2.3 Electrochemical Characterizations

The electrochemical performance was evaluated using 2032-type coin cells with the Li foil as the counter/reference electrode. The working electrodes were comprised of active materials (Si-PVA composite), acetylene black, and poly(acrylic acid) (PAA) binder with the weight ratio 7:2:1 and were fabricated using a typical slurry method. The mass loading of the active material was ~1 mg cm^{-2} for each electrode. The electrolyte was 1 M LiPF$_6$ in a mixture of ethylene carbonate (EC)/diethyl carbonate (DEC) with a volume ratio of 1:1 (LP40, BASF), and 5 vol% fluoroethylene carbonate (FEC, Sigma-Aldrich) was used as an additive. The assembled cells were galvanostatically cycled between 0.05 and 2 V vs Li$^+$/Li at different current densities using a LAND battery testing system (China). The specific capacities were calculated based on the total mass of the Si-PVA powder. Cyclic voltammetry (CV) experiments for the first cycles were performed using the electrochemical station Solartron 1860/1287 with a scan rate of 0.1 mV s^{-1} from open-circuit voltage (OCV, ~3 V vs Li/Li$^+$) to 0 and back to 2 V. Electrochemical impedance spectroscopy (EIS) data were recorded ranging from 100 kHz to 10 mHz with a voltage amplitude of 10 mV.

3.3 Results and Discussions

The synthetic strategy is schematically illustrated in **Figure 3.2**. The bulk silicon powder and PVA without any solvent are sealed in argon atmosphere in a ball-milling jar. Bearing the impact from the steel balls, the micron-sized silicon is ground into nanoparticles. Simultaneously, the mechanical energy also triggers the chemical reaction between freshly exposed surface of silicon nanoparticles and reactive hydroxyl groups of PVA. Due to the low dissociation energy of O-H bonds[201], the hydroxyl groups on PVA cleave and form Si-O-C bonds, generating nanocomposites of PVA coated silicon nanoparticles with robust chemical bonding.
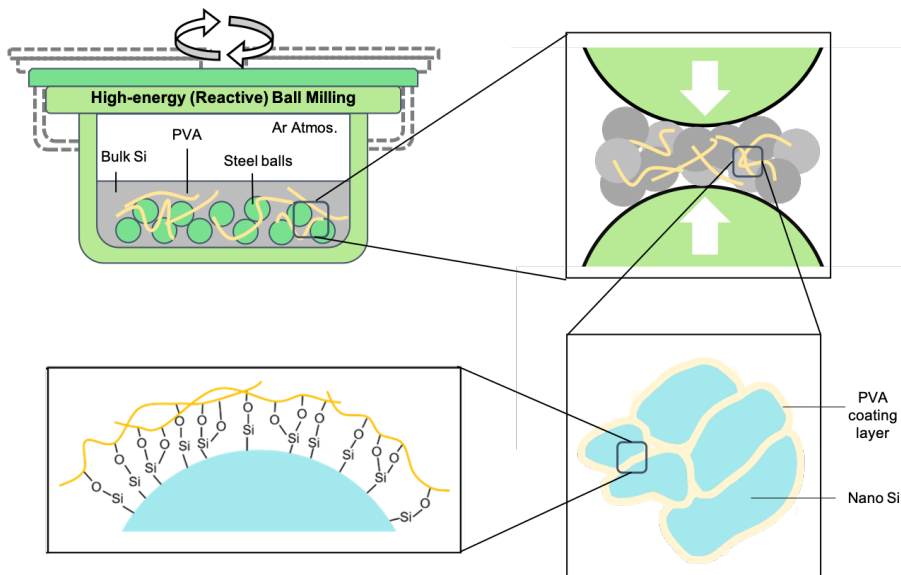
Figure 3.2 Schematic diagram of the reactive ball-milling (RBM) process starting with bulk silicon and the product of poly(vinyl alcohol) (PVA) coated silicon nanoparticles with the covalent bonds between PVA and the silicon on the surface.

The samples with different amount of PVA relative to silicon are denoted as RBM Si-2%PVA, RBM Si-5% PVA and RBM Si-5%PVA, respectively. Pure ball-milled Si without adding PVA is denoted as HEBM Si. The Raman spectrum of crystalline silicon generally contains one sharp peak at 520 cm^{-1}, which will redshift in a size-dependent manner.[202] Compared to raw silicon materials, the characteristic peak of ball-milled silicon-PVA nanocomposite in Raman spectrum shifts from 520 to 504 cm^{-1} (**Figure 3.3a**) with different content of PVA, indicating the formation of Si nanocrystals. The corresponding peak of HEBM Si, however, appears at a slightly higher wavenumber, suggesting a larger particle size than that of the PVA coated silicon.

X-ray diffraction (XRD) patterns presents accordant results (**Figure 3.3b**). Increasing the content of PVA in the composite significantly broadens the widths of diffraction peaks of (111),

(220) and (311) of Si-PVA composites, which directly confirms the reduced crystalline size in the presence of PVA. Due to the turbulent crushing during RBM, the crystalline silicon experiences a deformation into amorphous structure on the edge of the particles as suggested by the reduced peak intensity in the XRD patterns, which might benefit the kinetics of lithium ions transport.[45] N_2 sorption isotherms indicate a rising BET surface area with the addition of PVA due to the reduced particle size (**Figure 3.3c**). Starting from micron-size silicon with a BET surface area of only 5.1 m^2 g^{-1}, Si-PVA nanocomposites deliver much enlarged BET surface areas of 11.1, 17.4 and 19.2 m^2 g^{-1} for Si-2%PVA, Si-5%PVA and Si-10%PVA, respectively. The different volume of these samples (**Figure 3.3d**) with the same weight indicate a reduced tap density and thus a decreasing particle size. Based on the tap density of Pristine Si, the tap densities of ball-milled powders are calculated accordingly and presented in **Table 3.1**.
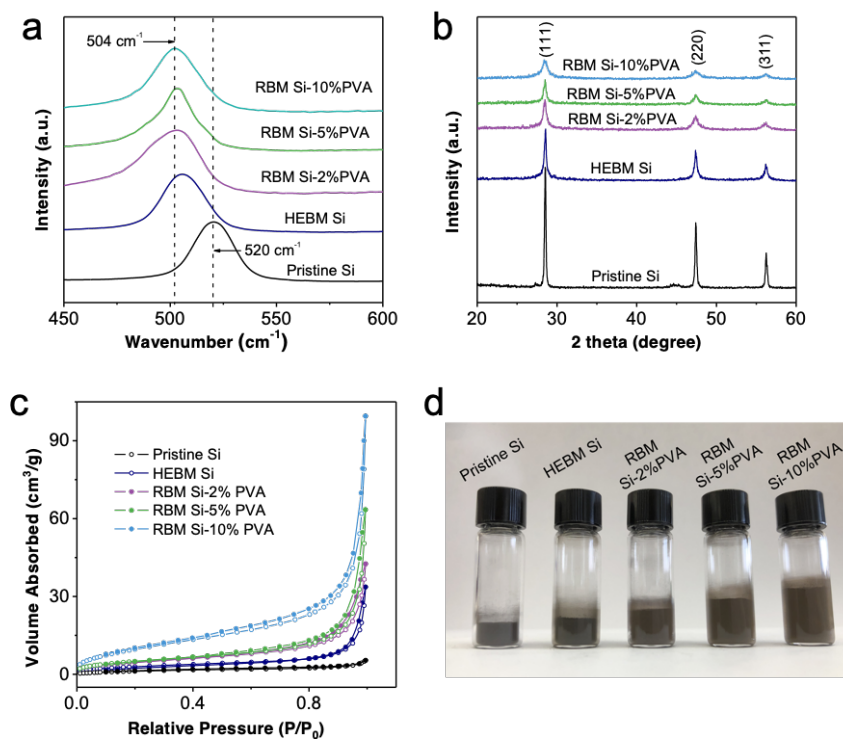
Figure 3.3 Characterizations of pristine bulk silicon, HEBM Si, and RBM Si-PVA nanocomposites. (a) Raman spectrum, (b) XRD pattern, (c) N_2 sorption isotherms of Si-PVA nanocomposites and (d) photographs comparing the tap density.

Table 3.1 Tap density of powders before and after HEBM.

	Pristine Si	HEBM Si	RBM Si-2%PVA	RBM Si-5%PVA	RBM Si-10%PVA
Tap density (g mL^{-1})	2.33	1.91	1.50	1.23	1.00

SEM characterizations were carried out to examine the morphology of samples after ball milling. Owing to the exposure of the high-energy surface of the particles during HEBM, the secondary aggregation of the nanoparticles is usually severe and inevitable. Without additional PVA, the finely crushed primary HEBM Si particles naturally aggregate into secondary particles up to 10 μm, which dispossesses the advantages of nanomaterials and renders a drastic structural transition during lithiation and delithiation. By forming covalent bonds between the PVA and Si particles, the active surface is chemically quenched, which effectively mitigates the formation of aggregates. The RBM Si-5%PVA primary particles are typically below 200 nm (**Figure 3.4a**), notably smaller than the HEBM Si (**Figure 3.4b**). Most of the secondary particles of RBM Si-5%PVA fall in the range of 0.5-1 μm. TEM images display more distinct differences. The RBM Si-5% PVA particles are around 200 nm and well-dispersed (**Figure 3.4c**). In contrast, the HEBM Si appears as an aggregation with size over 2 μm (**Figure 3.4d**). The sizes of RBM Si-2%PVA and RBM Si-10%PVA are consistent with the BET results as well (**Figure 3.4e,f**). The diffraction

spots corresponding to (111), (220) and (311) lattice planes of polycrystalline silicon can be found in the SAED pattern (**Figure 3.5a**). The (111) lattice of silicon with an interplanar spacing 0.32 nm can be determined in the HRTEM image (**Figure 3.5b**). More importantly, a layer of amorphous domain is observed around the Si nanocrystals, which may be assigned to the polymer coating and/or amorphous Si. The Si nanoparticles are effectively separated by the in situ formed polymer framework and the agglomeration is therefore remarkably suppressed during HEBM. Such unique structure might accommodate the volume change of Si, and also prevent the Si particles from aggregation upon repeated lithiation/delithiation.
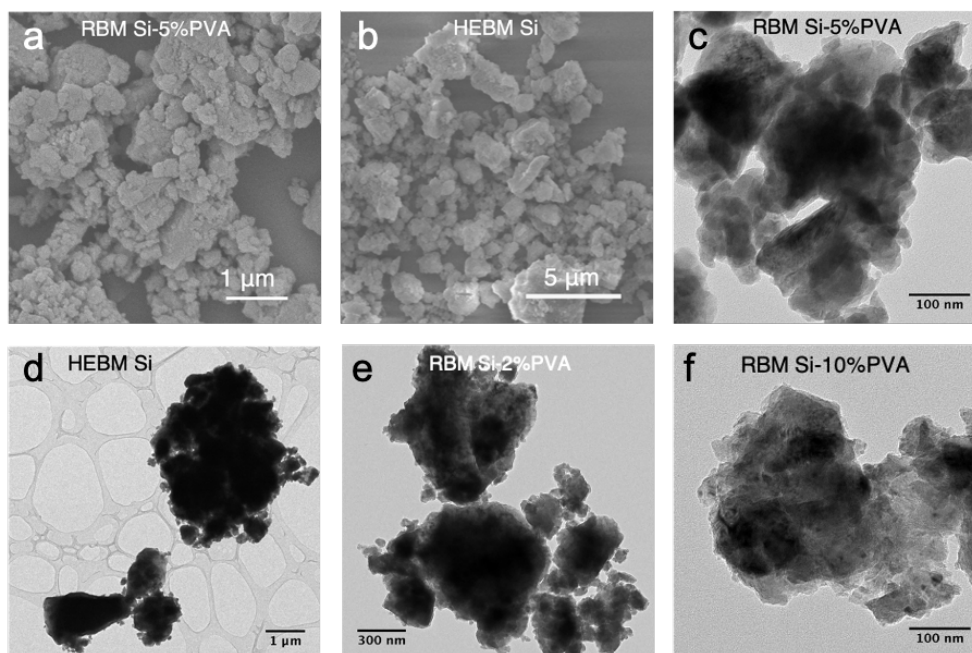
Figure 3.4 Morphology and sizes of HRBM Si powders. SEM images of (a) RBM Si-5% PVA and (b) HEBM Si and TEM images of (c) RBM Si-5%PVA, (d) HEBM Si, (e) RBM Si-2%PVA and (f) RBM Si-10%PVA.
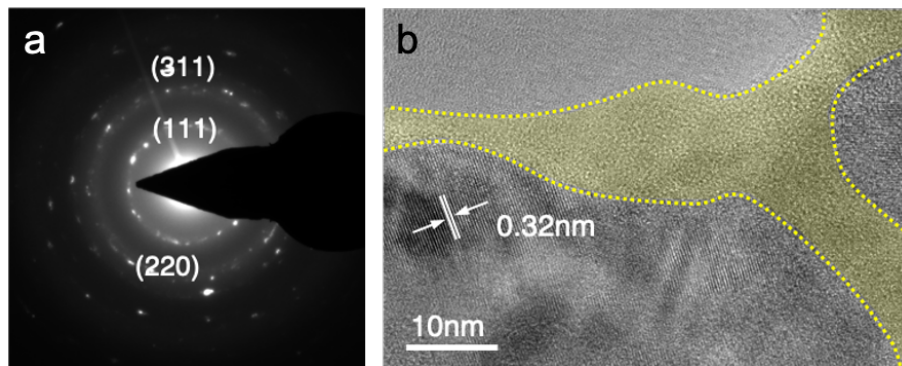
Figure 3.5 (a) SAED and (b) HR-TEM images of RBM Si-5%PVA.

The formation of covalent bonds between Si and PVA during the ball-milling process is further supported by the X-ray photoelectron spectroscopy (XPS) profiles. Typical peaks for Si in Si 2p spectrum located at 99.6, 100.3, 100.9 and 103.5 eV represent Si $2p_{3/2}$, Si $2p_{1/2}$, Si-O and SiO_2, respectively (**Figure 3.6a**).[203] All these peaks remain in the spectrum of RBM Si-5%PVA. In addition, a new peak at 102.5 eV corresponding to Si-O-C bonding appears,[204] probably due to the reaction between hydroxyl groups (-OH) from PVA and freshly exposed surface of silicon particles during RBM (**Figure 3.6b**). After the RBM process, the C-H/C-C peak (284.8 eV) from PVA polymer chain remains in C 1s spectrum, while the original C-OH peak at 286.3 eV is replaced by a new peak at 286.9 eV for Si-O-C (**Figure 3.6c, d**). Consistently, in O 1s spectrum, the Si-O-C peak (532.2 eV) in RBM Si-5%PVA completely replaces the C-OH peak (533.4 eV) in PVA (**Figure 3.6e-g**).[205] These observations imply that hydroxyl groups in PVA have fully reacted with silicon during RBM and a layer of Si-O-C coating layer has formed on the surface of silicon. The FTIR result provides direct evidences of the covalent bonds on the coated silicon particles surface (**Figure 3.7a**). The peak of Si-O-Si stretching around 1150-1200 cm^{-1} for HEBM Si [206] also appears in the spectrum of RBM Si-5%PVA, while the C-O peak in PVA for RBM Si-

5%PVA shows up at around 1100 cm^{-1}. More importantly, the characteristic peak of Si-O-C locates at around 1020 cm^{-1}. Additionally, the chemical linking between PVA and Si particles after RBM is confirmed by TGA. Both RBM Si-5%PVA and HEBM Si exhibit extraordinary thermal stability up to 1000 °C, compared to pure PVA with major weight loss occurring at around 250 °C (**Figure 3.7b**). Different from extensively reported physical coating/wrapping on the surface of Si nanoparticles, RBM is capable to achieve in situ generation of covalent bonds, inducing a robust shell to protect silicon particles. Furthermore, the complete removal of reactive groups in the raw materials might also improve the electrochemical stability.
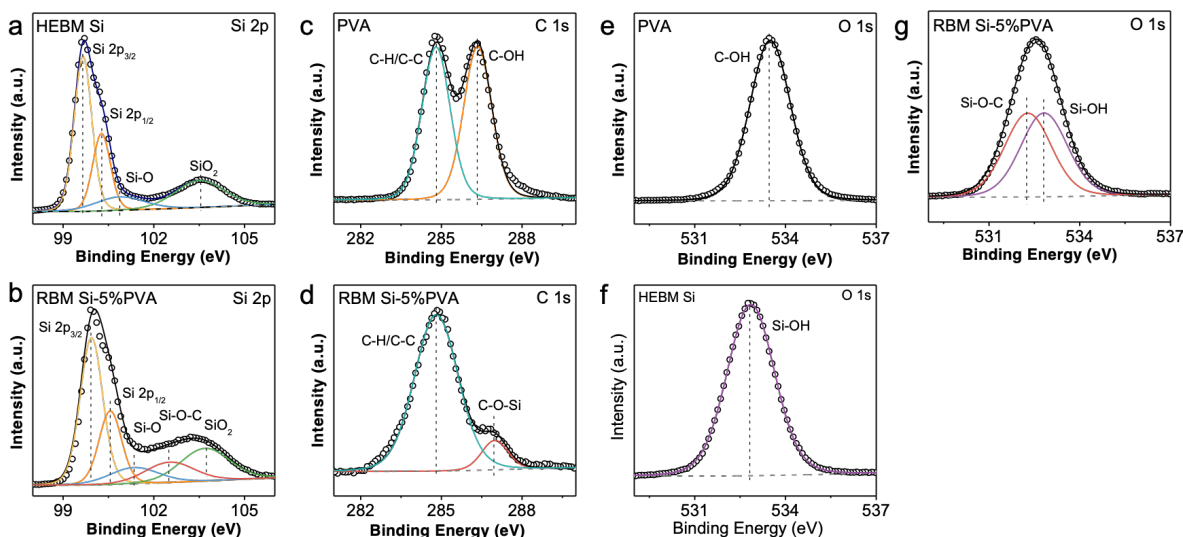
Figure 3.6 Characterizations of the chemical structure of the HEBM Si and RBM Si-5%PVA. Si 2p XPS spectra for (a) HEBM Si and (b) RBM Si-5% PVA. C 1s XPS spectra for (c) PVA and (d) RBM Si-5% PVA. O 1s XPS spectra for (e) PVA, (f) HEBM Si and (g) RBM Si-5%PVA.
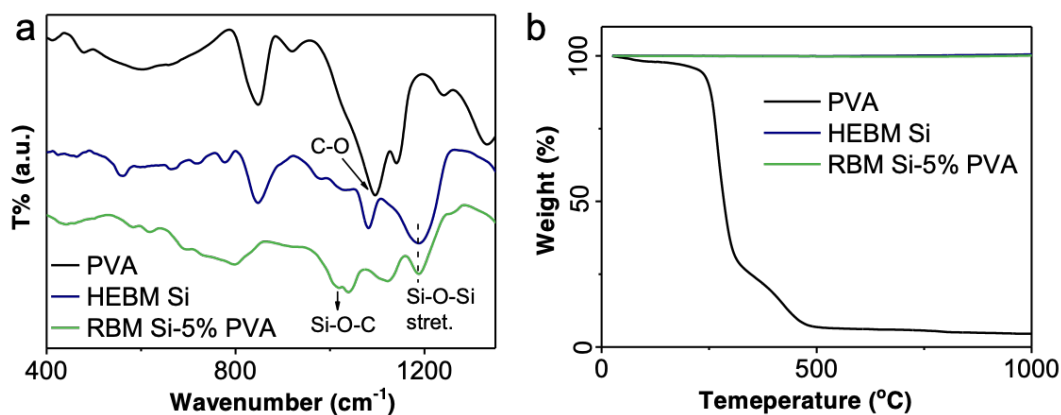
Figure 3.7 (a) FTIR and (b) TGA for PVA, HEBM Si and RBM Si-5% PVA.

The electrochemical lithiation/delithiation performances of the as-prepared silicon particles were investigated in half-cell configurations. **Figure 3.8** displays the CV feature of the RBM Si-5%PVA for the first four cycles. In the first cycle, the distinctive cathodic peak around 0.05 V reveals the initial formation of Li_xSi ($0 \leq x \leq 3.75$) alloy process. The two anodic peaks at 0.36 V and 0.53 V can be assigned to the phase transformation from high-Li-content to low-Li-content Li_xSi alloys and eventually to amorphous Si. The subsequent scans exhibit similar CV profiles, with another cathodic peak emerging at 0.18 V. The current increases steadily as the scans proceed, implying an activation process and formation of stable SEI on the electrode surface. Besides the well-established lithiation/delithiation peaks, no side reaction was detected, which is attributed to the elimination of reactive groups during RBM process.
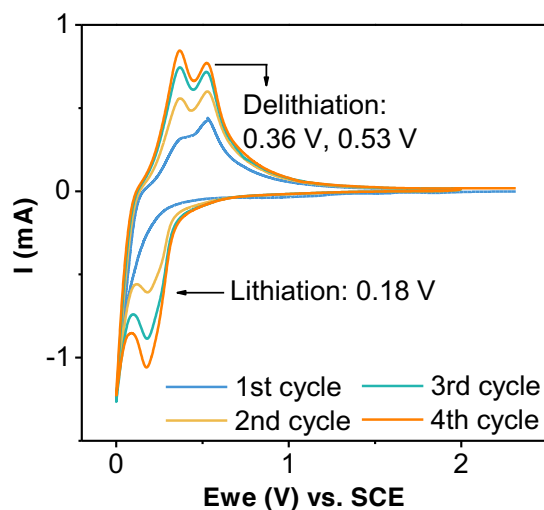
Figure 3.8 CV analysis for RBM Si-5%PVA sample.

Galvanostatic charging/discharging at 0.2 A g^{-1} for RBM Si-5%PVA discloses stable voltage profiles with well-defined charging/discharging plateaus. With the increasing content of PVA in the active materials, the specific capacity slightly decreases. Meanwhile, stability of the electrodes is notably improved, leading to higher capacity retention upon cycling. The initial capacity for bare HEBM Si is 3255 mAh g^{-1} with an ICE of only 83.0%, along with fast capacity fading (**Figure 3.9a**). The stability is slightly improved with 2% of PVA (**Figure 3.9b**). Nonetheless, the RBM Si-5%PVA electrode exhibits initial specific capacity of around 3000 mAh g^{-1} and an ICE of 86.1% with negligible capacity loss in the first three cycles (**Figure 3.9c**). The RBM Si-10%PVA shows a similar stability compared with RBM Si-5%PVA while the initial specific capacity drops to 2434 mAh g^{-1} due to the higher weight ratio of inactive PVA (**Figure 3.9d**). Through the PVA coating, the stability and the ICE of the electrodes are greatly improved with minimal sacrifice on the specific capacity.
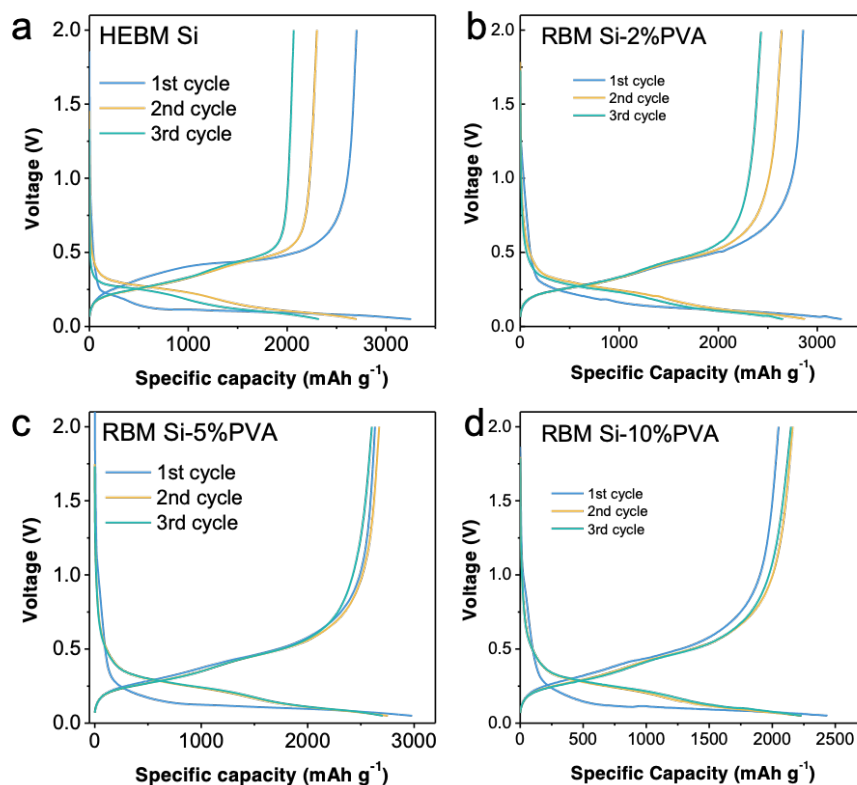
Figure 3.9 Galvanostatic charging/discharging profiles for (a) HEBM Si, (b) RBM Si-2%PVA, (c) RBM Si-5%PVA and (d) RBM Si-10%PVA. Current density: 200 mA g^{-1}.

Figure 3.10a compares the rate performance of RBM Si-5%PVA and HEBM Si electrodes. Ranging from 0.15 to 3.0 A g^{-1}, the capacity of electrode drops stepwise to 801 mAh g^{-1} and recovers to 2234 mAh g^{-1} once the current returns to 0.15 A g^{-1}. **Figure 3.10b** shows the galvanostatic cycling stability of the ball-milled silicon materials with a loading of 1 mg cm^{-2} and a current density of 0.2 A g^{-1}. In contrast to the drastic capacity fading of HEBM Si, Si-PVA nanocomposites synthesized through RBM present enhanced stability and higher capacity retention. It is noteworthy that the RBM Si-5%PVA offers the best improvement. Besides a high

ICE of 86.1% as mentioned earlier, the Coulombic efficiency (CE) rapidly reaches over 97% from the second cycle onwards (**Table 3.2**). After being activated in the first 10 cycles, the electrode steadily becomes stabilized and remains stable for later cycles, with 1526 mAh g^{-1} reversible specific capacity retained after 100 cycles and an average CE of 99.2%. A substantial capacity loss to 1395 mAh g^{-1} occurs in the first 5 cycles for RBM Si-10%PVA electrode, ending up with a reversible capacity of 798 mAh g^{-1} after 100 cycles. We speculate that the severe polymer solvation and swelling from the higher content of PVA leads to a more significant structural change, thus causing the quick capacity fade in the first several cycles. In addition, HEBM Si is simply stirred and mixed with 5% of PVA to demonstrate the vital role of RBM. Owing to the side reactions with the electrolytes induced by the reactive groups on PVA, the ICE is hardly over 70 %. Without the robust chemical interaction to preserve the integrity, the electrode quickly fails. Further increasing the current density to 3.0 A g^{-1}, the RBM Si-5%PVA electrode delivers a reversible specific capacity 750 mAh g^{-1} after 150 cycles (**Figure 3.10c**).
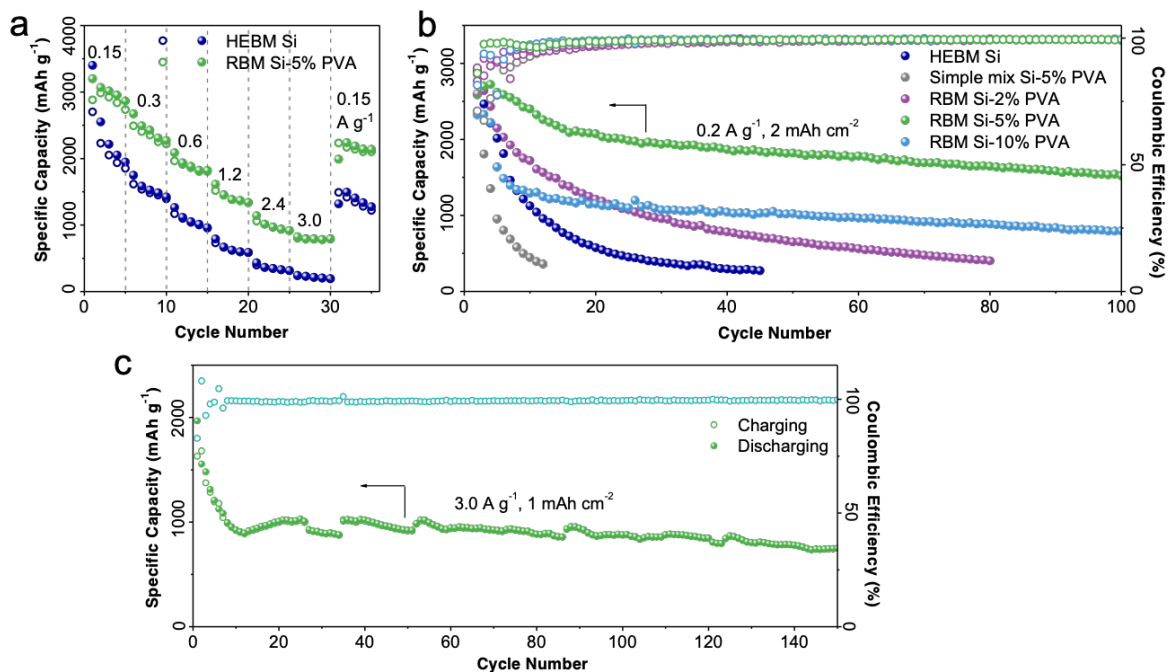
Figure 3.10 Electrochemical characterizations of the RBM Si-PVA anodes. (a) Rate performance of HEBM Si and RBM Si-5%PVA electrodes with the loading of 1 mg cm^{-2}. (b) Long-term cycling performances of ball-milled silicon materials at 0.2 A g^{-1} with the mass loading of 1 mg cm^{-2}. (c) Fast charging/discharging (3.0 A g^{-1}) performance of RBM Si-5%PVA electrode with the mass loading of 1 mg cm^{-2}.

Table 3.2. Coulombic efficiency of the first 5 cycles for cell cycling according to Figure 3.10b.

Cycle Number	HEBM Si	Simple mix Si-5%PVA	RBM Si-2%PVA	RBM Si-5%PVA	RBM Si-10%PVA
1	83.03%	71.24%	88.22%	86.12%	81.43%
2	85.14%	67.46%	91.92%	97.56%	93.76%
3	88.99%	76.1%	91.87%	97.98%	93.22%
4	90.36%	77.46%	91.12%	97.87%	77.62%
5	89.58%	87.32%	94.46%	98.33%	91.59%

EIS tests were conducted simultaneously at different cycle numbers. The diameters of the semicircles in the plots were evaluated with the measurement and indicate the charge transfer resistance (R_{ct}) of the cell.[207,208] For fresh electrodes, the resistance first gradually decreases from 316 Ω (HEBM Si) to 240 Ω (RBM Si-5%PVA), due to the improved ion transportation kinetics benefited from the reduced particle sizes. However, when the PVA content has reached 10%, the charge transfer resistance increases back to 340 Ω, indicating the role of non-conductive additive PVA has overruled the slight size decrease compared to RBM Si-5%PVA (**Figure 3.11a**). This result provides another explanation for the superior cell performance with RBM Si-5%PVA. After the first cycle of galvanostatic charging/discharging for the RBM Si-5%PVA electrode, the impedance reduces dramatically to 56 Ω, suggesting the formation of ionic conductive SEI layer. The impedance of the cell continues to decrease until it reaches 21 Ω after the 50th cycle, and

remains stable at 21 Ω to the 100th cycle (**Figure 3.11b**). At the beginning of cell cycling, the formation of SEI layers and improved interfacial contact that can be ascribed to the activation and wetting process significantly enhanced the charge transfer capability. Eventually, the R_{ct} maintains consistent, revealing a stabilized SEI layer and mitigated Si pulverization. To strike a balance between the capacity and stability, RBM Si-5%PVA is preferentially selected for the additional cycling tests. Through the covalent linking between silicon and PVA protective layer by RBM, the electrochemical performances in terms of CE and cycling stability of the electrode are greatly improved.
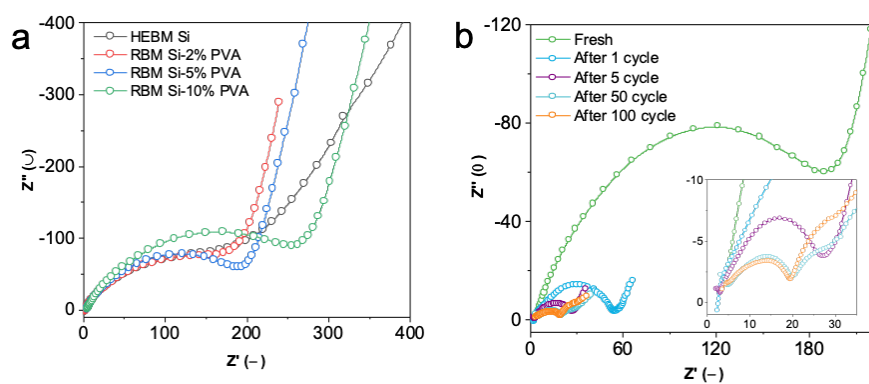
Figure 3.11 EIS profiles of (a) fresh electrodes with different Si powders and (b) RBM Si-5%PVA electrode before and after cycling. Inset: magnified EIS profiles of the high frequency region.

Figure 3.12a illustrates the working mechanism of the resilient PVA coating that promotes the cycling stability of the silicon electrodes. On the surface of silicon, the flexible polymer PVA with a linear chain structure can stretch and contract along with the volume expansion and

shrinkage of silicon particles during lithiation and delithiation. Unlike solely physical contact, the stable chemical bonding between the PVA chains and particles surface prevents phase separation during the volume variation of silicon. The PVA coating acts as a resilient buffer layer to accommodate the volume expansion and thus prevents the particles from pulverization. As a result, the integrity and thus cycling stability of the electrode would be notably improved. SEM images of cycled electrodes provide a visible demonstration of the improved mechanical stability of Si-PVA nanocomposites. After only one cycle of lithiation/delithiation, the surface of HEBM Si electrode becomes rough with deep cracks with a typical width of 10.5 μm (**Figure 3.12b**). The electrode film continuously breaks down upon cycling (**Figure 3.12c**), leading to obvious disintegration after 10 cycles with almost 20 μm width cracks (**Figure 3.12d**). On the other hand, only minor crevices typically 2.0 μm in width on the surface of electrode is observed for RBM Si-5%PVA (**Figure 3.12e**), and the electrode remains generally intact from the 5th to the 10th cycle (**Figure 3.12f, g**). The RBM Si-10%PVA electrode shows a similar result (**Figure 3.12h-j**). With only 5% PVA coating, we successfully mitigate the pulverization and thus enhanced the cycling stability of the silicon anodes.
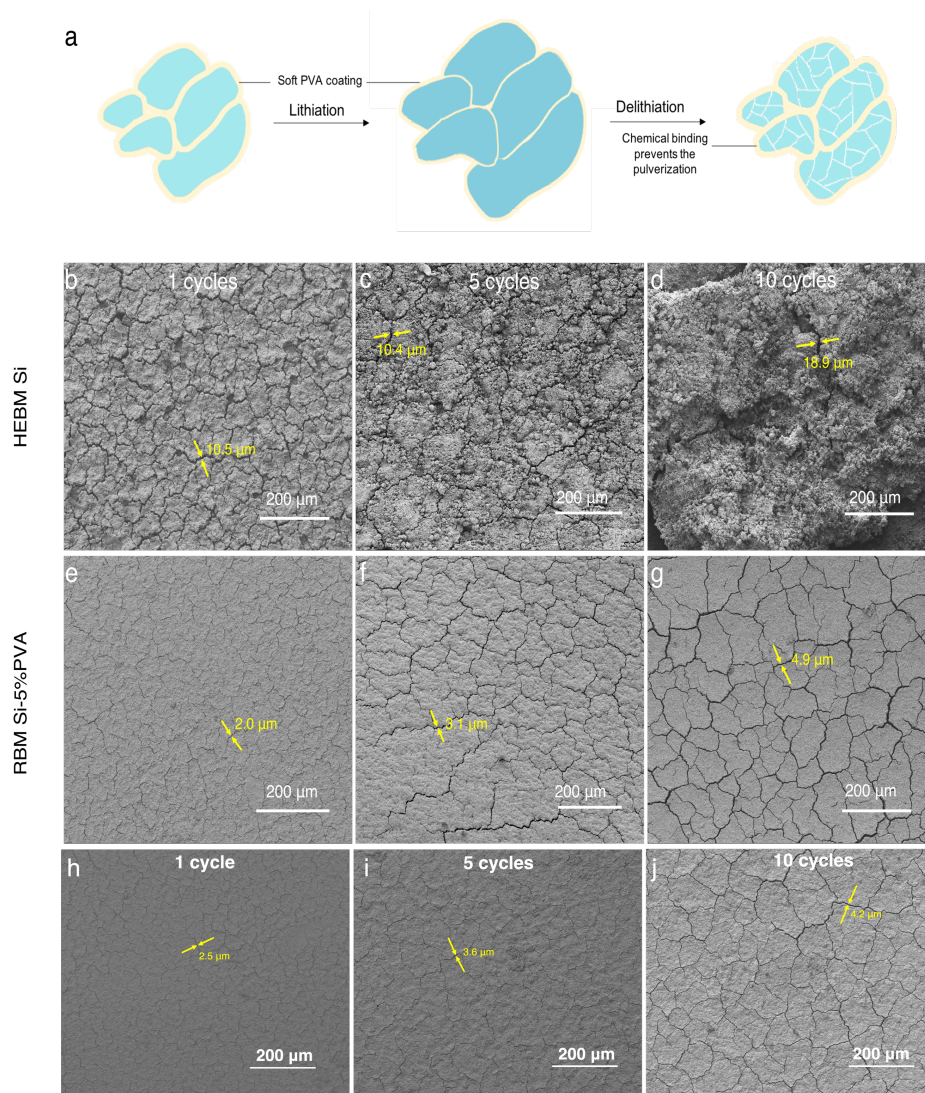
Figure 3.12 (a) Schematic diagram of the lithiation/delithiaion process of the ball-milled silicon materials. (b-g) Morphology of cycled silicon electrodes. SEM images of (b, c, d) HEBM Si electrodes, (e, f, g) RBM Si-5%PVA and (h, i, j) RBM Si-10%PVA after (b, e, h) one, (c, f, i) five and (d, g, j) ten cycles, respectively.

As suggested previously, despite the high specific capacity, the cycling stability silicon alone delivers might not be satisfying for industrial applications. Given that, Si/graphite

composite material is popular as a substitution and transitional option from graphite to Si anode materials. Consequently, we fabricated the obtained RBM Si-5%PVA particles with commercial graphite to produce Si/graphite composite anode materials. As shown in **Figure 3.13a**, the composite material delivers a high specific capacity of 1300 mAh g^{-1} at the beginning activation process of the cycle when the current density is 0.2 A g^{-1}. Following the higher current density of 0.5 A g^{-1}, the composite Si/graphite material maintains a highly reversible specific capacity of ~1000 mAh g^{-1}, which gives an impressive capacity retention of 87.5% after 100 cycles. Compared to graphite (372 mAh g^{-1}, dashed line), the according Si/graphite provides a greatly improved capacity, as well as a decently comparable cycling stability. **Figure 3.13b** shows the rate performance for the composite material. When the current density was raised from 0.1 A g^{-1} to 1.6 A g^{-1}, the specific capacity still reaches ~700 mAh g^{-1}, which is much higher than graphite, especially considering the poor rate capability of graphite materials.[209,210] When the current was decreased back to 0.2 A g^{-1} again, the capacity was able to recover to ~1200 mAh g^{-1} and remain stable to 100 cycles.
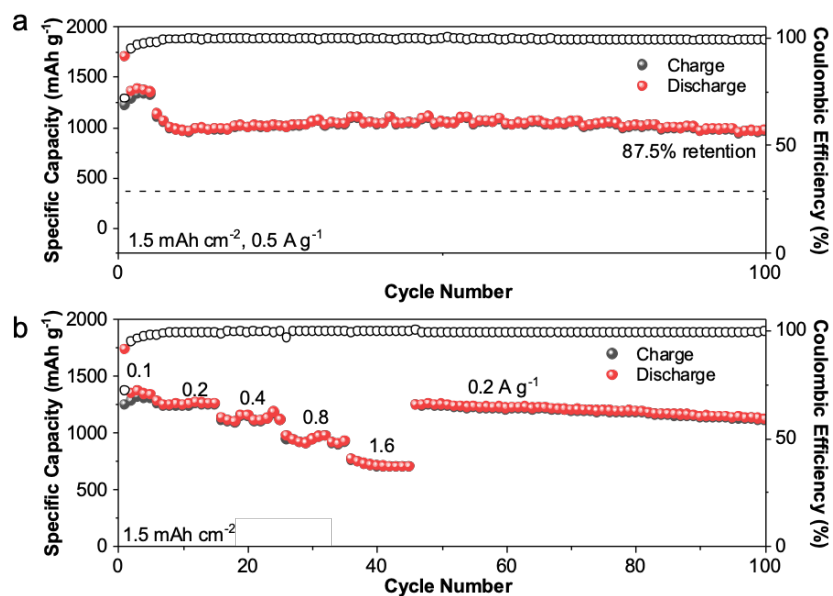
Figure 3.13 (a) Cycling performance of the Si/graphite (wt. 1:1) composite anode material. (b) Rate performance for the Si/graphite (wt. 1:1) composite anode material. Mass loading of the anode materials: 1.2 mg cm^{-2}.

In order to rationalize the practical applicability and commercial feasibility, high areal capacity was developed with the composite anode material. Si/graphite with a higher content of graphite (8 wt.% Si and 92 wt.% graphite) was fabricated for the cycling performance test. The specific capacity of the resulted Si/graphite composite is around 510 mAh g^{-1}, with an areal capacity of 3.2 mAh cm^{-2} for the corresponding anode. Even under a low current density of 50 mAh g^{-1}, the material still renders a high ICE of 89% and a capacity retention of 85.5% after 100 cycles, offering a promising potential for the practical uses.
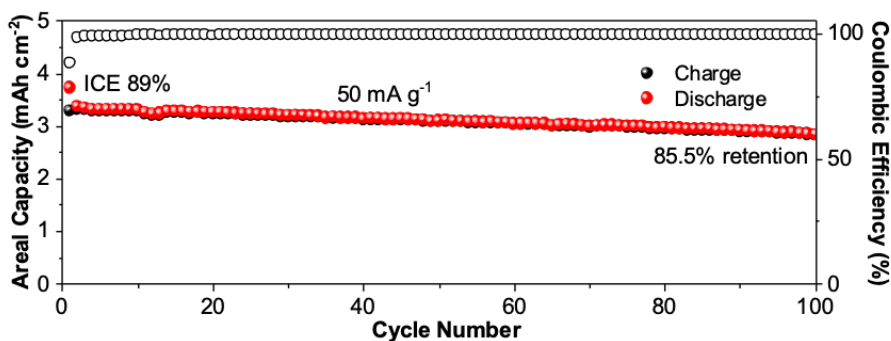
Figure 3.14 Cycling performance of Si/graphite composite material (8 wt.% Si and 92 wt.% graphite) with a specific capacity of ~510 mAh g^{-1} and an areal capacity of ~3.2 mAh cm^{-2}. Current density: 50 mAh g^{-1}.

3.4 Conclusions

In conclusion, we successfully developed an efficient RBM strategy for large-scale preparation of Si-PVA nanocomposites as anode materials for LIBs by using in situ chemical reaction between silicon particles and the hydroxyl groups on PVA chains. The Si-PVA nanocomposite with 5% PVA exhibits a primary size of Si within 200 nm coated by PVA through Si-O-C covalent bond on the surface. By varying the weight ratio of PVA, the sizes of the particles can be regulated, among which 5% PVA coated silicon particles demonstrate optimal electrochemical performances. At 0.2 A g^{-1}, the RBM Si-5%PVA delivers a reversible capacity over 1526 mAh g^{-1} after 100 cycles, with an ICE over 86.1% and an average CE of 99.2%. Raising the current to 3.0 A g^{-1}, a capacity around 800 mAh g^{-1} after 150 cycles can be maintained. The superior electrochemical performance can be attributed to the following aspects: (1) nanosized Si particles from ball milling greatly shorten the diffusion pathway of Li$^+$, leading to enhanced kinetics; (2) polymer coating effectively reduces the size of primary nanoparticles; (3) the resilient PVA coating layer with robust covalent bond is adaptive to the volume change of silicon particles. Therefore, the severe pulverization of Si-based anode is effectively alleviated. In addition, the synthetic strategy features one-pot and solvent-free reaction without post-procedure, as well as low cost of the raw materials, thus being suitable for industrial manufacturing. Moreover, the obtained Si particles can be well mixed with commercial graphite to produce compatible composite anode materials that offer great cycling stability and rate capability, even with a high mass loading. Thus, the RBM method developed in this work offers a feasible approach to fabricate Si-based anode materials for next-generation LIBs.

Chapter 4: **Electrolyte Membranes with Biomimetic Lithium-Ion Channels**

4.1 Introduction

The increasing adoption of electric vehicles necessitates lithium-ion batteries (LIBs) with high-performance characteristics such as improved energy density, faster charging time, prolonged lifetime, and improved safety.[19,211] Similar to other electrochemical-energy-storage devices, LIBs operate through charge separation that generates electrons and lithium ions in one electrode, transport of the electrons and ions respectively through the external circuit and electrolyte, and recombination of the electrons and ions on the other electrode.[20] As an essential component of this continuous process, transport of lithium ions heavily governs the performances of LIBs.[212]

Most commercial LIBs adopt liquid electrolytes, which consist of lithium salts dissolved in organic solvents, allowing fast translocation of the solvated ions in the electrolytes.[213] However, lithium ions (Li^+) and the solvent molecules tend to form bulky solvation sheaths, which reduce the mobility of Li^+.[214] As a consequence, the Li^+ transference number (t_{Li}^+) of the electrolytes, defined as the ratio of Li^+ conductivity *vs.* the total ionic conductivity, is typically less than 0.5.[215] In addition, since the anions are not involved in the relevant electrochemical reactions of LIBs, the charging and discharging process creates an anion concentration gradient across the electrolyte, causing joule heating, particularly during fast charging and discharging.[134] Meanwhile, such a concentration polarization also induces parasitic reactions that shorten the lifespan of the battery.[216,217] Although extensive studies have been explored to improve the t_{Li}^+ in liquid electrolytes, mainly by covalently grafting the anions on inorganic particles to reduce their mobility[162] or by using Li^+-conducting ionomers (e.g., Nafion) with pendant anionic moieties (e.g.,

lithium sulfonates)[218], these approaches typically result in low ionic conductivity on the order of magnitude of 10^{-5} S cm^{-1}.[163,219–222]

In contrast to the transport of ions in electrolytes, biological organisms can transport ions in a highly effective and selective fashion through ion channels.[223] As illustrated in **Figure 4.1a**, ion channels are narrow tunnel-like membrane proteins with negatively charged terminals (e.g., deprotonated carboxylic acids) decorated along the pore channels filled with water molecules, selectively allowing facile passage of specific cations (e.g., Na$^+$ and K$^+$) while electrostatically repulsing anions (e.g., Cl$^-$) without consumption of metabolic energy.[224,225] We envision that electrolytes with improved t_{Li}^+ could be achieved by using a nanoporous scaffold, of which the pore surface is decorated with negatively-charged moieties such as lithium sulfonate groups. Mimicking ion channels in biological systems, the negative moieties within the nanoporous channels should allow effective transport of Li$^+$ while electrostatically repelling the anions, leading to a high t_{Li}^+.

Metal-organic frameworks (MOFs), a class of nanoporous solids constructed from metal cornerstones and organic ligands with tunable structure topology and pore functionality, are excellent scaffolds to construct such biomimetic ion channels.[226,227] For demonstration, UiO-66-NH$_2$ (denoted as UN), a MOF with the formula $Zr_6O_4(OH)_4[BDC-NH_2]_6$ constructed by $Zr_6O_4(OH)_4$ hexanuclear clusters and bridging ligands (2-aminoterephthalic acid, BDC-NH$_2$), was utilized in this work.[228] As depicted in **Figure 4.1b**, UN is assembled by two types of building blocks: a tetrahedron cage and an octahedron cage, which offer two sizes of microporous cavities with triangular-shape window apertures.[229] Moreover, the amine moieties in the ligands could be readily grafted with negatively charged sulfonate (SO$_3^-$) groups via chemical modifications, structurally mimicking the anionic terminals of ion channels (**Figure 4.1c**).[230,231]
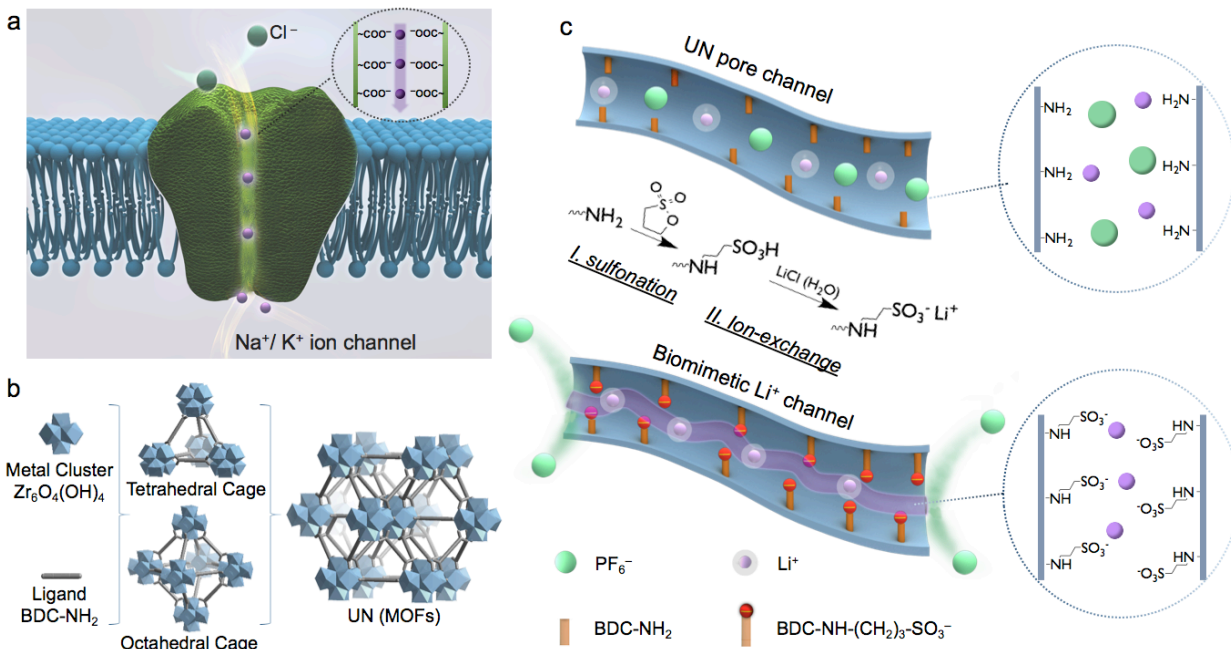
Figure 4.1. (a) A schematic illustration of an ion channel with negatively charged terminals in a cell membrane. (b) Structural fragments of UN comprising super tetrahedrons and octahedrons constituted by the metal clusters and ligands. (c) Illustrative drawings showing a biomimetic Li^+ channel constructed by grafting anionic sulfonate groups on the pore channels of UN.

Note that we have recently developed solid-like electrolytes by MOFs containing unsaturated metal sites (UMSs). Upon filling the pore channels of the MOFs with liquid electrolytes, the anions are spontaneously complexed with the UMSs, allowing effective transport of Li^+ within the porous channels.[232,233] Similarly, composite separators for LIBs with improved t_{Li^+}, rate performance and lifespan were also fabricated by electrospinning a mixture of polymer and MOFs with UMSs.[234] These approaches rely on the complexation of anions with UMSs to facilitate the transport of lithium ions and improve the t_{Li^+}; however, not all MOFs contain UMSs,

which limits the applicability of this strategy.[235,236] The present work circumvents this limitation by modifying the bridging ligands with negatively charged moieties, mimicking ion channels for effective transport of lithium ions in electrolytes.

4.2 Experimental Section

Synthesis of UN-SLi. UN was synthesized according to reported literature through a hydrothermal reaction.[229] As-synthesized UN was mixed with excess 1,3-propanesultone in CHCl$_3$. After stirring at 45 °C for 12 h, the bright yellow solid was collected through centrifugation. The solid was washed by CHCl$_3$ three times then dried at 80 °C to obtain UN-SH. UN-SLi was prepared by reacting UN-SH with excess LiCl aqueous solution. The final UN-SLi was collected by filtering, washed by water and ethanol for three times each, and dried at 120 °C under vacuum for complete removal of water.

Preparation of REF and UN-SLi-EM. UN-SLi-EM was prepared by homogenously mixing 480 mg of MOFs (UN-SLi) with 320 mg of P(VdF-HFP) powders in 10 mL of dimethyl carbonate (DMC) and 2 mL of ethylene carbonate (EC) for 24 h (ambient temperature). 150 μL of resulting suspension was uniformly added to each side (300 μL in total) of a glass-fiber separator (18.5 mm in diameter, Whatman, GF/C). REF was prepared by a similar process without MOFs. After evaporation of DMC solvents, all membranes were stored in glove box for future characterizations.

Approximation of the Debye length of sulfonate groups. Assuming the lithium sulfonate groups ionize completely in the EC/DEC solvents, the following formula of Debye length for symmetric monovalent electrolytes is used for the calculation: $\lambda_D = (\varepsilon_r \varepsilon_0 k_B T / q^2 \Sigma z_i^2 (N_A c_i))^{1/2}$ [237,238] (1), where λ_D is the Debye length in electrolyte solutions, ε_r is the relative dielectric constant of the solvent,

$\varepsilon_0 = 8.85 \times 10^{-12}$ F·m^{-1} is the vacuum permittivity, $k_B = 1.38 \times 10^{-23}$ J K^{-1} is the Boltzmann constant, T is the absolute temperature in kelvin, $q = 1.60 \times 10^{-19}$ C is the elementary charge, z_i is the charge number of the ion, $N_A = 6.02 \times 10^{23}$ mol^{-1} is the Avogadro constant, and c_i is the molar concentration of the ion in the electrolyte (mol L^{-1}). At T = 298 K (25 °C), ε_r for DEC is 2.82, while EC alone has a melting point higher than T = 298 K. Therefore, $\varepsilon_r = 90.36$ at T = 313 K for EC is used as an approximation.[239] The dielectric constant for the mixed EC/DEC solvents is considered roughly linear[240], thus $\varepsilon_r = 46.59$ can be estimated for the EC/DEC solvents (volume ratio 1:1). Considering the chemical formula of UN-SLi ($Zr_6O_{38.3}C_{54.3}H_{44.5}N_6S_{2.1}Li_{2.1}$) and the available liquid electrolyte in UN-SLi-EM (12 mg of UN-SLi in 160 μL of electrolyte), a molar concentration of the negatively charged sulfonate residues can be calculated as 7.8×10^{-2} mol L^{-1}. Taking all the derived numbers into formula (1), a Debye length of $\lambda_D = 8.4$ Å can be approximated.

Electrochemical studies. All electrochemical characterizations were carried out by adding an equivalent amount of liquid electrolyte (160 μL of 1M LiPF$_6$ in EC/DEC with 5 wt% FEC) to the membranes studied (UN-SLi-EM, REF). CV tests (Biologic VMP3) were conducted in coin-cell configuration with a scan rate of 1.0 mV s^{-1} between −0.2 and 5.0 V, where lithium chips were utilized as reference/counter electrodes and stainless-steel plates were used as the working electrodes.

The ionic conductivity (σ, S cm^{-1}) was measured by sandwiching electrolyte-saturated membranes by two blocking electrodes (stainless steel plates) and calculated based on the following equation: $\sigma = 4L/\pi RD^2$, where σ is conductivity, L (cm) and D (cm) are thickness and diameter of the membranes, respectively, and R (Ohm) is the resistance obtained from EIS (Solartron 1860/1287) by AC amplitude of 10 mV from 10^6 to 1 Hz. Activation energies (E_a) from

the Arrhenius behavior of conductivity ($\sigma = \sigma_0 \exp(-E_a/RT)$) were derived by linear fitting between log σ and 1000/T with a linear fitting coefficient over 0.99.

Determination of t_{Li^+} was performed through the combined measurement of alternating-current (AC) impedance and potentiostatic polarization. The time dependence of the current was detected via Li|Li symmetric cell with a voltage of 20 mV (ΔV) applied, during which the initial current (I_0) was monitored until reaching the steady-state current (I_{ss}). The same cell was monitored to measure the resistance of the electrolyte and the electrolyte–Li metal interface by EIS before (R_0) and after (R_{ss}) (10^6 to 1 Hz, 10 mV amplitude) applying the voltage. t_{Li^+} can be calculated with the following expression: $t_{Li^+} = I_{ss}(\Delta V - I_0 R_0)/ I_0(\Delta V - I_{ss} R_{ss})$.[157]

Li stripping and plating tests were performed using Li|Li cells by galvanostatically charging and discharging (Landt instrument) for a period of 2 h each at a current density of 1.0 mA cm^{-2}, except for initial 10 cycles at 0.2 mA cm^{-2}. The post-mortem evaluations on Li electrodes and UN-SLi-EM membranes were carried out by dissembling Li|Li cell after 50 cycles (200 h). Cu|Li asymmetric cells were assembled by a lithium chip and copper foil (15 μm in thickness) in a coin cell. Each cycle includes plating lithium on the copper with a current density of 1.0 mA cm^{-2} for 2 h and stripping to voltage cutoff at 1.0 V (*vs*. Li/Li$^+$).

Prototype batteries were fabricated by assembling a conventional LiFePO$_4$ cathode and a Li chip in coin cells (2.5 to 4 V *vs*. Li/Li$^+$ for LiFePO$_4$). The LiFePO$_4$ cathodes were prepared by homogenously blending LiFePO$_4$ (MTI), acetylene black, and polyvinylidene difluoride (PVdF) at a ratio of 8:1:1 in N-Methyl-2-pyrrolidone (NMP). The resulting slurry was uniformly coated on a conductive carbon-coated Al foil and dried in a vacuum oven at 90 °C for 12 h. The specific capacity is calculated based on the active materials in the cathode, corresponding to an areal mass

loading of 2 mg cm^{-2}. 1C charging and discharging rate here is defined as 150 mA g^{-1} for LiFePO$_4$. All the electrochemical tests were carried out at ambient temperature ($\approx$ 25 °C) unless specified.

Materials characterizations and structural analysis. Crystalline structures of MOFs samples were determined by the Rigaku powder X-ray diffractometer (XRD) using Kα radiation (λ = 1.54 Å). Surface morphology and particle sizes were investigated by scanning electron microscopy (Nova 230 Nano SEM) and transmission electron microscopy (FEI T12 Quick CryoEM and CryoET TEM). N$_2$ sorption/desorption measurements were conducted using a Micromeritics ASAP 2020 system at 77 K. Prior to the measurement, all samples were degassed at 120 °C for 12 h. All ^{1}H NMR samples were prepared by completely digesting MOFs samples in 30 µL HF solution and 570 µL DMSO-d6. AV400 was used with 5 mm broadband with Z gradient. Inductively coupled plasma atomic emission spectroscopy (ICP-AES) was performed using Shimadzu ICP-9000 instrument. The UN-SLi was digested by concentrated HNO$_3$ and HCl (vol. 1:3), dried to remove the liquid, and redissolved in 5% HCl solution for the ICP-AES test. X-ray photoelectron spectroscopy (XPS) measurements were performed on an AXIS Ultra DLD instrument. The samples were prepared in glovebox before quickly transferred to a high-vacuum chamber. The obtained raw XPS spectra were calibrated by C 1s peak at 284.8 eV and then fitted based on Gaussian−Lorentzian functions and Shirley-type background. Raman spectroscopy was conducted on a Renishaw 2000 System with a He/Ne laser at a wavelength of 633 nm. Zeta potential was measured on Zetasizer Nano instrument (Malvern) with isopropanol as the solvent.

COMSOL Multiphysics Simulation. The model includes following processes: (1) charge transport: electronic charge transport in electrodes, and ionic charge transport in electrolyte; (2) species transport: in electrolyte, and within particles of electrodes; (3) Butler-Volmer electrochemical kinetics for electrodes. As for domains, the model uses: (1) liquid electrolyte (1M

LiPF$_6$ salt in carbonate solvents) in porous separator; (2) positive porous electrode (LiFePO$_4$ particles as active material), partial physical properties are obtained from manufacturer datasheet; (3) at negative electrode, lithium foil is used as planar electrode. As for boundary conditions, (1) on the current collector/active material boundaries, for electronic current balance, electric potential is set 0 V at the negative electrode, and current density is given by applied discharge rate at the positive electrode; (2) current collector/active material boundaries are insulating for ionic charge balance; (3) at particle surfaces in electrodes, the species flux is determined by Butler-Volmer equation (reaction rates of electrochemical reactions).

4.3 Results and Discussions

UN particles with high crystallinity and porosity were synthesized by a reported hydrothermal approach.[229] **Figure 4.2a,b** present the transmission electron microscopy (TEM) and scanning electron microscopy (SEM) images of UN particles, respectively. The as-synthesized UN shows a well-defined octahedral shape with a uniform particulate size of 150 nm. Post-synthetic decoration of UN yields an anionic MOF, which is achieved by two-step modifications, that is, the reaction of UN with 1,3-propanesultone[231] (the product is denoted as UN-SH) and subsequent ion-exchange process with Li$^+$ (the product is denoted as UN-SLi). As shown in **Figure 4.3a**, the crystal structures of UN, UN-SH and UN-SLi were examined by X-ray powder diffraction (XRD), all of which are indexable to a simulated UN pattern.[229] Despite a slightly downshifted (200) peak ($2\theta = 8.5°$) observed due to ligand modification[230,241], the crystallinity and morphology (**Figure 4.2c,d**) of the modified UN particles are consistently preserved.
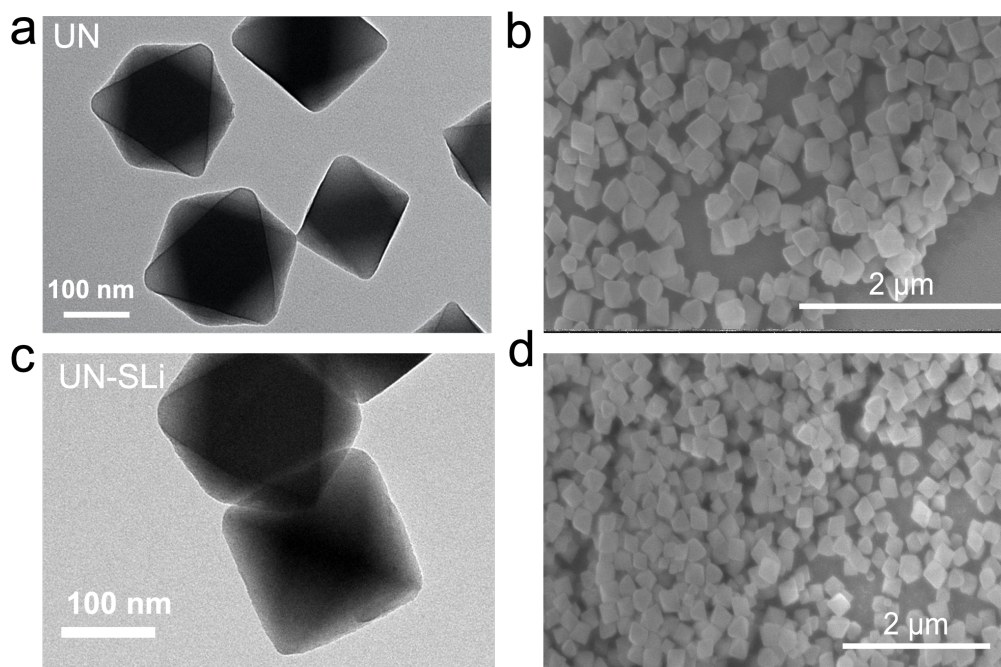
Figure 4.2 TEM images of (a) as-synthesized UN and (b) UN-SLi. SEM image of (c) as-synthesized UN and (d) UN-SLi.

N$_2$ adsorption/desorption isotherms, as well as the corresponding pore size distributions of UN, UN-SH and UN-SLi, are displayed in **Figure 4.3b** and **Figure 4.3c**, respectively. The pristine UN exhibits a Brunauer–Emmett–Teller (BET) surface area of 921.3 m^2 g^{-1} and a total pore volume of 0.473 cm^3 g^{-1}, which decreases to 659.8 m^2 g^{-1} and 0.367 cm^3 g^{-1} after the sulfonation modification (UN-SH), signifying a successful introduction of –(CH$_2$)$_3$SO$_3$H groups to the porous scaffold. Correspondingly, UN-SLi shows a slightly declined surface area of 627.2 m^2 g^{-1} and a pore volume of 0.357 cm^3 g^{-1}. Based on a Density Functional Theory (DFT) model, the pore size distribution analysis of UN indicates two types of pores with diameters of 7.5 Å and 11.5 Å, which are respectively consistent with the sizes of the tetrahedron and octahedron building units of UN

as illustrated in **Figure 4.2**a. The pore volume of the octahedron cavity (11.5 Å) notably decreases with the graft modification, which is accompanied by an increasing pore volume peaking at a diameter slightly higher than 7.5 Å ($\approx$ 8 Å).[229,242] The dominant pore diameter is thus reduced from 11.5 Å for UN to 8 Å for UN-SLi, which could be reasonably interpreted by the major modification in the octahedron cavities.
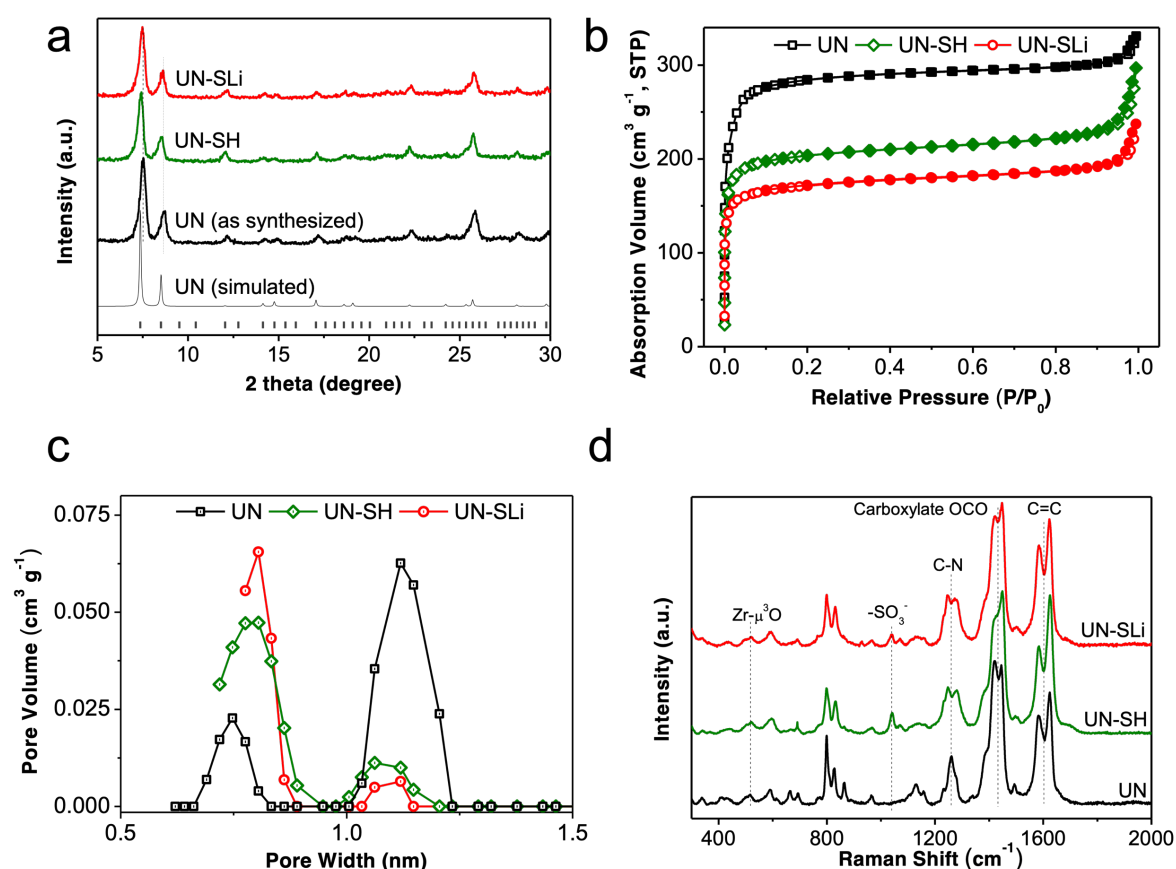
Figure 4.3 (a) XRD patterns of UN, UN-SH and UN-SLi. A simulated UN pattern is also plotted at the bottom. (b) N_2 adsorption/desorption isotherms of UN, UN-SH and UN-SLi. (c) Micropore size distributions of UN, UN-SH and UN-SLi obtained from a DFT model. (d) Raman spectra of UN, UN-SH and UN-SLi.

The evolution of the chemical structure during the modification was probed by Raman spectroscopy. **Figure 4.3d** shows the Raman spectra of UN, UN-SH and UN-SLi, in which the peaks at 510 cm^{-1}, 1420/1450 cm^{-1} and 1580/1625 cm^{-1} are attributed to the Zr-μ^3O (metal clusters), COO$^-$ (carboxylate of ligands) and C=C (phenyl of ligands) vibrations from the MOF skeleton, respectively.[243,244] An emergence of new sulfonate peaks at 1040 cm^{-1} for UN-SH and UN-SLi elucidates the successful installation of $-(CH_2)_3SO_3^-$ groups[245]. A pronounced peak at 1260 cm^{-1} of UN is associated with C-N bonds (BDC-NH$_2$). This peak is shifted and split into two peaks at 1247 cm^{-1} and 1280 cm^{-1} for both UN-SH and UN-SLi, suggesting multiple bonding configurations of the C-N bonds after grafting $-(CH_2)_3SO_3^-$ on the $-NH_2$ groups.[246,247] In addition, to verify the formation of negatively charged ion channels in UN-SH and UN-SLi, zeta potential measurements were performed in a non-aqueous environment for UN, UN-SH and UN-SLi powders (**Figure 4.4a**)). UN shows a near-zero zeta potential, whereas UN-SH and UN-SLi particles show a zeta potential of -15 mV, confirming that UN-SH and UN-SLi are negatively charged.

Proton nuclear magnetic resonance (^{1}H NMR) was utilized to quantitatively determine the degree of the modification (**Figure 4.4b**). The chemical shifts of both UN and UN-SH at around 7.0, 7.3 and 7.7 ppm are ascribed to the hydrogens (marked as H$_A$, H$_B$ and H$_C$) on the benzene ring of the ligand.[230] The chemical shifts of UN-SH at around 2.0 and 3.2 ppm are identified as the hydrogens (marked as H$_D$, H$_E$ and H$_F$) on the alkyl chain of the grafted groups ($-(CH_2)_3SO_3^-$). By comparing the integrals of the ^{1}H peaks from the ligands and the grafted groups, it is estimated that ~ 35 mol% of the ligands were functionalized with $-(CH_2)_3SO_3^-$ groups. Consistently, the molar ratio of Li to Zr in UN-SLi was 0.355, as determined by inductively coupled plasma atomic

emission spectroscopy (ICP-AES), demonstrating that ~ 35.5% of the ligands in UN are equipped with Li$^+$ (**Table 4.1**). The coincident results from ^{1}H NMR and ICP-AES confirm the complete ion-exchange after the second modification step. Assuming no synthetic defects present in UN ($Zr_6O_4(OH)_4[BDC-NH_2]_6$), the formula of UN-SLi is approximated as $Zr_6O_4(OH)_4[BDC-NH_{1.65}(C_3H_6SO_3Li)_{0.35}]_6$.
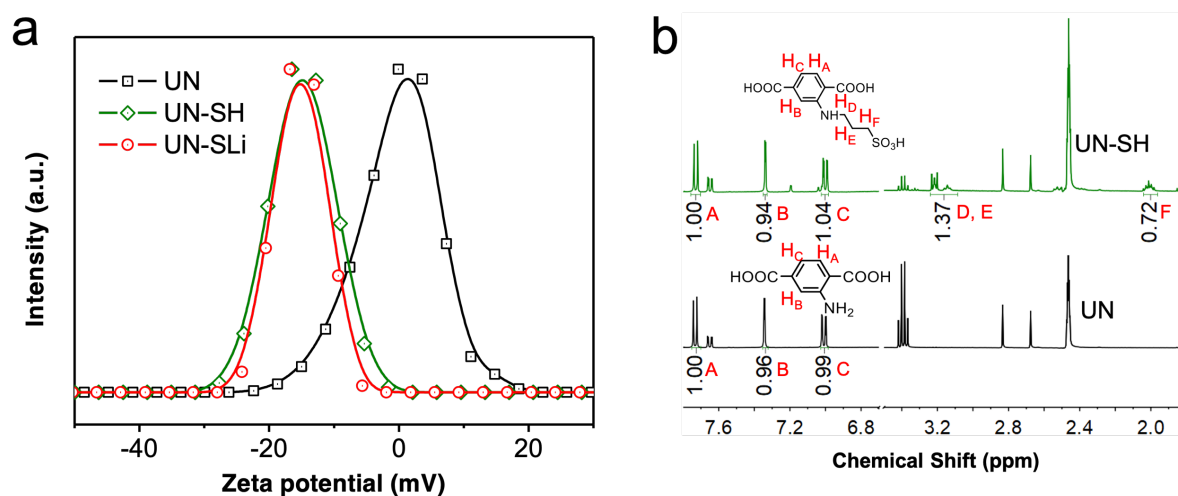
Figure 4.4 (a) Zeta potential measurements of UN, UN-SH and UN-SLi in organic medium (isopropanol). (b) ^{1}H NMR spectra of UN and UN-SH (3.8-6.6 ppm is omitted).

Table 4.1. ICP-AES measurement for UN-SLi.

Element	weight concentration (mg L^{-1})	molar concentration (mmol L^{-1})	molar ratio (Li/Zr)
Zr	19.2	0.21	
			35.5%
Li	0.517	0.0745	

91

To implement such ion-selective materials for battery applications, UN-SLi particles and poly(vinylidene fluoride-co-hexafluoropropylene) (P(VdF-HFP)) were infiltrated in a glass-fiber separator to form electrolyte membranes (denoted as UN-SLi-EM). As a reference, a composite separator membrane was also fabricated by impregnating bare P(VdF-HFP) into a glass-fiber separator (denoted as REF). **Figure 4.5a** and **Figure 4.5b** show the SEM images of REF and UN-SLi-EM, respectively, where REF displays a smooth surface while UN-SLi-EM shows a coating of UN-SLi particles. The insets show photographs of these membranes, where UN-SLi-EM shows a bright yellow color due to the presence of UN-SLi.
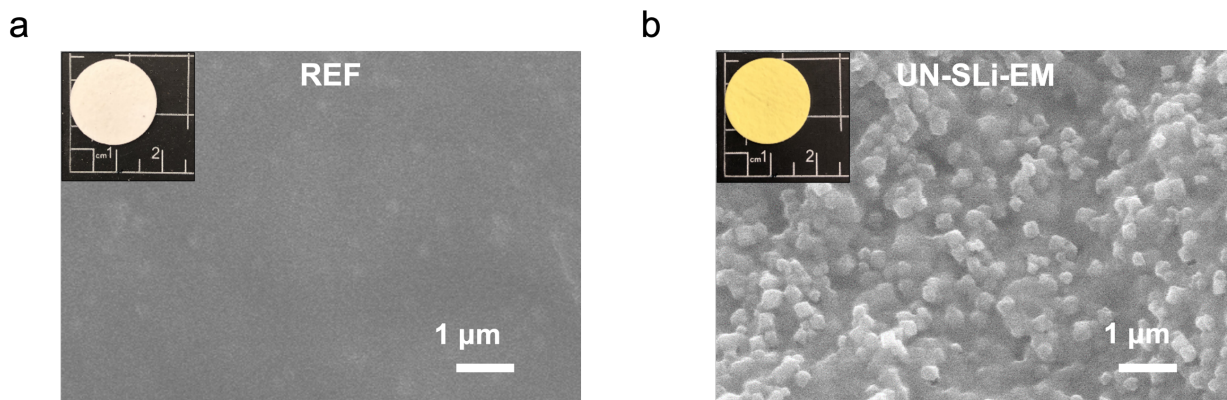
Figure 4.5 SEM images of (a) REF and (b) UN-SLi-EM; insets show the respective photographs.

We first evaluated the electrochemical stability of electrolytes in the electrolyte membranes. Cells were assembled using stainless steel plates as the working electrode, Li-metal as the reference/counter electrode, and REF or UN-SLi-EM with 160 μL 1M $LiPF_6$ in ethyl carbonate (EC)/diethyl carbonate (DEC) with 5 wt% fluoroethylene carbonate (FEC) as the electrolyte.

Figure 4.6a displays the cyclic voltammetry (CV) curves of the cells, where the redox peaks near 0 V (*vs*. Li/Li$^+$) are associated with Li$^+$ stripping and plating. The curve of the cell using UN-SLi-EM resembles the REF in terms of stripping/plating currents and electrochemical stability (see inset for enlarged CV), implying the intactness of the sulfonate groups. Meanwhile, the ionic conductivity of liquid electrolytes in these membranes was determined by electrochemical impedance spectroscopy (EIS) using two identical stainless-steel plates as blocking electrodes. Meanwhile, the ionic conductivity was determined by electrochemical impedance spectroscopy (EIS) using two identical stainless-steel plates as blocking electrodes (**Figure 4.6b,c**). As summarized in **Figure 4.6d**, the electrolytes in REF and UN-SLi-EM exhibit ionic conductivity of 0.96 mS cm^{-1} and 0.9 mS cm^{-1} at ambient temperature, respectively.
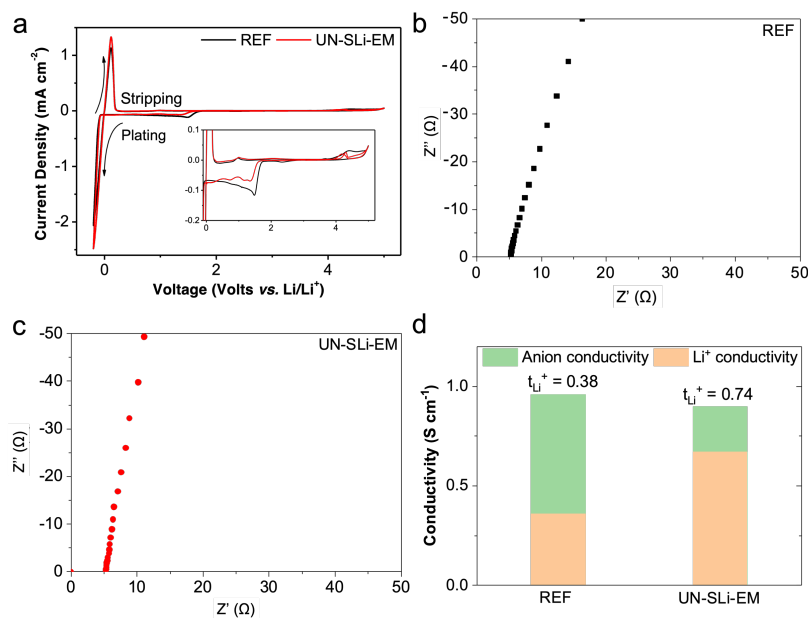
Figure 4.6 (a) CV curves of liquid electrolytes in REF and UN-SLi-EM using stainless steel as working electrode and Li as counter/reference electrodes (inset shows the enlarged view). Nyquist plots of (b) REF and (c) UN-EM with equivalent liquid electrolyte (160 μL of 1M LiPF$_6$

in EC/DEC) at ambient temperature. Note: the resistivity of electrolyte membranes was determined by the intercept of the plots with real axis. (d) Ionic conductivity and t_{Li}^+ of liquid electrolyte in REF and UN-SLi-EM, where the Li^+ and anion conductivities are partitioned based on t_{Li}^+.

The t_{Li}^+ was measured in Li symmetric (Li|Li) cells using a classical potentiostatic method.[248] As shown in **Figure 4.7**, the calculated t_{Li}^+ of electrolyte is doubly enhanced from 0.38 in REF to 0.74 in UN-SLi-EM. Considering their comparable ionic conductivity, the effective Li^+ conductivity is considerably increased from 0.36 mS cm^{-1} for REF to 0.67 mS cm^{-1} for UN-SLi-EM (**Figure 4.6d**). This observation clearly confirms the ion-channeling effect, where the negatively charged channels selectively repel the passage of anions and allow effective translocation of cations. Note that the Debye length of the SO_3^- groups in electrolyte is estimated as 8.4 Å, which is larger than the opening window of modified pore channels (~ 8 Å). Consistently, the electrostatic shielding effect of the SO_3^- groups persists within the Debye sphere, mimicking biological ion channels by restricting the permeation of PF_6^- anions (~ 5.1 Å[249]) and favoring the passage of Li^+ cations (~ 0.7 Å[250]).
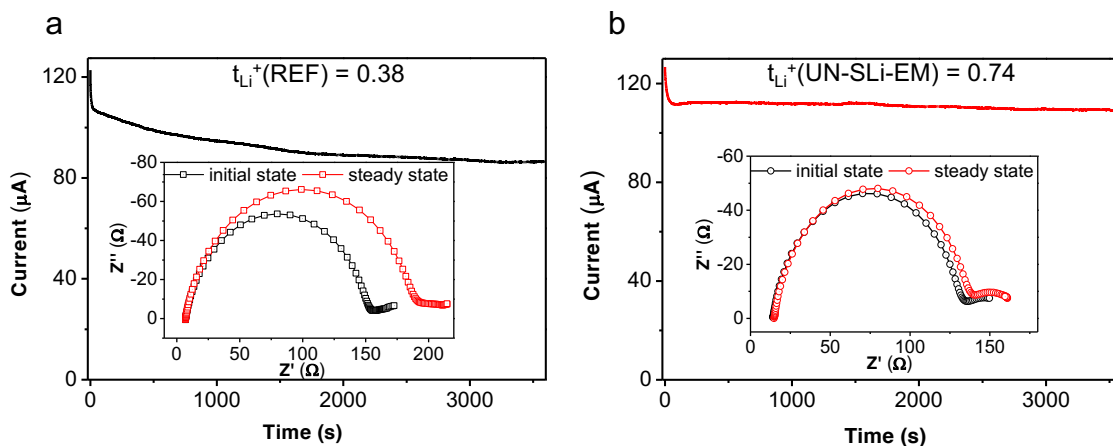
Figure 4.7 t_{Li}^+ measurements of liquid electrolytes in (a) REF and (b) UN-SLi-EM using potentiostatic polarization (insets: Nyquist plots before and after polarization).

The long-term interfacial stability between UN-SLi-EM and Li metal was characerized by galvanostatically cycling Li|Li cells at 1 mA cm^{-2} with areal capacity of 2 mAh cm^{-2}. **Figure 4.8a** compares the overpotential of the cells as a function of test time. The cell with UN-SLi-EM shows a smooth voltage plateau ~ 50 mV for each charging-discharging cycle that maintains stable for 600 h without an increase in polarization or dendrite-induced failure (**Figure 4.9**). In comparison, the cell with REF shows a severely fluctuating voltage profile with average overpotential of ~ 100 mV due to inhomogeneous electrodeposition. The smaller and more stable overpotential curve of the cell using UN-SLi-EM demonstrates that alleviating the concentration gradient contributes to a less resistive and more robust electrolyte interface with metallic Li. The coulombic efficiency of Li$^+$/Li plating-stripping was further evaluated in asymmetric (Cu|Li) cell, where the coulombic efficiency is defined by the ratio of the amount of stripped Li to that of the plated Li (2 mAh cm^{-2}) on Cu. As shown in **Figure 4.8b**, the cell using UN-SLi-EM retains an average coulombic efficiency of 92.4% for 100 cycles without short-circuiting (**Figure 4.10**). In contrast, the cell using REF delivers an average coulombic efficiency of 90.5% for the first 40 cycles, followed by a rapid decay to 70% or less after 70 cycles. The higher coulombic efficiency of Cu|Li cell using UN-SLi-EM substantiates that blocked anion mobility and improved Li$^+$ conductivity significantly suppresses parasitic reactions of electrolyte and affords more reversible Li electrodes.
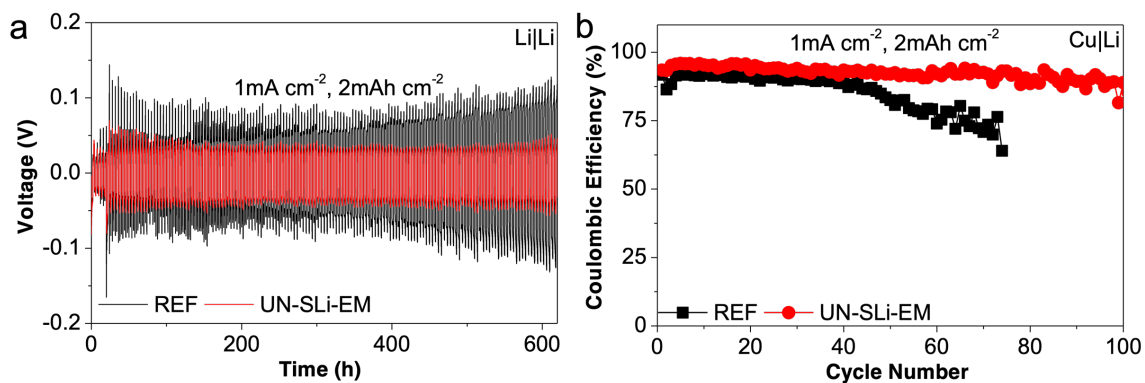
Figure 4.8 (a) Galvanostatic cycling of Li|Li cells at 1.0 mA cm^{-2} for 2 h each cycle (0.25 mA cm^{-2} for initial 20 h). (b) Coulombic efficiency of Cu|Li cells at fixed plating capacity of 2 mAh cm^{-2} (1.0 mA cm^{-2}).
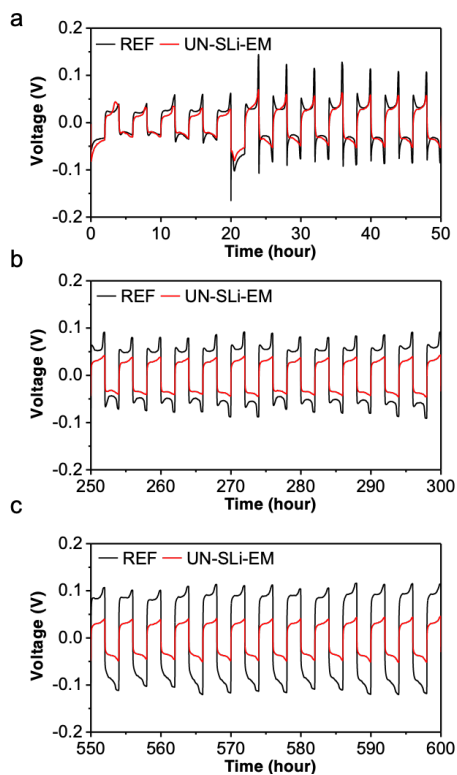
Figure 4.9 Enlarged time-dependent voltage profiles from the Li|Li cells at segments of (a) 0-50 h, (b) 250-300 h, and (c) 550-600 h. Areal capacity of 0.5 mAh cm^{-2} at 0.25 mA cm^{-2} for the initial 20 h and 2.0 mAh cm^{-2} at 1.0 mA cm^{-2} for cycles afterwards.
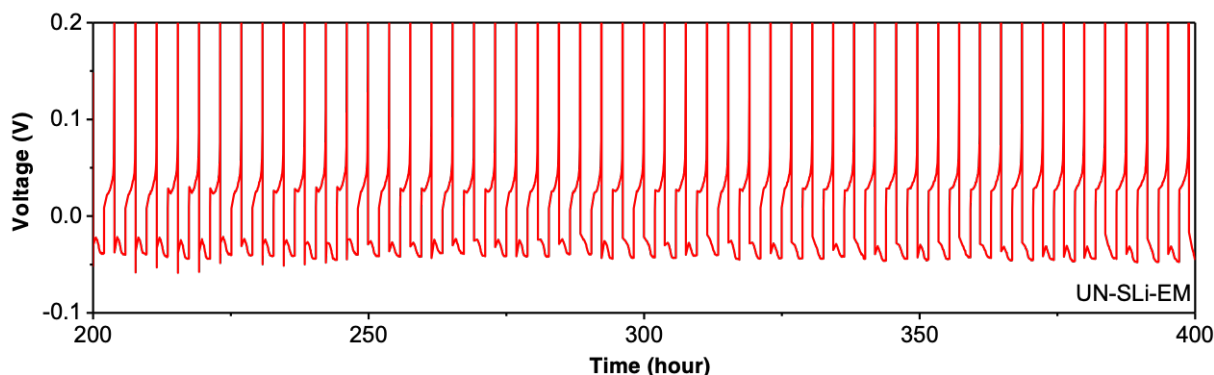
Figure 4.10. Time-dependent voltage profile (50th to 100th cycle) of Cu|Li cell using UN-SLi-EM.

For post-cycle analysis, Li electrodes from the cycled Li|Li cells were harvested and examined by SEM (**Figure 4.11**). Compared with the Li from the cell with UN-SLi-EM, the cycled Li with REF shows considerably rougher morphology. The species composition of anion on the electrode surface was analyzed by X-ray photoelectron spectroscopy (XPS) (**Figure 4.12a**). Decomposition products of PF$_6^-$ are clearly observed, including LiF (685.2 eV) from the F 1s spectra and Li$_x$PO$_y$F$_z$ (134.3 eV) from the P 2p spectra.[251,252] Significantly less amount of LiF and Li$_x$PO$_y$F$_z$ are present on cycled electrode from the cell using UN-SLi-EM, suggesting that the UN-SLi-EM could effectively alleviate polarization and reduce decomposition of PF$_6^-$ of electrolyte. The relatively weak –CF$_2$–CH$_2$– signal from the F 1s spectra of cycled electrode using UN-SLi-

EM indicates reduced attachment of P(VdF-HFP) onto Li surface as UN-SLi particles decrease the direct contact between Li and polymer. **Figure 4.12b** shows the S 2p spectra from the sulfonate group (168.9 eV), as well as the Zr 3d spectra from the Zr^{4+} metal clusters (181.5/184.0 eV), before and after the cycling.[253] Those similar spectra imply the excellent stability of UN-SLi-EM, which is further confirmed by Raman spectroscopy (**Figure 4.13a**) and XRD (**Figure 4.13b**) studies.
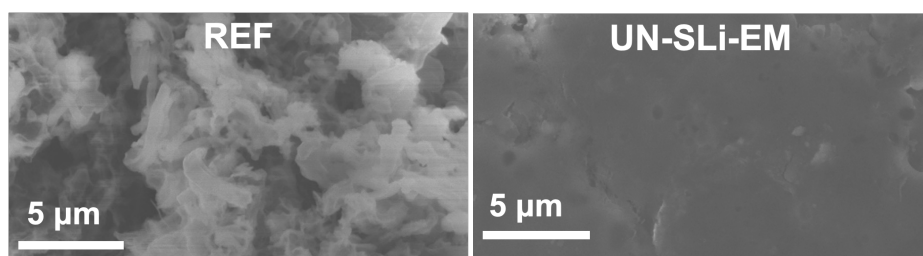
Figure 4.11 SEM images of the cycled Li.
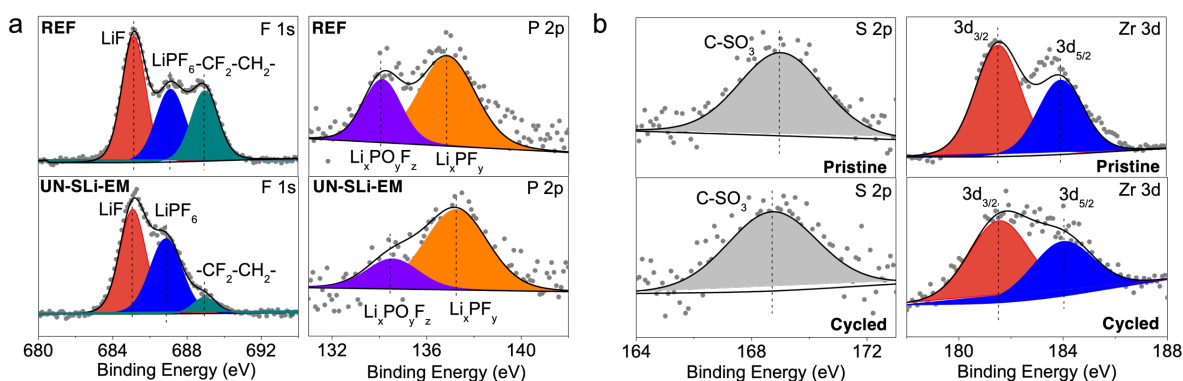
Figure 4.12 (a) XPS spectra of the cycled Li. (b) XPS spectra of UN-SLi-EM before and after cycling.
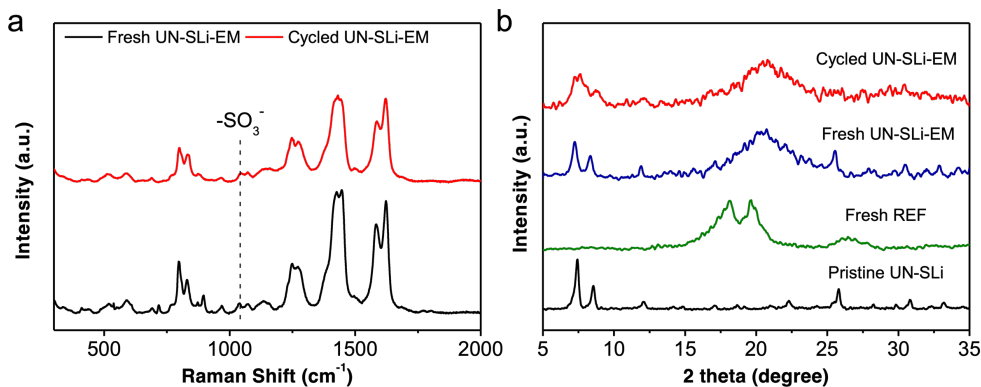
Figure 4.13 Post-cycle evaluations on UN-SLi-EM harvested from Li|Li cycling. (a) Raman spectrum of UN-SLi-EM comparing the fresh UN-SLi-EM. (b) XRD pattern of fresh and cycled UN-SLi-EM compared to UN-SLi powder and fresh REF.

Prototype lithium batteries were fabricated using $LiFePO_4$ (LFP) as the cathode and Li-metal as the anode (LFP|Li). Stepwise increased rates from 0.1C to 20C were applied on the LFP|Li cells. As shown in **Figure 4.14a**, although these cells show similar specific capacity of 145 mAh g^{-1} at a low rate of 0.1C, the cell with UN-SLi-EM delivers notably higher capacity at higher C rates. For example, the cells using REF shows almost no capacity at 20C, while the cell using UN-SLi-EM still affords a capacity of 45 mAh g^{-1}. As shown in **Figure 4.14b**, cell durability was evaluated at 5C. The cell with REF exhibits a fast capacity fade from 95 mAh g^{-1} to 30 mAh g^{-1} after 1000 cycles, corresponding to a capacity retention of 31%. In sharp contrast, the cell with UN-SLi-EM affords a capacity of 76 mAh g^{-1} after 3000 cycles, equivalent to a capacity retention of 80%. The results support that the channeling effect for ion transport evidently benefits the rate capability and durability under fast charging/discharging.
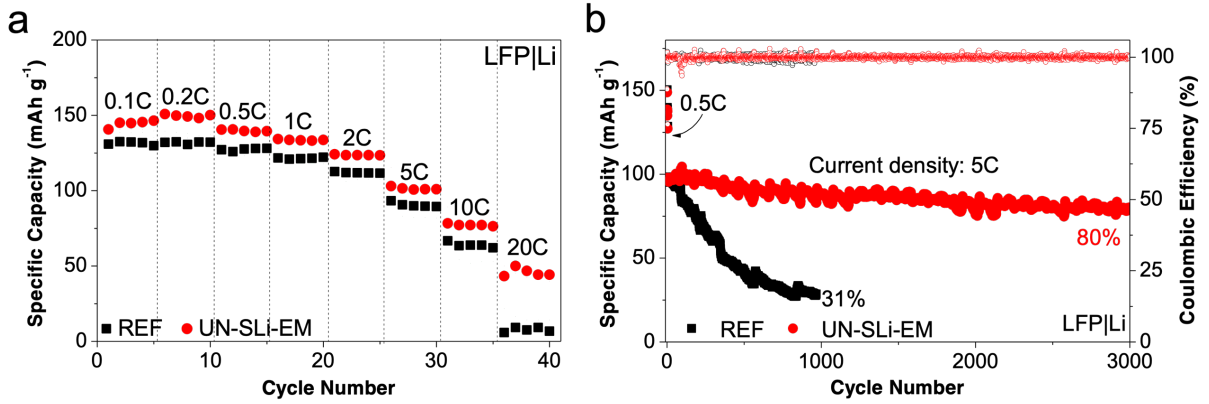
Figure 4.14 (a) Rate performance of LFP|Li cells at various current densities from 0.1C to 20C. (b) Long-term cycling stability of LFP|Li cells at high rate of 5C (0.2C for initial 5 cycles).

To investigate a relationship between ion transport, concentration polarization and output voltage, a conceptual cell (LFP|Li) was modelled in COMSOL Multiphysics® with key parameter inputs from above prototype cell and electrolyte property (**Table 4.2**). A 1-D model on the basis of the pseudo two-dimensional(P2D) model is implemented. The P2D model consists of three components of the battery shown in **Figure 4.15**: positive electrode (cathode, LFP), separator (electrolyte membrane, UN-SLi-EM), negative electrode (anode, Li metal), which denoted respectively by the indexes p, s, and n. Lithium metal is used as the anode that can be treated as a 2-D surface, and thus its thickness is neglected in the simulation. The cathode (LFP) is porous with coexisting solid and liquid phases. Herein, we consider the cell under an isothermal condition without discussing the energy balance.
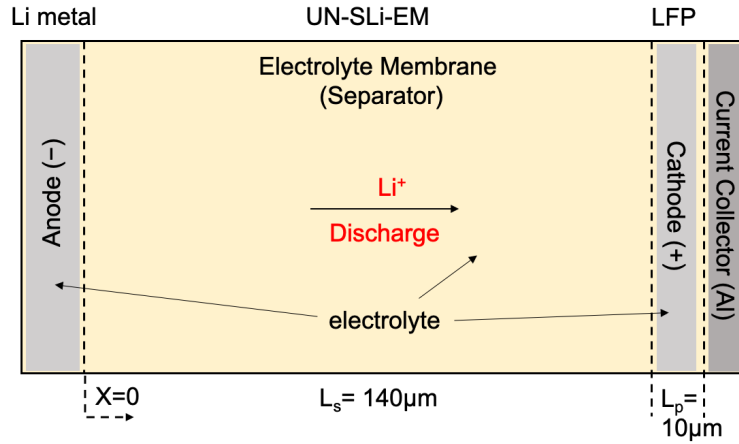
Figure 4.15 Schematic of LiFePO$_4$|Li cell model with 1-D coordination. The governing equations and boundary conditions are summarized in Table 4.2.

Table 4.2. Li-ion P2D model governing equations and boundary conditions.[254,255]

Governing Equations	Boundary Conditions
Positive electrode, $i \in \{p, n\}$	

$\epsilon_i \dfrac{\partial c_e(x,t)}{\partial t} = \dfrac{\partial}{\partial x}\left[D_{eff,i}\dfrac{\partial c_e(x,t)}{\partial x}\right] + a_i(1-t_+)j(x,t)$ (e1)	$-D_{eff,i}\dfrac{\partial c_e(x,t)}{\partial x}\big|_{x=0,L_s+L_p} = 0$ (b1)
	$c_e(x,t)\big|_{x=L_s^-} = c_e(x,t)\big|_{x=L_s^+}$ (b1')
$\dfrac{\partial c_{s,i}(x,r,t)}{\partial t} = D_{eff,i}\dfrac{1}{r^2}\dfrac{\partial}{\partial r}\left(r^2\dfrac{\partial c_{s,i}(x,r,t)}{\partial r}\right)$ (e2)	
	$-D_{s,i}\dfrac{\partial c_{s,i}(x,r,t)}{\partial r}\big|_{r=0} = 0$ (b2)
	$-D_{s,i}\dfrac{\partial c_{s,i}(x,r,t)}{\partial r}\big|_{r=R_{s,i}} = j(x,t)$ (b2')
$a_i Fj(x,t) = -\dfrac{\partial}{\partial x}\left[\kappa_{eff,i}\dfrac{\partial \Phi_e(x,t)}{\partial x}\right] + \dfrac{\partial}{\partial x}\left[\kappa_{eff,i}\gamma T(x,t)\dfrac{\partial \ln c_e(x,t)}{\partial x}\right]$ (e3) $\left(\gamma = \dfrac{2(1-t_+)R}{F}\right)$	
	$-\kappa_{eff,i}\dfrac{\partial \Phi_e(x,t)}{\partial x}\big|_{x=0,L_s+L_p} = 0$ (b3)
$\dfrac{\partial}{\partial x}\left[\sigma_{eff,i}\dfrac{\partial \Phi_s(x,t)}{\partial x}\right] = a_i Fj(x,t)$ (e4)	$\Phi_e(x,t)\big|_{x=L_s^-} = \Phi_e(x,t)\big|_{x=L_s^+}$ (b3')
$j(x,t) = 2k_{eff,i}\sqrt{c_e(x,t)(c_{s,i}^{max}-c_s^*(x,t))c_s^*(x,t)}\sinh\left[\dfrac{0.5R}{FT(x,t)}\eta_i(x,t)\right]$ (e5)	$-\sigma_{eff,i}\dfrac{\partial \Phi_s(x,t)}{\partial x}\big|_{x=L_s+L_p} = I_{app}(t)$ (b4)
	$-\sigma_{eff,i}\dfrac{\partial \Phi_s(x,t)}{\partial x}\big|_{x=L_s} = 0$ (b4')
$\eta_i(x,t) = \Phi_s(x,t) - \Phi_e(x,t) - U_i$ (e6)	$\Phi_s(x,t)\big|_{x=0} = 0$ (b4'')

Separator, $i = s$	
$\epsilon_i \dfrac{\partial c_e(x,t)}{\partial t} = \dfrac{\partial}{\partial x}\left[D_{eff,i}\dfrac{\partial c_e(x,t)}{\partial x}\right]$ (e1')	$-D_{eff,s}\dfrac{\partial c_e(x,t)}{\partial x}\big|_{x=L_s^-} = -D_{eff,p}\dfrac{\partial c_e(x,t)}{\partial x}\big|_{x=L_s^+}$ (b1'')
$0 = -\dfrac{\partial}{\partial x}\left[\kappa_{eff,i}\dfrac{\partial \Phi_e(x,t)}{\partial x}\right] + \dfrac{\partial}{\partial x}\left[\kappa_{eff,i}T(x,t)\gamma\dfrac{\partial \ln c_e(x,t)}{\partial x}\right]$ (e3')	$-\kappa_{eff,s}\dfrac{\partial \Phi_e(x,t)}{\partial x}\big|_{x=L_p^-} = -\kappa_{eff,p}\dfrac{\partial \Phi_e(x,t)}{\partial x}\big|_{x=L_p^+}$ (b3'')

The material balance of electrolyte in the liquid phase is described as (e1) for the (positive) electrode and (e1') for the separator, respectively. At the both ends of the cell, there is no mass flux $j(x,t)$ (b1); at the electrode/separator interface, the concentration of the electrolyte and its mass flux are both continuous (b1', b1''). The material balance of lithium ions in a particle of active material in the solid phase is governed by Fick's second law with spherical coordinates as

(e2). At the center of the particle, there is no mass flux (b2); on the surface of the particle, the mass flux is equal to the pore wall flux for electrode reactions (b2'). Since the anode here is an electrode surface instead of a porous electrode, the equation of particle intercalation is not applicable (e2), but the pore wall flux for electrode reactions still applies. The charge balance in the liquid phase governed by Ohm's law is described as (e3) for the (positive) electrode and (e3') for the separator, respectively. At both ends of the cell, there is no charge flux; at the electrode/separator interface, the electrolyte potential and its charge flux are both continuous (b3', b3''). The charge balance in the solid phase governed by Ohm's law is described as (e4). At the electrode/current collector interface, the charge flux is equal to the applied current density (b4); at the electrode/separator interface, the charge flux is 0 (b4'); at the current collector/negative electrode interface, the solid potential is set to be 0 (b4''). Moreover, the pore wall flux, equal to the consumption/production rate of Li ions due to the electrochemical reaction at the solid/electrolyte interface, is given by Butler-Volmer equation (e5). And the over potential of electrochemical reactions at the solid electrolyte interface is given by (e6) as a function of the solid potential, the electrolyte potential and the thermodynamic equilibrium potential of active materials. As for initial conditions, the electrolyte concentration is set to be 1M; the solid potential is derived from the equilibrium potential functions of the state of charge (lithium concentration) of active material; the electrolyte potential is 0; the temperature is 298 K.

As displayed in **Figure 4.16a,b**, the evolution of concentration gradient was plotted against proceeding of discharge at 20C and cell length, where planar Li anode, separator and LFP cathode were positioned at 0, 0 to $1.4 \cdot 10^{-4}$ and $1.4 \cdot 10^{-4}$ to $1.5 \cdot 10^{-4}$ m, respectively. The initial electrolyte concentration of 1M was polarized progressively as Li^+ were generated at the anode and consumed at the cathode. For the reference electrolyte with the low t_{Li^+} (0.38), a high rate discharging at 20C

gives rise to a steep concentration gradient after 27 seconds, where the anode side accumulates a concentrated 1.8M electrolyte and the cathode completely depletes the salts (0M). As shown in **Figure 4.16c**, the polarized concentration distribution correspondingly produces a reverse electrolyte potential of -0.74 V by the end of discharge (27 seconds) at cathode side, where the electrolyte potential takes both ohmic and concentration polarization into consideration. Consequently, the electrolyte potential offsets the cell equilibrium potential and deviates the output voltage rapidly down to end-of-discharge condition (2.5 V), notably limiting attainable capacity at 24 mAh g^{-1} (**Figure 4.17a**). In sharp contrast, the cell with the higher t_{Li}^+ (0.74) alleviates the concentration polarization, which is evidenced by the less concentrated concentration at anode (1.5M) and less diluted concentration at cathode (0.1M) by the end of discharge. The discharging of the cell lasts 93 seconds, which correspond to an enhanced deliverable capacity of 80 mAh g^{-1} at 20C (**Figure 4.17b**). Taking the same discharge time (27 seconds) for comparison, the cell with the higher t_{Li}^+ still maintains a higher electrolyte concentration of 0.4M and a smaller electrolyte potential drop of -0.57 V at cathode side (**Figure 4.16d**). Therefore, the biomimetic Li$^+$ channel with high t_{Li}^+ and improved Li$^+$ transport efficiency effectively prevents the electrolyte depletion at the electrode surface, mitigating concentration polarization and electrolyte potential drop particularly at high-rate operation.
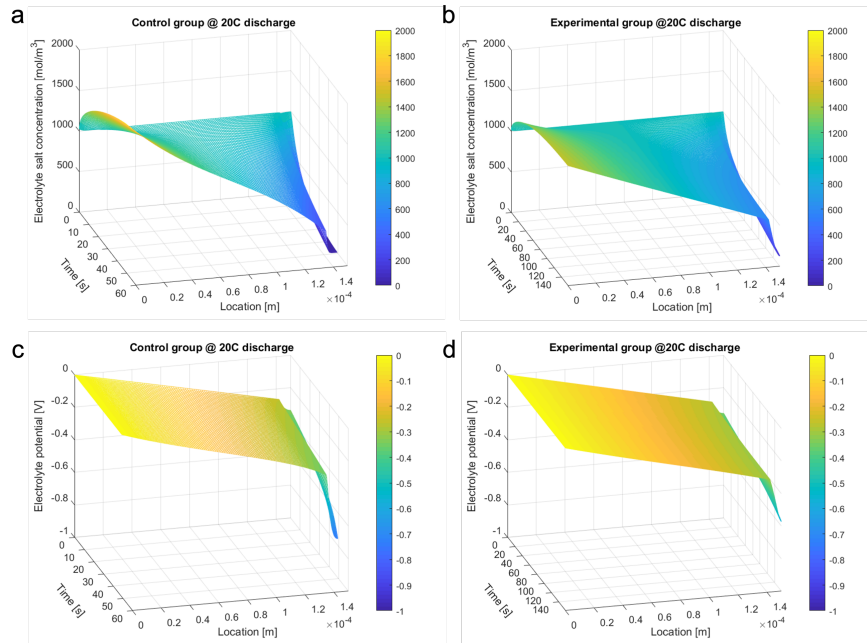
Figure 4.16 Electrolyte concentration distribution and electrolyte potential drop profiles simulated from conceptual LFP|Li cells.
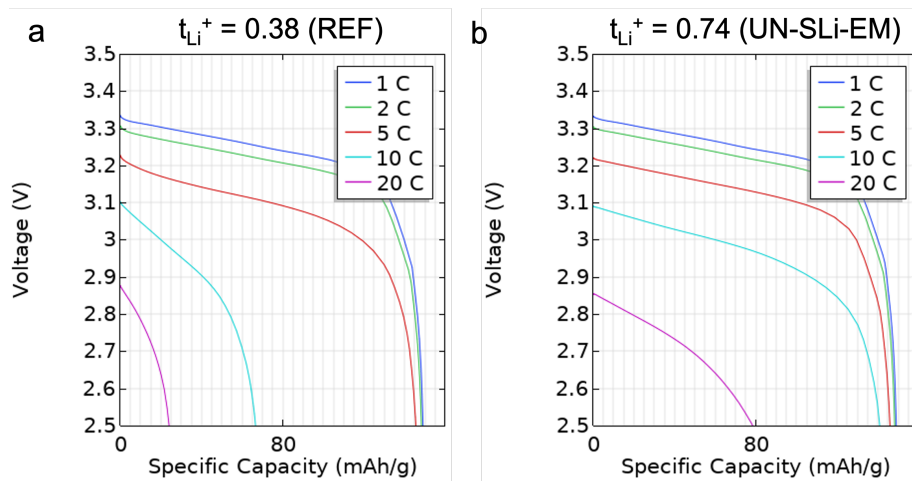
Figure 4.17 Output voltage profiles from simulated conceptual cell (LFP|Li) as a function of C-rate.

Table 4.3. List of parameters (adapted from COMSOL manual "1D Isothermal Lithium-Ion Battery")[1-2]

Parameter	Value [Unit]	Meaning
i_1C	3 [A m^{-2}]	1C discharge current
C	1	Discharge rate
t_plus	0.38	Li-ion transference number (in non-separator region)
sigma_f	1	Scaling factor for electrolyte ionic conductivity (in non-separator region)
t_plus_SEP	0.38	Li-ion transference number (in separator region)
sigma_f_SEP	0.36	Scaling factor for electrolyte ionic conductivity (in separator region)
cl_0	1000[mol m^{-3}]	Initial electrolyte salt concentration
c_ref	1000[mol m^{-3}]	Reference electrolyte salt concentration for ionic conductivity interpolation
L_sep	140e-6[m]	Length of separator
L_pos	10e-6[m]	Length of positive electrode
T	298[K]	Temperature
rp_pos	2e-6[m]	Particle radius positive electrode
epsl_pos	0.63	Electrolyte phase volume fraction, positive electrode
epss_filler_pos	0.073	Conductive filler phase volume fraction, positive electrode
epss_pos	1-epsl_pos-epss_filler_pos	Electrode phase volume fraction, positive electrode
epss_neg	1-epsl_neg-epss_filler_neg	Solid phase vol-fraction negative electrode
csmax_neg	26390[mol m^{-3}]	Max solid phase concentration negative electrode
cs0_neg	26000[mol m^{-3}]	Initial concentration negative active electrode material
cs0_pos	3900[mol m^{-3}]	Initial concentration positive active electrode material
Ks_neg	100[S m^{-1}]	Solid phase conductivity negative electrode
k_pos	4.8e-10[m s^{-1}]	Reaction rate coefficient positive electrode
brugg	3.3	Bruggeman coefficient

4.4 Conclusions

In summary, we have demonstrated an electrolyte membrane for the selective transport of lithium ions through grafting the nanoporous channels of MOFs with sulfonate groups. This design

mimics ion channels in biological systems, electrostatically repelling anions while allowing passage of Li^+ with a high t_{Li^+}, which significantly improves the rate performance and prolongs the cycling life of lithium-ion batteries. Furthermore, this biomimetic strategy could be extended to develop various ion-conducting materials with desired selectivity.

REFERENCES:

(1)   Ritchie, H.; Roser, M. CO₂ and Greenhouse Gas Emissions - Our World in Data. *Our World in Data* **2017**.

(2)   Clean Energy Investment Exceeded $300 Billion Once Again in 2018 | BloombergNEF https://about.bnef.com/blog/clean-energy-investment-exceeded-300-billion-2018/ (accessed Mar 4, 2020).

(3)   Renewable energy: getting to 100% requires cheap energy storage. But how cheap? - Vox https://www.vox.com/energy-and-environment/2019/8/9/20767886/renewable-energy-storage-cost-electricity (accessed Mar 4, 2020).

(4)   Aneke, M.; Wang, M. Energy Storage Technologies and Real Life Applications – A State of the Art Review. *Appl. Energy* **2016**, *179*, 350–377.

(5)   Díaz-González, F.; Sumper, A.; Gomis-Bellmunt, O.; Villafáfila-Robles, R. A Review of Energy Storage Technologies for Wind Power Applications. *Renewable and Sustainable Energy Reviews* **2012**, *16*, 2154–2171.

(6)   Electricity generation - Wikipedia https://en.wikipedia.org/wiki/Electricity_generation (accessed Mar 5, 2020).

(7)   Energy Storage Systems Market Size, Share | Industry Report 2019-2026 https://www.grandviewresearch.com/industry-analysis/energy-storage-systems-market (accessed Mar 5, 2020).

(8)   *Energy Storage Systems - Volume I*; Gogus, Y., Ed.; EOLSS Publications, 2009.

(9)   Yang, Z.; Zhang, J.; Kintner-Meyer, M. C. W.; Lu, X.; Choi, D.; Lemmon, J. P.; Liu, J.

Electrochemical Energy Storage for Green Grid. *Chem. Rev.* **2011**, *111*, 3577–3613.

(10)   McLaren, J.; Miller, J.; O'Shaughnessy, E.; Wood, E.; Shapiro, E. *Emissions Associated with Electric Vehicle Charging: Impact of Electricity Generation Mix, Charging Infrastructure Availability, and Vehicle Type*; National Renewable Energy Laboratory (NREL): Golden, CO (United States), 2016.

(11)   Elgowainy, A.; Han, J.; Poch, L.; Wang, M.; Vyas, A.; Mahalik, M.; Rousseau, A. *Well-to-Wheels Analysis of Energy Use and Greenhouse Gas Emissions of Plug-in Hybrid Electric Vehicles.*; Argonne National Laboratory (ANL): Argonne, IL (United States), 2010.

(12)   Larcher, D.; Tarascon, J. M. Towards Greener and More Sustainable Batteries for Electrical Energy Storage. *Nat. Chem.* **2015**, *7*, 19–29.

(13)   Smartphone battery life: iPhone XS battery isn't as good as the X. Which phone outlasts them all? - The Washington Post https://www.washingtonpost.com/technology/2018/11/01/its-not-your-imagination-phone-battery-life-is-getting-worse/ (accessed Mar 4, 2020).

(14)   SAFETY, G. Models: See Specific Products Listed in This Document under Apple Product Battery Information,.

(15)   Prifti, H.; Parasuraman, A.; Winardi, S.; Lim, T. M.; Skyllas-Kazacos, M. Membranes for Redox Flow Battery Applications. *Membranes (Basel)* **2012**, *2*, 275–306.

(16)   Lu, X.; Xia, G.; Lemmon, J. P.; Yang, Z. Advanced Materials for Sodium-Beta Alumina Batteries: Status, Challenges and Perspectives. *J. Power Sources* **2010**, *195*, 2431–2442.

(17)   Hueso, K. B.; Armand, M.; Rojo, T. High Temperature Sodium Batteries: Status, Challenges and Future Trends. *Energy Environ. Sci.* **2013**, *6*, 734.

(18)   Pavlov, D. *Lead-Acid Batteries: Science and Technology*; Elsevier, 2011.

(19)   Winter, M.; Barnett, B.; Xu, K. Before Li Ion Batteries. *Chem. Rev.* **2018**, *118*, 11433–11456.

(20)   Goodenough, J. B. How We Made the Li-Ion Rechargeable Battery. *Nat. Electron.* **2018**, *1*, 204–204.

(21)   Xu, J.; Dou, S.; Liu, H.; Dai, L. Cathode Materials for next Generation Lithium Ion Batteries. *Nano Energy* **2013**, *2*, 439–442.

(22)   Zhang, W.-J. Structure and Performance of LiFePO4 Cathode Materials: A Review. *J. Power Sources* **2011**, *196*, 2962–2970.

(23)   Zheng, J.; Ye, Y.; Pan, F. 'Structure Units' as Materials Genes in Cathode Materials for Lithium-Ion Batteries. *Natl Sci Rev* **2019**.

(24)   Zhan, C.; Wu, T.; Lu, J.; Amine, K. Dissolution, Migration, and Deposition of Transition Metal Ions in Li-Ion Batteries Exemplified by Mn-Based Cathodes – a Critical Review. *Energy Environ. Sci.* **2018**, *11*, 243–257.

(25)   Dou, S. Review and Prospects of Mn-Based Spinel Compounds as Cathode Materials for Lithium-Ion Batteries. *Ionics (Kiel)* **2015**, *21*, 3001–3030.

(26)   Lu, J.; Lee, K. S. Spinel Cathodes for Advanced Lithium Ion Batteries: A Review of Challenges and Recent Progress. *Materials Technology* **2016**, *31*, 628–641.

(27)   Myung, S.-T.; Maglia, F.; Park, K.-J.; Yoon, C. S.; Lamp, P.; Kim, S.-J.; Sun, Y.-K.

Nickel-Rich Layered Cathode Materials for Automotive Lithium-Ion Batteries: Achievements and Perspectives. *ACS Energy Lett.* **2017**, *2*, 196–223.

(28)   Xu, J.; Lin, F.; Doeff, M. M.; Tong, W. A Review of Ni-Based Layered Oxides for Rechargeable Li-Ion Batteries. *J. Mater. Chem. A* **2017**, *5*, 874–901.

(29)   Yan, J.; Liu, X.; Li, B. Recent Progress in Li-Rich Layered Oxides as Cathode Materials for Li-Ion Batteries. *RSC Adv.* **2014**, *4*, 63268–63284.

(30)   Li, W.; Erickson, E. M.; Manthiram, A. High-Nickel Layered Oxide Cathodes for Lithium-Based Automotive Batteries. *Nat. Energy* **2020**, *5*, 26–34.

(31)   Myung, S.-T.; Izumi, K.; Komaba, S.; Sun, Y.-K.; Yashiro, H.; Kumagai, N. Role of Alumina Coating on Li−Ni−Co−Mn−O Particles as Positive Electrode Material for Lithium-Ion Batteries. *Chem. Mater.* **2005**, *17*, 3695–3704.

(32)   US20130313485A1 - METHOD OF FABRICATING LiFePO4 CATHODE ELECTROACTIVE MATERIAL BY RECYCLING, AND LiFePO4 CATHODE ELECTROACTIVE MATERIAL, LiFePO4 CATHODE, AND LITHIUM SECONDARY BATTERY FABRICATED THEREBY - Google Patents https://patents.google.com/patent/US20130313485A1/en (accessed Mar 7, 2020).

(33)   POLYCRYSTALLINE LAYERED METAL OXIDES COMPRISING NANO-CRYSTALS - CAMX POWER, LLC. http://www.freepatentsonline.com/y2019/0140276.html (accessed Mar 6, 2020).

(34)   Dawson, J. A.; Canepa, P.; Famprikis, T.; Masquelier, C.; Islam, M. S. Atomic-Scale Influence of Grain Boundaries on Li-Ion Conduction in Solid Electrolytes for All-Solid-

State Batteries. *J. Am. Chem. Soc.* **2017**, *140*, 362–368.

(35)   Shi, Y.; Zhou, X.; Yu, G. Material and Structural Design of Novel Binder Systems for

High-Energy, High-Power Lithium-Ion Batteries. *Acc. Chem. Res.* **2017**, *50*, 2642–2652.

(36)   US20180159128A1 - Nickel-based active material for lithium secondary battery, method

of preparing the same, and lithium secondary battery including positive electrode

including the nickel-based active material - Google Patents

https://patents.google.com/patent/US20180159128A1/en (accessed Mar 7, 2020).

(37)   Kimijima, T.; Zettsu, N.; Teshima, K. Growth Manner of Octahedral-Shaped $Li(Ni_{1/3}$

$Co_{1/3} Mn_{1/3})O_2$ Single Crystals in Molten $Na_2 SO_4$. *Cryst. Growth Des.* **2016**, *16*, 2618–

2623.

(38)   US20140356719A1 - Electrode active material for lithium secondary battery - Google

Patents https://patents.google.com/patent/US20140356719A1/en (accessed Mar 7,

2020).

(39)   Kokalj, A.; Dominko, R.; Mali, G.; Meden, A.; Gaberscek, M.; Jamnik, J. Beyond One-

Electron Reaction in Li Cathode Materials: Designing $Li_2 Mn$ $Fe_1 -$

SiO_4. *Chem. Mater.* **2007**, *19*, 3633–3640.

(40)   Tarascon, J. M.; Armand, M. Issues and Challenges Facing Rechargeable Lithium

Batteries. *Nature* **2001**, *414*, 359–367.

(41)   Liu, Y.; Zhu, Y.; Cui, Y. Challenges and Opportunities towards Fast-Charging Battery

Materials. *Nat. Energy* **2019**.

(42)   Kwade, A.; Haselrieder, W.; Leithoff, R.; Modlinger, A.; Dietrich, F.; Droeder, K.

Current Status and Challenges for Automotive Battery Production Technologies. *Nat. Energy* **2018**, *3*, 290–300.

(43)   Schmuch, R.; Wagner, R.; Hörpel, G.; Placke, T.; Winter, M. Performance and Cost of Materials for Lithium-Based Rechargeable Automotive Batteries. *Nat. Energy* **2018**, *3*, 267–278.

(44)   Lu, J.; Chen, Z.; Pan, F.; Cui, Y.; Amine, K. High-Performance Anode Materials for Rechargeable Lithium-Ion Batteries. *Electrochem. Energ. Rev.* **2018**, *1*, 35–53.

(45)   Xu, Z.-L.; Liu, X.; Luo, Y.; Zhou, L.; Kim, J.-K. Nanosilicon Anodes for High Performance Rechargeable Batteries. *Prog. Mater. Sci.* **2017**, *90*, 1–44.

(46)   Nitta, N.; Wu, F.; Lee, J. T.; Yushin, G. Li-Ion Battery Materials: Present and Future. *Materials Today* **2015**, *18*, 252–264.

(47)   Li, M.; Lu, J.; Chen, Z.; Amine, K. 30 Years of Lithium-Ion Batteries. *Adv. Mater. Weinheim* **2018**, e1800561.

(48)   Aravindan, V.; Lee, Y.-S.; Madhavi, S. Best Practices for Mitigating Irreversible Capacity Loss of Negative Electrodes in Li-Ion Batteries. *Adv. Energy Mater.* **2017**, *7*, 1602607.

(49)   Andre, D.; Hain, H.; Lamp, P.; Maglia, F.; Stiaszny, B. Future High-Energy Density Anode Materials from an Automotive Application Perspective. *J. Mater. Chem. A* **2017**, *5*, 17174–17198.

(50)   Pietsch, P.; Westhoff, D.; Feinauer, J.; Eller, J.; Marone, F.; Stampanoni, M.; Schmidt, V.; Wood, V. Quantifying Microstructural Dynamics and Electrochemical Activity of

Graphite and Silicon-Graphite Lithium Ion Battery Anodes. *Nat. Commun.* **2016**, *7*, 12909.

(51)   Billaud, J.; Bouville, F.; Magrini, T.; Villevieille, C.; Studart, A. R. Magnetically Aligned Graphite Electrodes for High-Rate Performance Li-Ion Batteries. *Nat. Energy* **2016**, *1*, 16097.

(52)   Yoshio, M.; Wang, H.; Fukuda, K.; Umeno, T.; Abeb, T.; Ogumib, Z. Improvement of Natural Graphite as a Lithium-Ion Battery Anode Material, from Raw Flake to Carbon-Coated Sphere{.

(53)   The World Market for Synthetic Graphite, 2019 to 2024 - Top 5 Players Account for More Than 75% of the Market Share https://finance.yahoo.com/news/world-market-synthetic-graphite-2019-081147510.html?guccounter=1&guce_referrer=aHR0cHM6Ly93d3cuZ29vZ2xlLmNvbS8&guce_referrer_sig=AQAAAG_2dYw8M6hT6X7aswJrnQ2lOxPAd2Iukd1rvHvBLu7iLx-dIyY4whBEWj8IYv0l9O0NBjBuAYN5MVjxiSoKOpVHBikQ6mC3q7PaPWHOU8F-h4P4hZlF9sAeco-Kj6urlvG4wVvpfzo7P_H9y-F7iGESk7M1SUQNYkM_X9GKwNMK (accessed Mar 11, 2020).

(54)   Azuma, H.; Imoto, H.; Yamada, S.; Sekai, K. Advanced Carbon Anode Materials for Lithium Ion Cells. *J. Power Sources* **1999**, *81–82*, 1–7.

(55)   Cai, Y.; Fan, C. Influences of Conductive Additives on Electrochemical Performances of Artificial Graphite Anode with Different Shapes for Lithium Ion Batteries. *Electrochim. Acta* **2011**, *58*, 481–487.

(56)   Zheng, H.; Qu, Q.; Zhang, L.; Liu, G.; Battaglia, V. S. Hard Carbon: A Promising

Lithium-Ion Battery Anode for High Temperature Applications with Ionic Electrolyte.

RSC Adv. **2012**, *2*, 4904.

(57)   Fan, L.; Liu, Q.; Chen, S.; Xu, Z.; Lu, B. Soft Carbon as Anode for High-Performance

Sodium-Based Dual Ion Full Battery. *Adv. Energy Mater.* **2017**, *7*, 1602778.

(58)   Cao, B.; Liu, H.; Xu, B.; Lei, Y.; Chen, X.; Song, H. Mesoporous Soft Carbon as an

Anode Material for Sodium Ion Batteries with Superior Rate and Cycling Performance.

J. Mater. Chem. A **2016**, *4*, 6472–6478.

(59)   Zheng, Y.; Wang, Y.; Lu, Y.; Hu, Y.-S.; Li, J. A High-Performance Sodium-Ion Battery

Enhanced by Macadamia Shell Derived Hard Carbon Anode. *Nano Energy* **2017**, *39*,

489–498.

(60)   Han, Y.-J.; Kim, J.; Yeo, J.-S.; An, J. C.; Hong, I.-P.; Nakabayashi, K.; Miyawaki, J.;

Jung, J.-D.; Yoon, S.-H. Coating of Graphite Anode with Coal Tar Pitch as an Effective

Precursor for Enhancing the Rate Performance in Li-Ion Batteries: Effects of

Composition and Softening Points of Coal Tar Pitch. *Carbon N. Y.* **2015**, *94*, 432–438.

(61)   Ding, F.; Xu, W.; Choi, D.; Wang, W.; Li, X.; Engelhard, M. H.; Chen, X.; Yang, Z.;

Zhang, J.-G. Enhanced Performance of Graphite Anode Materials by AlF3 Coating for

Lithium-Ion Batteries. *J. Mater. Chem.* **2012**, *22*, 12745.

(62)   Han, H.; Park, H.; Kil, K. C.; Jeon, Y.; Ko, Y.; Lee, C.; Kim, M.; Cho, C.-W.; Kim, K.;

Paik, U.; *et al.* Microstructure Control of the Graphite Anode with a High Density for Li

Ion Batteries with High Energy Density. *Electrochim. Acta* **2015**, *166*, 367–371.

(63)   Chai, L.; Qu, Q.; Zhang, L.; Shen, M.; Zhang, L.; Zheng, H. Chitosan, a New and Environmental Benign Electrode Binder for Use with Graphite Anode in Lithium-Ion Batteries. *Electrochim. Acta* **2013**, *105*, 378–383.

(64)   Wang, H.; Umeno, T.; Mizuma, K.; Yoshio, M. Highly Conductive Bridges between Graphite Spheres to Improve the Cycle Performance of a Graphite Anode in Lithium-Ion Batteries. *J. Power Sources* **2008**, *175*, 886–890.

(65)   Chae, S.; Choi, S.-H.; Kim, N.; Sung, J.; Cho, J. Integration of Graphite and Silicon Anodes for the Commercialization of High-Energy Lithium-Ion Batteries. *Angew. Chem. Int. Ed. Engl.* **2019**.

(66)   Xu, Y.; Yi, R.; Yuan, B.; Wu, X.; Dunwell, M.; Lin, Q.; Fei, L.; Deng, S.; Andersen, P.; Wang, D.; *et al.* High Capacity MoO2/Graphite Oxide Composite Anode for Lithium-Ion Batteries. *J. Phys. Chem. Lett.* **2012**, *3*, 309–314.

(67)   Nobili, F.; Mancini, M.; Dsoke, S.; Tossici, R.; Marassi, R. Low-Temperature Behavior of Graphite–tin Composite Anodes for Li-Ion Batteries. *J. Power Sources* **2010**, *195*, 7090–7097.

(68)   Etacheri, V.; Marom, R.; Elazari, R.; Salitra, G.; Aurbach, D. Challenges in the Development of Advanced Li-Ion Batteries: A Review. *Energy Environ. Sci.* **2011**, *4*, 3243.

(69)   Sandhya, C. P.; John, B.; Gouri, C. Lithium Titanate as Anode Material for Lithium-Ion Cells: A Review. *Ionics (Kiel)* **2014**, *20*, 601–620.

(70)   Yi, T.-F.; Jiang, L.-J.; Shu, J.; Yue, C.-B.; Zhu, R.-S.; Qiao, H.-B. Recent Development

and Application of Li4Ti5O12 as Anode Material of Lithium Ion Battery. *Journal of Physics and Chemistry of Solids* **2010**, *71*, 1236–1242.

(71)   Chen, S.; Xin, Y.; Zhou, Y.; Ma, Y.; Zhou, H.; Qi, L. Self-Supported Li4Ti5O12 Nanosheet Arrays for Lithium Ion Batteries with Excellent Rate Capability and Ultralong Cycle Life. *Energy Environ. Sci.* **2014**, *7*, 1924.

(72)   Zhang, J.; Cai, Y.; Wu, J.; Yao, J. Graphene Oxide-Confined Synthesis of Li4Ti5O12 Microspheres as High-Performance Anodes for Lithium Ion Batteries. *Electrochim. Acta* **2015**, *165*, 422–429.

(73)   Li, Z.; Li, J.; Zhao, Y.; Yang, K.; Gao, F.; Li, X. Structure and Electrochemical Properties of Sm-Doped $Li_4 Ti_5 O_{12}$ as Anode Material for Lithium-Ion Batteries. *RSC Adv.* **2016**, *6*, 15492–15500.

(74)   Luo, G.; He, J.; Song, X.; Huang, X.; Yu, X.; Fang, Y.; Chen, D. Bamboo Carbon Assisted Sol–gel Synthesis of Li4Ti5O12 Anode Material with Enhanced Electrochemical Activity for Lithium Ion Battery. *J. Alloys Compd.* **2015**, *621*, 268–273.

(75)   Xu, G. B.; Li, W.; Yang, L. W.; Wei, X. L.; Ding, J. W.; Zhong, J. X.; Chu, P. K. Highly-Crystalline Ultrathin Li4Ti5O12 Nanosheets Decorated with Silver Nanocrystals as a High-Performance Anode Material for Lithium Ion Batteries. *J. Power Sources* **2015**, *276*, 247–254.

(76)   Mu, D.; Chen, Y.; Wu, B.; Huang, R.; Jiang, Y.; Li, L.; Wu, F. Nano-Sized Li4Ti5O12/C Anode Material with Ultrafast Charge/Discharge Capability for Lithium Ion Batteries. *J. Alloys Compd.* **2016**, *671*, 157–163.

(77)   Feng, K.; Li, M.; Liu, W.; Kashkooli, A. G.; Xiao, X.; Cai, M.; Chen, Z. Silicon-Based Anodes for Lithium-Ion Batteries: From Fundamentals to Practical Applications. *Small* **2018**, *14*.

(78)   Liu, D.; Liu, Z. J.; Li, X.; Xie, W.; Wang, Q.; Liu, Q.; Fu, Y.; He, D. Group IVA Element (Si, Ge, Sn)-Based Alloying/Dealloying Anodes as Negative Electrodes for Full-Cell Lithium-Ion Batteries. *Small* **2017**.

(79)   Huggins, R. A. Lithium Alloy Negative Electrodes. *J. Power Sources* **1999**, *81–82*, 13–19.

(80)   Wu, H.; Cui, Y. Designing Nanostructured Si Anodes for High Energy Lithium Ion Batteries. *Nano Today* **2012**, *7*, 414–429.

(81)   Silicon Anode Battery Market | Size, Share, system and Industry Analysis and Market Forecast to 2025 | MarketsandMarkets™ https://www.marketsandmarkets.com/Market-Reports/silicon-anode-battery-market-38224258.html (accessed Mar 12, 2020).

(82)   Li, J.; Dahn, J. R. An In Situ X-Ray Diffraction Study of the Reaction of Li with Crystalline Si. *J. Electrochem. Soc.* **2007**, *154*, A156.

(83)   Chan, M. K. Y.; Wolverton, C.; Greeley, J. P. First Principles Simulations of the Electrochemical Lithiation and Delithiation of Faceted Crystalline Silicon. *J. Am. Chem. Soc.* **2012**, *134*, 14362–14374.

(84)   Li, Y.; Zhang, K.; Zheng, B.; Zhang, X.; Wang, Q. Effects of Reversible Chemical Reaction on Li Diffusion and Stresses in Spherical Composition-Gradient Electrodes. *J. Appl. Phys.* **2015**, *117*, 245103.

(85)   Stolle, A.; Szuppa, T.; Leonhardt, S. E. S.; Ondruschka, B. Ball Milling in Organic

         Synthesis: Solutions and Challenges. *Chem. Soc. Rev.* **2011**, *40*, 2317–2329.

(86)   Zhu, B.; Jin, Y.; Tan, Y.; Zong, L.; Hu, Y.; Chen, L.; Chen, Y.; Zhang, Q.; Zhu, J.

         Scalable Production of Si Nanoparticles Directly from Low Grade Sources for Lithium-

         Ion Battery Anode. *Nano Lett.* **2015**, *15*, 5750–5754.

(87)   Shen, C.; Fang, X.; Ge, M.; Zhang, A.; Liu, Y.; Ma, Y.; Mecklenburg, M.; Nie, X.;

         Zhou, C. Hierarchical Carbon-Coated Ball-Milled Silicon: Synthesis and Applications in

         Free-Standing Electrodes and High-Voltage Full Lithium-Ion Batteries. *ACS Nano* **2018**,

         12, 6280–6291.

(88)   Song, T.; Hu, L.; Paik, U. One-Dimensional Silicon Nanostructures for Li Ion Batteries.

         J. Phys. Chem. Lett. **2014**, *5*, 720–731.

(89)   Peng, K.-Q.; Wang, X.; Li, L.; Hu, Y.; Lee, S.-T. Silicon Nanowires for Advanced

         Energy Conversion and Storage. *Nano Today* **2013**, *8*, 75–97.

(90)   Su, X.; Wu, Q.; Li, J.; Xiao, X.; Lott, A.; Lu, W.; Sheldon, B. W.; Wu, J. Silicon-Based

         Nanomaterials for Lithium-Ion Batteries: A Review. *Adv. Energy Mater.* **2014**, *4*,

         1300882.

(91)   Chan, C. K.; Peng, H.; Liu, G.; McIlwrath, K.; Zhang, X. F.; Huggins, R. A.; Cui, Y.

         High-Performance Lithium Battery Anodes Using Silicon Nanowires. *Nat. Nanotechnol.*

         2008, *3*, 31–35.

(92)   McSweeney, W.; Geaney, H.; O'Dwyer, C. Metal-Assisted Chemical Etching of Silicon

         and the Behavior of Nanoscale Silicon Materials as Li-Ion Battery Anodes. *Nano Res.*

2015, *8*, 1395–1442.

(93)   Ge, M.; Rong, J.; Fang, X.; Zhang, A.; Lu, Y.; Zhou, C. Scalable Preparation of Porous

Silicon Nanoparticles and Their Application for Lithium-Ion Battery Anodes. *Nano Res.*

2013, *6*, 174–181.

(94)   Jia, H.; Gao, P.; Yang, J.; Wang, J.; Nuli, Y.; Yang, Z. Novel Three-Dimensional

Mesoporous Silicon for High Power Lithium-Ion Battery Anode Material. *Adv. Energy*

Mater. **2011**, *1*, 1036–1039.

(95)   Yoo, J.-K.; Kim, J.; Choi, M.-J.; Park, Y.-U.; Hong, J.; Baek, K. M.; Kang, K.; Jung, Y.

S. Extremely High Yield Conversion from Low-Cost Sand to High-Capacity Si

Electrodes for Li-Ion Batteries. *Adv. Energy Mater.* **2014**, *4*, 1400622.

(96)   Zhang, L.; Liu, X.; Zhao, Q.; Dou, S.; Liu, H.; Huang, Y.; Hu, X. Si-Containing

Precursors for Si-Based Anode Materials of Li-Ion Batteries: A Review. *Energy Storage*

Materials **2016**, *4*, 92–102.

(97)   Liu, N.; Wu, H.; McDowell, M. T.; Yao, Y.; Wang, C.; Cui, Y. A Yolk-Shell Design for

Stabilized and Scalable Li-Ion Battery Alloy Anodes. *Nano Lett.* **2012**, *12*, 3315–3321.

(98)   Wu, H.; Zheng, G.; Liu, N.; Carney, T. J.; Yang, Y.; Cui, Y. Engineering Empty Space

between Si Nanoparticles for Lithium-Ion Battery Anodes. *Nano Lett.* **2012**, *12*, 904–

909.

(99)   Liu, N.; Lu, Z.; Zhao, J.; McDowell, M. T.; Lee, H.-W.; Zhao, W.; Cui, Y. A

Pomegranate-Inspired Nanoscale Design for Large-Volume-Change Lithium Battery

Anodes. *Nat. Nanotechnol.* **2014**, *9*, 187–192.

(100)   Li, Y.; Yan, K.; Lee, H.-W.; Lu, Z.; Liu, N.; Cui, Y. Growth of Conformal Graphene
        Cages on Micrometre-Sized Silicon Particles as Stable Battery Anodes. *Nat. Energy*
        2016, *1*, 15029.

(101)   Jin, Y.; Li, S.; Kushima, A.; Zheng, X.; Sun, Y.; Xie, J.; Sun, J.; Xue, W.; Zhou, G.; Wu,
        J.; *et al.* Self-Healing SEI Enables Full-Cell Cycling of a Silicon-Majority Anode with a
        Coulombic Efficiency Exceeding 99.9%. *Energy Environ. Sci.* **2017**, *10*, 580–592.

(102)   Yang, J.; Wang, Y.; Li, W.; Wang, L.; Fan, Y.; Jiang, W.; Luo, W.; Wang, Y.; Kong, B.;
        Selomulya, C.; *et al.* Amorphous TiO2 Shells: A Vital Elastic Buffering Layer on
        Silicon Nanoparticles for High-Performance and Safe Lithium Storage. *Adv. Mater.*
        Weinheim **2017**, *29*.

(103)   Wu, H.; Yu, G.; Pan, L.; Liu, N.; McDowell, M. T.; Bao, Z.; Cui, Y. Stable Li-Ion
        Battery Anodes by in-Situ Polymerization of Conducting Hydrogel to Conformally Coat
        Silicon Nanoparticles. *Nat. Commun.* **2013**, *4*, 1943.

(104)   Wang, C.; Wu, H.; Chen, Z.; McDowell, M. T.; Cui, Y.; Bao, Z. Self-Healing Chemistry
        Enables the Stable Operation of Silicon Microparticle Anodes for High-Energy Lithium-
        Ion Batteries. *Nat. Chem.* **2013**, *5*, 1042–1048.

(105)   Zhao, H.; Wei, Y.; Qiao, R.; Zhu, C.; Zheng, Z.; Ling, M.; Jia, Z.; Bai, Y.; Fu, Y.; Lei,
        J.; *et al.* Conductive Polymer Binder for High-Tap-Density Nanosilicon Material for
        Lithium-Ion Battery Negative Electrode Application. *Nano Lett.* **2015**, *15*, 7927–7932.

(106)   Liu, N.; Hu, L.; McDowell, M. T.; Jackson, A.; Cui, Y. Prelithiated Silicon Nanowires
        as an Anode for Lithium Ion Batteries. *ACS Nano* **2011**, *5*, 6487–6493.

(107)   Forney, M. W.; Ganter, M. J.; Staub, J. W.; Ridgley, R. D.; Landi, B. J. Prelithiation of Silicon-Carbon Nanotube Anodes for Lithium Ion Batteries by Stabilized Lithium Metal Powder (SLMP). *Nano Lett.* **2013**, *13*, 4158–4163.

(108)   Zhao, J.; Lu, Z.; Liu, N.; Lee, H.-W.; McDowell, M. T.; Cui, Y. Dry-Air-Stable Lithium Silicide-Lithium Oxide Core-Shell Nanoparticles as High-Capacity Prelithiation Reagents. *Nat. Commun.* **2014**, *5*, 5088.

(109)   Wang, B.; Ryu, J.; Choi, S.; Zhang, X.; Pribat, D.; Li, X.; Zhi, L.; Park, S.; Ruoff, R. S. Ultrafast-Charging Silicon-Based Coral-Like Network Anodes for Lithium-Ion Batteries with High Energy and Power Densities. *ACS Nano* **2019**, *13*, 2307–2315.

(110)   An, W.; Gao, B.; Mei, S.; Xiang, B.; Fu, J.; Wang, L.; Zhang, Q.; Chu, P. K.; Huo, K. Scalable Synthesis of Ant-Nest-like Bulk Porous Silicon for High-Performance Lithium-Ion Battery Anodes. *Nat. Commun.* **2019**, *10*, 1447.

(111)   Chen, S.; Chen, Z.; Xu, X.; Cao, C.; Xia, M.; Luo, Y. Scalable 2D Mesoporous Silicon Nanosheets for High-Performance Lithium-Ion Battery Anode. *Small* **2018**, *14*.

(112)   Ko, M.; Chae, S.; Ma, J.; Kim, N.; Lee, H.-W.; Cui, Y.; Cho, J. Scalable Synthesis of Silicon-Nanolayer-Embedded Graphite for High-Energy Lithium-Ion Batteries. *Nat. Energy* **2016**, *1*, 16113.

(113)   Ma, J.; Sung, J.; Hong, J.; Chae, S.; Kim, N.; Choi, S.-H.; Nam, G.; Son, Y.; Kim, S. Y.; Ko, M.; *et al.* Towards Maximized Volumetric Capacity via Pore-Coordinated Design for Large-Volume-Change Lithium-Ion Battery Anodes. *Nat. Commun.* **2019**, *10*, 475.

(114)   Park, J.-B.; Ham, J.-S.; Shin, M.-S.; Park, H.-K.; Lee, Y.-J.; Lee, S.-M. Synthesis and

Electrochemical Characterization of Anode Material with Titanium–silicon Alloy Solid Core/Nanoporous Silicon Shell Structures for Lithium Rechargeable Batteries. *J. Power Sources* **2015**, *299*, 537–543.

(115)   Global Next-generation Anode Materials Market Anticipated to Reach $6.28 Billion by 2029 - Bloomberg https://www.bloomberg.com/press-releases/2019-06-25/global-next-generation-anode-materials-market-anticipated-to-reach-6-28-billion-by-2029 (accessed Mar 20, 2020).

(116)   Liu, Z.; Yu, Q.; Zhao, Y.; He, R.; Xu, M.; Feng, S.; Li, S.; Zhou, L.; Mai, L. Silicon Oxides: A Promising Family of Anode Materials for Lithium-Ion Batteries. *Chem. Soc. Rev.* **2019**, *48*, 285–309.

(117)   Seong, I. W.; Kim, K. T.; Yoon, W. Y. Electrochemical Behavior of a Lithium-Pre-Doped Carbon-Coated Silicon Monoxide Anode Cell. *J. Power Sources* **2009**, *189*, 511–514.

(118)   Seong, I. W.; Yoon, W. Y. Electrochemical Behavior of a Silicon Monoxide and Li-Powder Double Layer Anode Cell. *J. Power Sources* **2010**, *195*, 6143–6147.

(119)   Kim, H. J.; Choi, S.; Lee, S. J.; Seo, M. W.; Lee, J. G.; Deniz, E.; Lee, Y. J.; Kim, E. K.; Choi, J. W. Controlled Prelithiation of Silicon Monoxide for High Performance Lithium-Ion Rechargeable Full Cells. *Nano Lett.* **2016**, *16*, 282–288.

(120)   Yang, X.; Wen, Z.; Xu, X.; Lin, B.; Huang, S. Nanosized Silicon-Based Composite Derived by in Situ Mechanochemical Reduction for Lithium Ion Batteries. *J. Power Sources* **2007**, *164*, 880–884.

(121)   Yom, J. H.; Hwang, S. W.; Cho, S. M.; Yoon, W. Y. Improvement of Irreversible

         Behavior of SiO Anodes for Lithium Ion Batteries by a Solid State Reaction at High

         Temperature. *J. Power Sources* **2016**, *311*, 159–166.

(122)   Yu, B.-C.; Hwa, Y.; Kim, J.-H.; Sohn, H.-J. A New Approach to Synthesis of Porous

         SiOx Anode for Li-Ion Batteries via Chemical Etching of Si Crystallites. *Electrochim.*

         Acta **2014**, *117*, 426–430.

(123)   Li-ion Batteries 2018-2028: IDTechEx https://www.idtechex.com/en/research-report/li-

         ion-batteries-2018-2028/557 (accessed Mar 21, 2020).

(124)   Yang, C.; Fu, K.; Zhang, Y.; Hitz, E.; Hu, L. Protected Lithium-Metal Anodes in

         Batteries: From Liquid to Solid. *Adv. Mater. Weinheim* **2017**, *29*.

(125)   Cheng, X.-B.; Zhang, R.; Zhao, C.-Z.; Zhang, Q. Toward Safe Lithium Metal Anode in

         Rechargeable Batteries: A Review. *Chem. Rev.* **2017**, *117*, 10403–10473.

(126)   Albertus, P.; Babinec, S.; Litzelman, S.; Newman, A. Status and Challenges in Enabling

         the Lithium Metal Electrode for High-Energy and Low-Cost Rechargeable Batteries.

         Nat. Energy **2017**.

(127)   Lin, D.; Liu, Y.; Cui, Y. Reviving the Lithium Metal Anode for High-Energy Batteries.

         Nat. Nanotechnol. **2017**, *12*, 194–206.

(128)   Li, Y.; Huang, W.; Li, Y.; Pei, A.; Boyle, D. T.; Cui, Y. Correlating Structure and

         Function of Battery Interphases at Atomic Resolution Using Cryoelectron Microscopy.

         Joule **2018**, *2*, 2167–2177.

(129)   Parimalam, B. S.; MacIntosh, A. D.; Kadam, R.; Lucht, B. L. Decomposition Reactions

of Anode Solid Electrolyte Interphase (SEI) Components with LiPF$_6$. *J. Phys. Chem. C* **2017**, *121*, 22733–22738.

(130) Cheng, X.-B.; Zhang, R.; Zhao, C.-Z.; Wei, F.; Zhang, J.-G.; Zhang, Q. A Review of Solid Electrolyte Interphases on Lithium Metal Anode. *Adv Sci (Weinh)* **2016**, *3*, 1500213.

(131) Yan, C.; Cheng, X.-B.; Tian, Y.; Chen, X.; Zhang, X.-Q.; Li, W.-J.; Huang, J.-Q.; Zhang, Q. Dual-Layered Film Protected Lithium Metal Anode to Enable Dendrite-Free Lithium Deposition. *Adv. Mater. Weinheim* **2018**, *30*, e1707629.

(132) Lang, J.; Long, Y.; Qu, J.; Luo, X.; Wei, H.; Huang, K.; Zhang, H.; Qi, L.; Zhang, Q.; Li, Z.; *et al.* One-Pot Solution Coating of High Quality LiF Layer to Stabilize Li Metal Anode. *Energy Storage Materials* **2019**, *16*, 85–90.

(133) Zhu, J.; Li, P.; Chen, X.; Legut, D.; Fan, Y.; Zhang, R.; Lu, Y.; Cheng, X.; Zhang, Q. Rational Design of Graphitic-Inorganic Bi-Layer Artificial SEI for Stable Lithium Metal Anode. *Energy Storage Materials* **2019**, *16*, 426–433.

(134) Tikekar, M. D.; Choudhury, S.; Tu, Z.; Archer, L. A. Design Principles for Electrolytes and Interfaces for Stable Lithium-Metal Batteries. *Nat. Energy* **2016**, *1*, 16114.

(135) Gao, Y.; Yan, Z.; Gray, J. L.; He, X.; Wang, D.; Chen, T.; Huang, Q.; Li, Y. C.; Wang, H.; Kim, S. H.; *et al.* Polymer-Inorganic Solid-Electrolyte Interphase for Stable Lithium Metal Batteries under Lean Electrolyte Conditions. *Nat. Mater.* **2019**, *18*, 384–389.

(136) Liu, Y.; Lin, D.; Yuen, P. Y.; Liu, K.; Xie, J.; Dauskardt, R. H.; Cui, Y. An Artificial Solid Electrolyte Interphase with High Li-Ion Conductivity, Mechanical Strength, and

Flexibility for Stable Lithium Metal Anodes. *Adv. Mater. Weinheim* **2017**, *29*.

(137)   Zhang, Y.; Luo, W.; Wang, C.; Li, Y.; Chen, C.; Song, J.; Dai, J.; Hitz, E. M.; Xu, S.; Yang, C.; *et al.* High-Capacity, Low-Tortuosity, and Channel-Guided Lithium Metal Anode. *Proc. Natl. Acad. Sci. USA* **2017**, *114*, 3584–3589.

(138)   Liang, Z.; Lin, D.; Zhao, J.; Lu, Z.; Liu, Y.; Liu, C.; Lu, Y.; Wang, H.; Yan, K.; Tao, X.; *et al.* Composite Lithium Metal Anode by Melt Infusion of Lithium into a 3D Conducting Scaffold with Lithiophilic Coating. *Proc. Natl. Acad. Sci. USA* **2016**, *113*, 2862–2867.

(139)   Liu, Y.; Lin, D.; Liang, Z.; Zhao, J.; Yan, K.; Cui, Y. Lithium-Coated Polymeric Matrix as a Minimum Volume-Change and Dendrite-Free Lithium Metal Anode. *Nat. Commun.* **2016**, *7*, 10992.

(140)   Lin, D.; Liu, Y.; Liang, Z.; Lee, H.-W.; Sun, J.; Wang, H.; Yan, K.; Xie, J.; Cui, Y. Layered Reduced Graphene Oxide with Nanoscale Interlayer Gaps as a Stable Host for Lithium Metal Anodes. *Nat. Nanotechnol.* **2016**, *11*, 626–632.

(141)   Xue, P.; Liu, S.; Shi, X.; Sun, C.; Lai, C.; Zhou, Y.; Sui, D.; Chen, Y.; Liang, J. A Hierarchical Silver-Nanowire-Graphene Host Enabling Ultrahigh Rates and Superior Long-Term Cycling of Lithium-Metal Composite Anodes. *Adv. Mater. Weinheim* **2018**, *30*, e1804165.

(142)   Xu, K. Nonaqueous Liquid Electrolytes for Lithium-Based Rechargeable Batteries. *Chem. Rev.* **2004**, *104*, 4303–4417.

(143)   Zhang, S. S.; Jow, T. R.; Amine, K.; Henriksen, G. L. LiPF6–EC–EMC Electrolyte for

Li-Ion Battery. *J. Power Sources* **2002**, *107*, 18–23.

(144)   Tesla fire kills man because door handles wouldn't open, lawsuit alleges - The
        Washington Post https://www.washingtonpost.com/business/2019/10/23/man-died-
        burning-tesla-because-its-futuristic-doors-wouldnt-open-lawsuit-alleges/ (accessed Mar
        30, 2020).

(145)   Wagner, R.; Korth, M.; Streipert, B.; Kasnatscheew, J.; Gallus, D. R.; Brox, S.;
        Amereller, M.; Cekic-Laskovic, I.; Winter, M. Impact of Selected LiPF6 Hydrolysis
        Products on the High Voltage Stability of Lithium-Ion Battery Cells. *ACS Appl. Mater.
        Interfaces* **2016**, *8*, 30871–30878.

(146)   Aurbach, D.; Talyosef, Y.; Markovsky, B.; Markevich, E.; Zinigrad, E.; Asraf, L.;
        Gnanaraj, J. S.; Kim, H.-J. Design of Electrolyte Solutions for Li and Li-Ion Batteries: A
        Review. *Electrochim. Acta* **2004**, *50*, 247–254.

(147)   Zheng, J.; Engelhard, M. H.; Mei, D.; Jiao, S.; Polzin, B. J.; Zhang, J.-G.; Xu, W.
        Electrolyte Additive Enabled Fast Charging and Stable Cycling Lithium Metal Batteries.
        Nat. Energy **2017**, *2*, 17012.

(148)   Marcinek, M.; Syzdek, J.; Marczewski, M.; Piszcz, M.; Niedzicki, L.; Kalita, M.; Plewa-
        Marczewska, A.; Bitner, A.; Wieczorek, P.; Trzeciak, T.; *et al.* Electrolytes for Li-Ion
        Transport – Review. *Solid State Ionics* **2015**, *276*, 107–126.

(149)   Verma, P.; Maire, P.; Novák, P. A Review of the Features and Analyses of the Solid
        Electrolyte Interphase in Li-Ion Batteries. *Electrochim. Acta* **2010**, *55*, 6332–6341.

(150)   Peled, E. Advanced Model for Solid Electrolyte Interphase Electrodes in Liquid and

Polymer Electrolytes. *J. Electrochem. Soc.* **1997**, *144*, L208.

(151)   Aurbach, D. The Surface Chemistry of Lithium Electrodes in Alkyl Carbonate Solutions.
        J. Electrochem. Soc. **1994**, *141*, L1.

(152)   Zhang, S. S. A Review on Electrolyte Additives for Lithium-Ion Batteries. *J. Power
        Sources* **2006**, *162*, 1379–1394.

(153)   Aurbach, D.; Gamolsky, K.; Markovsky, B.; Gofer, Y.; Schmidt, M.; Heider, U. On the
        Use of Vinylene Carbonate (VC) as an Additive to Electrolyte Solutions for Li-Ion
        Batteries. *Electrochim. Acta* **2002**, *47*, 1423–1439.

(154)   Chen, L.; Wang, K.; Xie, X.; Xie, J. Effect of Vinylene Carbonate (VC) as Electrolyte
        Additive on Electrochemical Performance of Si Film Anode for Lithium Ion Batteries. *J.
        Power Sources* **2007**, *174*, 538–543.

(155)   Bouchet, R.; Maria, S.; Meziane, R.; Aboulaich, A.; Lienafa, L.; Bonnet, J.-P.; Phan, T.
        N. T.; Bertin, D.; Gigmes, D.; Devaux, D.; *et al.* Single-Ion BAB Triblock Copolymers
        as Highly Efficient Electrolytes for Lithium-Metal Batteries. *Nat. Mater.* **2013**, *12*, 452–
        457.

(156)   Zhao, J.; Wang, L.; He, X.; Wan, C.; Jiang, C. Determination of Lithium-Ion
        Transference Numbers in LiPF[Sub 6]–PC Solutions Based on Electrochemical
        Polarization and NMR Measurements. *J. Electrochem. Soc.* **2008**, *155*, A292.

(157)   Zugmann, S.; Fleischmann, M.; Amereller, M.; Gschwind, R. M.; Wiemhöfer, H. D.;
        Gores, H. J. Measurement of Transference Numbers for Lithium Ion Electrolytes via
        Four Different Methods, a Comparative Study. *Electrochim. Acta* **2011**, *56*, 3926–3933.

(158)   Valøen, L. O.; Reimers, J. N. Transport Properties of LiPF[Sub 6]-Based Li-Ion Battery Electrolytes. *J. Electrochem. Soc.* **2005**, *152*, A882.

(159)   Diederichsen, K. M.; McShane, E. J.; McCloskey, B. D. Promising Routes to a High Li$^+$ Transference Number Electrolyte for Lithium Ion Batteries. *ACS Energy Lett.* **2017**, *2*, 2563–2575.

(160)   Suo, L.; Hu, Y.-S.; Li, H.; Armand, M.; Chen, L. A New Class of Solvent-in-Salt Electrolyte for High-Energy Rechargeable Metallic Lithium Batteries. *Nat. Commun.* **2013**, *4*, 1481.

(161)   Suo, L.; Borodin, O.; Gao, T.; Olguin, M.; Ho, J.; Fan, X.; Luo, C.; Wang, C.; Xu, K. "Water-in-Salt" Electrolyte Enables High-Voltage Aqueous Lithium-Ion Chemistries. *Science* **2015**, *350*, 938–943.

(162)   Lu, Y.; Das, S. K.; Moganty, S. S.; Archer, L. A. Ionic Liquid-Nanoparticle Hybrid Electrolytes and Their Application in Secondary Lithium-Metal Batteries. *Adv. Mater. Weinheim* **2012**, *24*, 4430–4435.

(163)   Schaefer, J. L.; Yanga, D. A.; Archer, L. A. High Lithium Transference Number Electrolytes via Creation of 3-Dimensional, Charged, Nanoporous Networks from Dense Functionalized Nanoparticle Composites. *Chem. Mater.* **2013**, *25*, 834–839.

(164)   Tominaga, Y.; Yamazaki, K. Fast Li-Ion Conduction in Poly(Ethylene Carbonate)-Based Electrolytes and Composites Filled with TiO2 Nanoparticles. *Chem. Commun.* **2014**, *50*, 4448–4450.

(165)   Safa, M.; Chamaani, A.; Chawla, N.; El-Zahab, B. Polymeric Ionic Liquid Gel

Electrolyte for Room Temperature Lithium Battery Applications. *Electrochim. Acta* **2016**, *213*, 587–593.

(166)   Li, W.; Pang, Y.; Liu, J.; Liu, G.; Wang, Y.; Xia, Y. A PEO-Based Gel Polymer Electrolyte for Lithium Ion Batteries. *RSC Adv.* **2017**, *7*, 23494–23501.

(167)   Manthiram, A.; Yu, X.; Wang, S. Lithium Battery Chemistries Enabled by Solid-State Electrolytes. *Nat. Rev. Mater.* **2017**, *2*, 16103.

(168)   Dudney, N. Sputtering of Lithium Compounds for Preparation of Electrolyte Thin Films. *Solid State Ionics* **1992**, *53–56*, 655–661.

(169)   Hong, H. Y. P. Crystal Structure and Ionic Conductivity of Li14Zn(GeO4)4 and Other New Li+ Superionic Conductors. *Mater Res Bull* **1978**, *13*, 117–124.

(170)   Kanno, R.; Murayama, M. Lithium Ionic Conductor Thio-LISICON: The Li[Sub 2]S-GeS[Sub 2]-P[Sub 2]S[Sub 5] System. *J. Electrochem. Soc.* **2001**, *148*, A742.

(171)   Murugan, R.; Thangadurai, V.; Weppner, W. Fast Lithium Ion Conduction in Garnet-Type Li(7)La(3)Zr(2)O(12). *Angew. Chem. Int. Ed. Engl.* **2007**, *46*, 7778–7781.

(172)   Fu, K. K.; Gong, Y.; Dai, J.; Gong, A.; Han, X.; Yao, Y.; Wang, C.; Wang, Y.; Chen, Y.; Yan, C.; *et al.* Flexible, Solid-State, Ion-Conducting Membrane with 3D Garnet Nanofiber Networks for Lithium Batteries. *Proc. Natl. Acad. Sci. USA* **2016**, *113*, 7094–7099.

(173)   Han, X.; Gong, Y.; Fu, K. K.; He, X.; Hitz, G. T.; Dai, J.; Pearse, A.; Liu, B.; Wang, H.; Rubloff, G.; *et al.* Negating Interfacial Impedance in Garnet-Based Solid-State Li Metal Batteries. *Nat. Mater.* **2017**, *16*, 572–579.

(174)   Michael, M. S.; Jacob, M. M. E.; Prabaharan, S. R. S.; Radhakrishna, S. Enhanced

Lithium Ion Transport in PEO-Based Solid Polymer Electrolytes Employing a Novel

Class of Plasticizers. *Solid State Ionics* **1997**, *98*, 167–174.

(175)   Quartarone, E. PEO-Based Composite Polymer Electrolytes. *Solid State Ionics* **1998**,

110, 1–14.

(176)   Gorecki, W.; Andreani, R.; Berthier, C.; Armand, M.; Mali, M.; Roos, J.; Brinkmann, D.

NMR, DSC, and Conductivity Study of a Poly(Ethylene Oxide) Complex Electrolyte :

PEO(LiClO4)X. *Solid State Ionics* **1986**, *18–19*, 295–299.

(177)   Mukanova, A.; Jetybayeva, A.; Myung, S.-T.; Kim, S.-S.; Bakenov, Z. A Mini-Review

on the Development of Si-Based Thin Film Anodes for Li-Ion Batteries. *Materials

Today Energy* **2018**, *9*, 49–66.

(178)   Jin, Y.; Zhu, B.; Lu, Z.; Liu, N.; Zhu, J. Challenges and Recent Progress in the

Development of Si Anodes for Lithium-Ion Battery. *Adv. Energy Mater.* **2017**, 1700715.

(179)   Choi, M.; Kim, J.-C.; Kim, D.-W. Waste Windshield-Derived Silicon/Carbon

Nanocomposites as High-Performance Lithium-Ion Battery Anodes. *Sci. Rep.* **2018**, *8*,

960.

(180)   Choi, S.; Kwon, T.-W.; Coskun, A.; Choi, J. W. Highly Elastic Binders Integrating

Polyrotaxanes for Silicon Microparticle Anodes in Lithium Ion Batteries. *Science* **2017**,

357, 279–283.

(181)   Yoo, J.-K.; Kim, J.; Jung, Y. S.; Kang, K. Scalable Fabrication of Silicon Nanotubes and

Their Application to Energy Storage. *Adv. Mater. Weinheim* **2012**, *24*, 5452–5456.

(182)   Chen, H.; Hou, X.; Chen, F.; Wang, S.; Wu, B.; Ru, Q.; Qin, H.; Xia, Y. Milled Flake
         Graphite/Plasma Nano-Silicon@carbon Composite with Void Sandwich Structure for
         High Performance as Lithium Ion Battery Anode at High Temperature. *Carbon N. Y.*
         2018, *130*, 433–440.

(183)   Yoon, T.; Bok, T.; Kim, C.; Na, Y.; Park, S.; Kim, K. S. Mesoporous Silicon Hollow
         Nanocubes Derived from Metal-Organic Framework Template for Advanced Lithium-
         Ion Battery Anode. *ACS Nano* **2017**, *11*, 4808–4815.

(184)   Zhang, L.; Wang, C.; Dou, Y.; Cheng, N.; Cui, D.; Du, Y.; Liu, P.; Al-Mamun, M.;
         Zhang, S.; Zhao, H. A Yolk-Shell Structured Silicon Anode with Superior Conductivity
         and High Tap Density for Full Lithium-Ion Batteries. *Angew. Chem. Int. Ed. Engl.* **2019**,
         58, 8824–8828.

(185)   Li, P.; Chen, G.; Lin, Y.; Chen, F.; Chen, L.; Zhang, N.; Cao, Y.; Ma, R.; Liu, X. 3D
         Network Binder via In Situ Cross-Linking on Silicon Anodes with Improved Stability
         for Lithium-Ion Batteries. *Macromol. Chem. Phys.* **2020**, *221*, 1900414.

(186)   Yao, Y.; McDowell, M. T.; Ryu, I.; Wu, H.; Liu, N.; Hu, L.; Nix, W. D.; Cui, Y.
         Interconnected Silicon Hollow Nanospheres for Lithium-Ion Battery Anodes with Long
         Cycle Life. *Nano Lett.* **2011**, *11*, 2949–2954.

(187)   Fu, K.; Xue, L.; Yildiz, O.; Li, S.; Lee, H.; Li, Y.; Xu, G.; Zhou, L.; Bradford, P. D.;
         Zhang, X. Effect of CVD Carbon Coatings on Si@CNF Composite as Anode for
         Lithium-Ion Batteries. *Nano Energy* **2013**, *2*, 976–986.

(188)   Wu, H.; Chan, G.; Choi, J. W.; Ryu, I.; Yao, Y.; McDowell, M. T.; Lee, S. W.; Jackson,
         A.; Yang, Y.; Hu, L.; *et al.* Stable Cycling of Double-Walled Silicon Nanotube Battery

Anodes through Solid-Electrolyte Interphase Control. *Nat. Nanotechnol.* **2012**, *7*, 310–315.

(189)   Liu, J.; Kopold, P.; van Aken, P. A.; Maier, J.; Yu, Y. Energy Storage Materials from Nature through Nanotechnology: A Sustainable Route from Reed Plants to a Silicon Anode for Lithium-Ion Batteries. *Angew. Chem. Int. Ed. Engl.* **2015**, *54*, 9632–9636.

(190)   Wu, J.; Qin, X.; Miao, C.; He, Y.-B.; Liang, G.; Zhou, D.; Liu, M.; Han, C.; Li, B.; Kang, F. A Honeycomb-Cobweb Inspired Hierarchical Core–shell Structure Design for Electrospun Silicon/Carbon Fibers as Lithium-Ion Battery Anodes. *Carbon N. Y.* **2016**, *98*, 582–591.

(191)   Xin, X.; Zhou, X.; Wang, F.; Yao, X.; Xu, X.; Zhu, Y.; Liu, Z. A 3D Porous Architecture of Si/Graphene Nanocomposite as High-Performance Anode Materials for Li-Ion Batteries. *J. Mater. Chem.* **2012**, *22*, 7724.

(192)   Chae, C.; Noh, H.-J.; Lee, J. K.; Scrosati, B.; Sun, Y.-K. A High-Energy Li-Ion Battery Using a Silicon-Based Anode and a Nano-Structured Layered Composite Cathode. *Adv. Funct. Mater.* **2014**, *24*, 3036–3042.

(193)   He, Y.; Yu, X.; Wang, Y.; Li, H.; Huang, X. Alumina-Coated Patterned Amorphous Silicon as the Anode for a Lithium-Ion Battery with High Coulombic Efficiency. *Adv. Mater. Weinheim* **2011**, *23*, 4938–4941.

(194)   Lee, J.-I.; Ko, Y.; Shin, M.; Song, H.-K.; Choi, N.-S.; Kim, M. G.; Park, S. High-Performance Silicon-Based Multicomponent Battery Anodes Produced via Synergistic Coupling of Multifunctional Coating Layers. *Energy Environ. Sci.* **2015**, *8*, 2075–2084.

(195)   Gauthier, M.; Mazouzi, D.; Reyter, D.; Lestriez, B.; Moreau, P.; Guyomard, D.; Roué,

L. A Low-Cost and High Performance Ball-Milled Si-Based Negative Electrode for

High-Energy Li-Ion Batteries. *Energy Environ. Sci.* **2013**, *6*, 2145.

(196)   Yuan, W.; Friscić, T.; Apperley, D.; James, S. L. High Reactivity of Metal-Organic

Frameworks under Grinding Conditions: Parallels with Organic Molecular Materials.

Angew. Chem. Int. Ed. Engl. **2010**, *49*, 3916–3919.

(197)   Bennett, T. D.; Saines, P. J.; Keen, D. A.; Tan, J.-C.; Cheetham, A. K. Ball-Milling-

Induced Amorphization of Zeolitic Imidazolate Frameworks (ZIFs) for the Irreversible

Trapping of Iodine. *Chem. Eur. J* **2013**, *19*, 7049–7055.

(198)   Sohn, M.; Park, H.-I.; Kim, H. Foamed Silicon Particles as a High Capacity Anode

Material for Lithium-Ion Batteries. *Chem. Commun.* **2017**, *53*, 11897–11900.

(199)   Nzabahimana, J.; Chang, P.; Hu, X. Porous Carbon-Coated Ball-Milled Silicon as High-

Performance Anodes for Lithium-Ion Batteries. *J. Mater. Sci.* **2019**, *54*, 4798–4810.

(200)   Kasukabe, T.; Nishihara, H.; Iwamura, S.; Kyotani, T. Remarkable Performance

Improvement of Inexpensive Ball-Milled Si Nanoparticles by Carbon-Coating for Li-Ion

Batteries. *J. Power Sources* **2016**, *319*, 99–103.

(201)   Dean, J. A. Lange's Handbook of Chemistry. *Materials and Manufacturing Processes*

1990, *5*, 687–688.

(202)   Kim, K. H.; Lee, D. J.; Cho, K. M.; Kim, S. J.; Park, J.-K.; Jung, H.-T. Complete

Magnesiothermic Reduction Reaction of Vertically Aligned Mesoporous Silica Channels

to Form Pure Silicon Nanoparticles. *Sci. Rep.* **2015**, *5*, 9014.

(203)   Zhang, L.; Kuramoto, N.; Azuma, Y.; Kurokawa, A.; Fujii, K. Thickness Measurement of Oxide and Carbonaceous Layers on a[28] Si Sphere by XPS. *IEEE Trans Instrum Meas* **2017**, *66*, 1297–1303.

(204)   Sivaranjini, B.; Mangaiyarkarasi, R.; Ganesh, V.; Umadevi, S. Vertical Alignment of Liquid Crystals over a Functionalized Flexible Substrate. *Sci. Rep.* **2018**, *8*, 8891.

(205)   Khung, Y. L.; Ngalim, S. H.; Scaccabarozzi, A.; Narducci, D. Formation of Stable Si-O-C Submonolayers on Hydrogen-Terminated Silicon(111) under Low-Temperature Conditions. *Beilstein J Nanotechnol* **2015**, *6*, 19–26.

(206)   Michalak, D. J.; Amy, S. R.; Estève, A.; Chabal, Y. J. Investigation of the Chemical Purity of Silicon Surfaces Reacted with Liquid Methanol. *J. Phys. Chem. C* **2008**, *112*, 11907–11919.

(207)   Yohannes, Y. B.; Lin, S. D.; Wu, N.-L. In Situ DRIFTS Analysis of Solid Electrolyte Interphase of Si-Based Anode with and without Fluoroethylene Carbonate Additive. *J. Electrochem. Soc.* **2017**, *164*, A3641–A3648.

(208)   Zhang, H.; Qin, X.; Wu, J.; He, Y.-B.; Du, H.; Li, B.; Kang, F. Electrospun Core–shell Silicon/Carbon Fibers with an Internal Honeycomb-like Conductive Carbon Framework as an Anode for Lithium Ion Batteries. *J. Mater. Chem. A* **2015**, *3*, 7112–7120.

(209)   Park, T.-H.; Yeo, J.-S.; Seo, M.-H.; Miyawaki, J.; Mochida, I.; Yoon, S.-H. Enhancing the Rate Performance of Graphite Anodes through Addition of Natural Graphite/Carbon Nanofibers in Lithium-Ion Batteries. *Electrochim. Acta* **2013**, *93*, 236–240.

(210)   Sivakkumar, S. R.; Nerkar, J. Y.; Pandolfo, A. G. Rate Capability of Graphite Materials

as Negative Electrodes in Lithium-Ion Capacitors. *Electrochim. Acta* **2010**, *55*, 3330–3335.

(211)   Choi, J. W.; Aurbach, D. Promise and Reality of Post-Lithium-Ion Batteries with High Energy Densities. *Nat. Rev. Mater.* **2016**, *1*, 16013.

(212)   Zhang, H.; Li, C.; Piszcz, M.; Coya, E.; Rojo, T.; Rodriguez-Martinez, L. M.; Armand, M.; Zhou, Z. Single Lithium-Ion Conducting Solid Polymer Electrolytes: Advances and Perspectives. *Chem. Soc. Rev.* **2017**, *46*, 797–815.

(213)   Kalhoff, J.; Eshetu, G. G.; Bresser, D.; Passerini, S. Safer Electrolytes for Lithium-Ion Batteries: State of the Art and Perspectives. *ChemSusChem* **2015**, *8*, 2154–2175.

(214)   Ueno, K.; Murai, J.; Ikeda, K.; Tsuzuki, S.; Tsuchiya, M.; Tatara, R.; Mandai, T.; Umebayashi, Y.; Dokko, K.; Watanabe, M. Li$^+$ Solvation and Ionic Transport in Lithium Solvate Ionic Liquids Diluted by Molecular Solvents. *J. Phys. Chem. C* **2016**, *120*, 15792–15802.

(215)   Shi, F.; Pei, A.; Vailionis, A.; Xie, J.; Liu, B.; Zhao, J.; Gong, Y.; Cui, Y. Strong Texturing of Lithium Metal in Batteries. *Proc. Natl. Acad. Sci. USA* **2017**, *114*, 12138–12143.

(216)   Brissot, C.; Rosso, M.; Chazalviel, J. N.; Lascaud, S. Dendritic Growth Mechanisms in Lithium/Polymer Cells. *J. Power Sources* **1999**, *81–82*, 925–929.

(217)   Chazalviel, J. Electrochemical Aspects of the Generation of Ramified Metallic Electrodeposits. *Phys Rev, A* **1990**, *42*, 7355–7367.

(218)   Tu, Z.; Choudhury, S.; Zachman, M. J.; Wei, S.; Zhang, K.; Kourkoutis, L. F.; Archer,

L. A. Designing Artificial Solid-Electrolyte Interphases for Single-Ion and High-Efficiency Transport in Batteries. *Joule* **2017**, *1*, 394–406.

(219)   Song, J.; Lee, H.; Choo, M.-J.; Park, J.-K.; Kim, H.-T. Ionomer-Liquid Electrolyte Hybrid Ionic Conductor for High Cycling Stability of Lithium Metal Electrodes. *Sci. Rep.* **2015**, *5*, 14458.

(220)   Moganty, S. S.; Jayaprakash, N.; Nugent, J. L.; Shen, J.; Archer, L. A. Ionic-Liquid-Tethered Nanoparticles: Hybrid Electrolytes. *Angew. Chem. Int. Ed. Engl.* **2010**, *49*, 9158–9161.

(221)   Lu, Y.; Moganty, S. S.; Schaefer, J. L.; Archer, L. A. Ionic Liquid-Nanoparticle Hybrid Electrolytes. *J. Mater. Chem.* **2012**, *22*, 4066.

(222)   Wang, M.; Zhao, F.; Dong, S. A Single Ionic Conductor Based on Nafion and Its Electrochemical Properties Used As Lithium Polymer Electrolyte. *J. Phys. Chem. B* **2004**, *108*, 1365–1370.

(223)   Aqvist, J.; Luzhkov, V. Ion Permeation Mechanism of the Potassium Channel. *Nature* **2000**, *404*, 881–884.

(224)   Lemoine, D.; Jiang, R.; Taly, A.; Chataigneau, T.; Specht, A.; Grutter, T. Ligand-Gated Ion Channels: New Insights into Neurological Disorders and Ligand Recognition. *Chem. Rev.* **2012**, *112*, 6285–6318.

(225)   Dawson, R. J. P.; Benz, J.; Stohler, P.; Tetaz, T.; Joseph, C.; Huber, S.; Schmid, G.; Hügin, D.; Pflimlin, P.; Trube, G.; *et al.* Structure of the Acid-Sensing Ion Channel 1 in Complex with the Gating Modifier Psalmotoxin 1. *Nat. Commun.* **2012**, *3*, 936.

(226)   Corma, A.; García, H.; Llabrés i Xamena, F. X. Engineering Metal Organic Frameworks for Heterogeneous Catalysis. *Chem. Rev.* **2010**, *110*, 4606–4655.

(227)   Chughtai, A. H.; Ahmad, N.; Younus, H. A.; Laypkov, A.; Verpoort, F. Metal-Organic Frameworks: Versatile Heterogeneous Catalysts for Efficient Catalytic Organic Transformations. *Chem. Soc. Rev.* **2015**, *44*, 6804–6849.

(228)   Garibay, S. J.; Cohen, S. M. Isoreticular Synthesis and Modification of Frameworks with the UiO-66 Topology. *Chem. Commun.* **2010**, *46*, 7700–7702.

(229)   Katz, M. J.; Brown, Z. J.; Colón, Y. J.; Siu, P. W.; Scheidt, K. A.; Snurr, R. Q.; Hupp, J. T.; Farha, O. K. A Facile Synthesis of UiO-66, UiO-67 and Their Derivatives. *Chem. Commun.* **2013**, *49*, 9449–9451.

(230)   Miao, Z.; Qi, C.; Wensley, A. M.; Luan, Y. Development of a Novel Brønsted Acid UiO-66 Metal–organic Framework Catalyst by Postsynthetic Modification and Its Application in Catalysis. *RSC Adv.* **2016**, *6*, 67226–67231.

(231)   Garibay, S. J.; Wang, Z.; Tanabe, K. K.; Cohen, S. M. Postsynthetic Modification: A Versatile Approach toward Multifunctional Metal-Organic Frameworks. *Inorg. Chem.* **2009**, *48*, 7341–7349.

(232)   Shen, L.; Wu, H. B.; Liu, F.; Brosmer, J. L.; Shen, G.; Wang, X.; Zink, J. I.; Xiao, Q.; Cai, M.; Wang, G.; *et al.* Creating Lithium-Ion Electrolytes with Biomimetic Ionic Channels in Metal-Organic Frameworks. *Adv. Mater. Weinheim* **2018**, *30*, e1707476.

(233)   Shen, L.; Wu, H. B.; Liu, F.; Zhang, C.; Ma, S.; Le, Z.; Lu, Y. Anchoring Anions by Metal-Organic Framework-Functionalized Separators for Advanced Lithium Batteries.

Nanoscale Horiz. **2019**.

(234) Zhang, C.; Shen, L.; Shen, J.; Liu, F.; Chen, G.; Tao, R.; Ma, S.; Peng, Y.; Lu, Y. Anion-Sorbent Composite Separators for High-Rate Lithium-Ion Batteries. *Adv. Mater. Weinheim* **2019**, *31*, e1808338.

(235) Jiang, J.; Yaghi, O. M. Brønsted Acidity in Metal-Organic Frameworks. *Chem. Rev.* **2015**, *115*, 6966–6997.

(236) Britt, D.; Tranchemontagne, D.; Yaghi, O. M. Metal-Organic Frameworks with High Capacity and Selectivity for Harmful Gases. *Proc. Natl. Acad. Sci. USA* **2008**, *105*, 11623–11627.

(237) Russel, W. B.; Saville, D. A.; Schowalter, W. R. *Colloidal Dispersions*; Cambridge University Press: Cambridge, 1989.

(238) Kohonen, M. M.; Karaman, M. E.; Pashley, R. M. Debye Length in Multivalent Electrolyte Solutions. *Langmuir* **2000**, *16*, 5749–5753.

(239) Wrodnigg, G. H.; Besenhard, J. O.; Winter, M. Cyclic and Acyclic Sulfites: New Solvents and Electrolyte Additives for Lithium Ion Batteries with Graphitic Anodes? *J. Power Sources* **2001**, *97–98*, 592–594.

(240) Jouyban, A.; Soltanpour, S.; Chan, H.-K. A Simple Relationship between Dielectric Constant of Mixed Solvents with Solvent Composition and Temperature. *Int. J. Pharm.* **2004**, *269*, 353–360.

(241) Britt, D.; Lee, C.; Uribe-Romo, F. J.; Furukawa, H.; Yaghi, O. M. Ring-Opening Reactions within Porous Metal-Organic Frameworks. *Inorg. Chem.* **2010**, *49*, 6387–

6389.

(242)   Peterson, G. W.; Moon, S.-Y.; Wagner, G. W.; Hall, M. G.; DeCoste, J. B.; Hupp, J. T.;

Farha, O. K. Tailoring the Pore Size and Functionality of UiO-Type Metal-Organic

Frameworks for Optimal Nerve Agent Destruction. *Inorg. Chem.* **2015**, *54*, 9684–9686.

(243)   Bristow, J. K.; Svane, K. L.; Tiana, D.; Skelton, J. M.; Gale, J. D.; Walsh, A. Free

Energy of Ligand Removal in the Metal-Organic Framework UiO-66. *J. Phys. Chem. C,*

Nanomater. Interfaces **2016**, *120*, 9276–9281.

(244)   Shearer, G. C.; Chavan, S.; Ethiraj, J.; Vitillo, J. G.; Svelle, S.; Olsbye, U.; Lamberti, C.;

Bordiga, S.; Lillerud, K. P. Tuned to Perfection: Ironing Out the Defects in Metal–

Organic Framework UiO-66. *Chem. Mater.* **2014**, *26*, 4068–4071.

(245)   Bondy, A. L.; Craig, R. L.; Zhang, Z.; Gold, A.; Surratt, J. D.; Ault, A. P. Isoprene-

Derived Organosulfates: Vibrational Mode Analysis by Raman Spectroscopy, Acidity-

Dependent Spectral Modes, and Observation in Individual Atmospheric Particles. *J.*

Phys. Chem. A **2018**, *122*, 303–315.

(246)   Otal, E. H.; Kim, M. L.; Calvo, M. E.; Karvonen, L.; Fabregas, I. O.; Sierra, C. A.;

Hinestroza, J. P. A Panchromatic Modification of the Light Absorption Spectra of

Metal-Organic Frameworks. *Chem. Commun.* **2016**, *52*, 6665–6668.

(247)   Ferreira, G. R.; Garcia, H. C.; Couri, M. R. C.; Dos Santos, H. F.; de Oliveira, L. F. C.

On the Azo/Hydrazo Equilibrium in Sudan I Azo Dye Derivatives. *J. Phys. Chem. A*

2013, *117*, 642–649.

(248)   Bruce, P. Conductivity and Transference Number Measurements on Polymer

Electrolytes. *Solid State Ionics* **1988**, *28–30*, 918–922.

(249)   Feng, G.; Qiao, R.; Huang, J.; Dai, S.; Sumpter, B. G.; Meunier, V. The Importance of
        Ion Size and Electrode Curvature on Electrical Double Layers in Ionic Liquids. *Phys.*
        Chem. Chem. Phys. **2011**, *13*, 1152–1161.

(250)   Shannon, R. D. Revised Effective Ionic Radii and Systematic Studies of Interatomic
        Distances in Halides and Chalcogenides. *Acta Cryst. A* **1976**, *32*, 751–767.

(251)   Tasaki, K.; Goldberg, A.; Lian, J.-J.; Walker, M.; Timmons, A.; Harris, S. J. Solubility
        of Lithium Salts Formed on the Lithium-Ion Battery Negative Electrode Surface in
        Organic Solvents. *J. Electrochem. Soc.* **2009**, *156*, A1019.

(252)   Schroder, K.; Alvarado, J.; Yersak, T. A.; Li, J.; Dudney, N.; Webb, L. J.; Meng, Y. S.;
        Stevenson, K. J. The Effect of Fluoroethylene Carbonate as an Additive on the Solid
        Electrolyte Interphase on Silicon Lithium-Ion Electrodes. *Chem. Mater.* **2015**, *27*, 5531–
        5542.

(253)   Luan, Y.; Qi, Y.; Gao, H.; Zheng, N.; Wang, G. Synthesis of an Amino-Functionalized
        Metal–organic Framework at a Nanoscale Level for Gold Nanoparticle Deposition and
        Catalysis. *J. Mater. Chem. A* **2014**, *2*, 20588–20596.

(254)   Torchio, M.; Magni, L.; Gopaluni, R. B.; Braatz, R. D.; Raimondo, D. M. LIONSIMBA:
        A Matlab Framework Based on a Finite Volume Model Suitable for Li-Ion Battery
        Design, Simulation, and Control. *J. Electrochem. Soc.* **2016**, *163*, A1192–A1205.

(255)   Mathematical Modeling of a Lithium Ion Battery
        https://www.comsol.com/paper/mathematical-modeling-of-a-lithium-ion-battery-6678

(accessed Jul 1, 2020).